Aeroradiometric Measurements in the Framework of the Swiss ARM24 and International AGC24 Exercises

Alberto Stabilini, David Breitenmoser, Federico Geser,
Benno Bucher, Ladislaus Rybach, Cristina Poretti,
Stéphane Maillard, Adrian Hess, Malgorzata Kasprzak,
Gerald Scharding, Sabine Mayer

PSI-Report No. 25-01
March 2025
ISSN 1019-0643

DOI: http://doi.org/10.55402/psi:68900

PSI

Aeroradiometric Measurements in the Framework of the Swiss ARM24 and International AGC24 Exercises

Alberto Stabilini[1], David Breitenmoser[1], Federico Geser[1], Benno Bucher[2], Ladislaus Rybach[3], Cristina Poretti[4], Stéphane Maillard[5], Adrian Hess[4], Malgorzata Kasprzak[1], Gerald Scharding[4], Sabine Mayer[1]

1 Department of Radiation Safety and Security, Paul Scherrer Institute (PSI), Forschungsstrasse 111, 5232 Villigen PSI, Switzerland
2 Swiss Federal Nuclear Safety Inspectorate (ENSI), Industriestrasse 19, 5201 Brugg, Switzerland
3 Institute of Geophysics, Swiss Federal Institute of Technology Zürich (ETHZ), 8092 Zürich, Switzerland
4 Swiss National Emergency Operations Center (NEOC), 3003 Bern, Switzerland
5 NBC-EOD Centre of Excellence (Nuclear Biological Chemical defense and Explosive Ordnance Disposal), 3700 Spiez, Switzerland

DOI: http://doi.org/10.55402/psi:68900

PSI-Report No. 25-01
March 2025
ISSN 1019-0643

PSI

Abstract

Measurements of the civil exercise (ARM24c) took place at the Bürgenstock on the 29th May and on the 29th and 31st May in the area of the Beznau and Leibstadt nuclear power plants, the Zwilag interim storage facility, and the research facilities of the Paul Scherrer Institute. Atmospheric and terrestrial short-lived anthropogenic radionuclides in the western area of the Paul Scherrer Institute were detected and quantified using a newly developed Monte Carlo based full-spectrum Bayesian inversion method. A modest contribution of ^{16}N was detected above the premises of the nuclear power plant of Leibstadt (KKL), which was resuming operations. These emissions are allowed and monitored by the competent authorities. No deviations from the natural background were detected in the vicinities of the nuclear installation of the nuclear power plant of Beznau (KKB) and the interim storage facility Zwilag. The military campaign (ARM24m) surveyed the areas of Fleurier, Sainte-Croix, Concise, Ecuvillens, Gibloux in the western part of Switzerland between September the 17th and September the 20th. Traces of the Chernobyl accident depositions were detected in the Jura heights. The international campaign (AGC24) organised by the Czech Republic was held in Přerov (CZ) from the 3rd to the the 7th of June. The exercise involved reference measurements in designated areas characterised with in-situ measurements, the search and identification of radioactive sources, the assessment of a radiologically significant region with uranium-rich soil and subsoil, and composite mapping. Such exercises provide valuable opportunities to compare and refine methodologies, practise measurements under unique conditions not present in the national territory but pertinent to emergency scenarios, and harmonise procedures and data formats. These efforts contribute to smoother and more efficient international support during radiological emergencies.

Contents

List of Figures

List of Tables

1 Introduction

Swiss airborne gamma-ray spectrometry measurements started in 1986. The methodology and software for calibration, data acquisition and mapping were developed at the Institute of Geophysics of the Swiss Federal Institute of Technology Zurich (ETHZ). Between 1989 and 1993 the environs of Swiss nuclear installations were measured annually on behalf of the Swiss Federal Nuclear Safety Inspectorate (ENSI) during exercises performed as system check and drill for the operators. This schedule was changed to biennial inspections in 1994, together with an organizational inclusion of the airborne gamma-spectrometric system (ARM) into the Emergency Organization Radioactivity (EOR) of the Federal Office for Civil Protection (FOCP). The deployment of the airborne gamma-spectrometric system is organised by the National Emergency Operations Centre (NEOC). NEOC is also responsible for the recruitment and instruction of the measurement team and for the operational readiness of the systems. Aerial operations are coordinated and performed by the Swiss Air Force with Super Puma helicopters.

In 2018, the ARM measuring system used by NEOC in past exercises was replaced with the RLL (Radiometrie Land-Luft) system owned by the Swiss armed forces. The maintenance of the RLL systems is performed by the manufacturer according to a service agreement with the Swiss Armed Forces. Four identical gamma-spectrometric pieces of equipment are stationed in pairs at the military airfields of Dübendorf and Payerne and can be fully operative and airborne within four hours. Of the four systems available, under normal circumstances two systems are operated by the staff of the NBC-EOD Centre of Excellence (Nuclear Biological Chemical defense and Explosive Ordnance Disposal), for measurement tasks with military character, and two systems are assigned to NEOC, for the deployment in case of civil emergencies with a radiological component. For this year exercises the systems RLL 001 and RLL 004 were used.

Responsibility for scientific support, development and maintenance of the aeroradiometric measurement equipment passed from the Institute of Geophysics of ETHZ to the Radiation Metrology Section of the Paul Scherrer Institute (PSI) in 2003, in cooperation with ENSI. General scientific coordination and planning of the annual measuring flights is provided by the Expert Group for Airborne Gamma Spectrometry (FAR), which consists of experts from all Swiss institutions concerned with aeroradiometry. FAR, formerly a working group of the Swiss Federal Commission for NBC protection (ComNBC), was re-organized as an expert group of NEOC in 2008. Additional information can be found at `https://far.ensi.ch/`.

Since 2018, the scientific report includes, in addition to the measuring flights of NEOC (ARM24c & AGC24), flights performed by the NBC-EOD Centre of Excellence (ARM24m). This report focuses on methodological aspects and thus complements the respective short reports available at `https://www.vtg.admin.ch/de/lvbgrabc` for ARM24m and `https: //www.naz.ch` for ARM24c and AGC24.

ARM24c This year the program of the civil measurement campaign on Swiss territory was reduced, in favour of the international campaign in the Czech Republic. Measurements took place at the Bürgenstock on the 29th May and on the 29th and 31st May in the area of the nuclear power plants of Beznau, Leibstadt, Zwilag and the Paul Scherrer Institute.

ARM24m The military campaign surveyed the areas of Fleurier, Sainte-Croix, Concise, Ecuvillens, Gibloux in the western part of Switzerland between September the 17th and September the 20th.

AGC24 The international campaign organised by the Czech Republic was held in Přerov (CZ) from the 3rd to the 7th of June (Figure 1). The exercise involved reference measurements in designated areas characterised with in-situ measurements, the search and identification of radioactive sources, the assessment of a radiologically significant region with uranium-rich soil and subsoil, and composite mapping.

Figure 1: Participants of the AGC24 International measurement campaign in the Czech Republic

2 Equipment and methodology

2.1 Measuring system RLL

The measuring system RLL (Radiometrie Land-Luft) used both for civil and military measurements consists of a radiation detector featuring four NaI(TI) scintillation crystals having a total volume of 16.8 litres with their associated photo-multipliers and multichannel analysers (MCA) for low level measurements, and one Geiger-Müller tube and associated electronics for high dose-rate measurements. The spectroscopic measuring chain provides a linear energy calibration of the MCA up to 3.072 MeV divided into 1024 channels. NaI detectors, Geiger-Müller tube and associated acquisition chain are installed in an aluminium case with thermal insulation foam. The detection container is mounted in the cargo bay below the centre of the helicopter. The RLL system registers position, air pressure, air temperature and radar altitude data provided by the helicopter via the internal ARINC bus. Figure 2 shows the complete system packaged for storage.

The equipment control, data acquisition and storage are performed with a rugged computer working as a data server. Two additional redundant rugged client computers are used as operator interface for real-time evaluation, data mapping and communication. All computers are installed in an equipment rack, including an additional battery as power supply backup. Both operators can manage the system with their associated client computer, display, keyboard and trackball. The additional third central display on the operators' console is mirrored on a screen in the cockpit, located between the pilots, and is used for information exchange with the pilots and general radiological situation awareness (Figure 4).

The measuring system RLL is mounted in an Aerospatiale AS 332 Super Puma helicopter (TH 06) of the Swiss Air Forces (Figure 3). This helicopter has excellent navigation properties and allows emergency operations during bad weather conditions and night time.

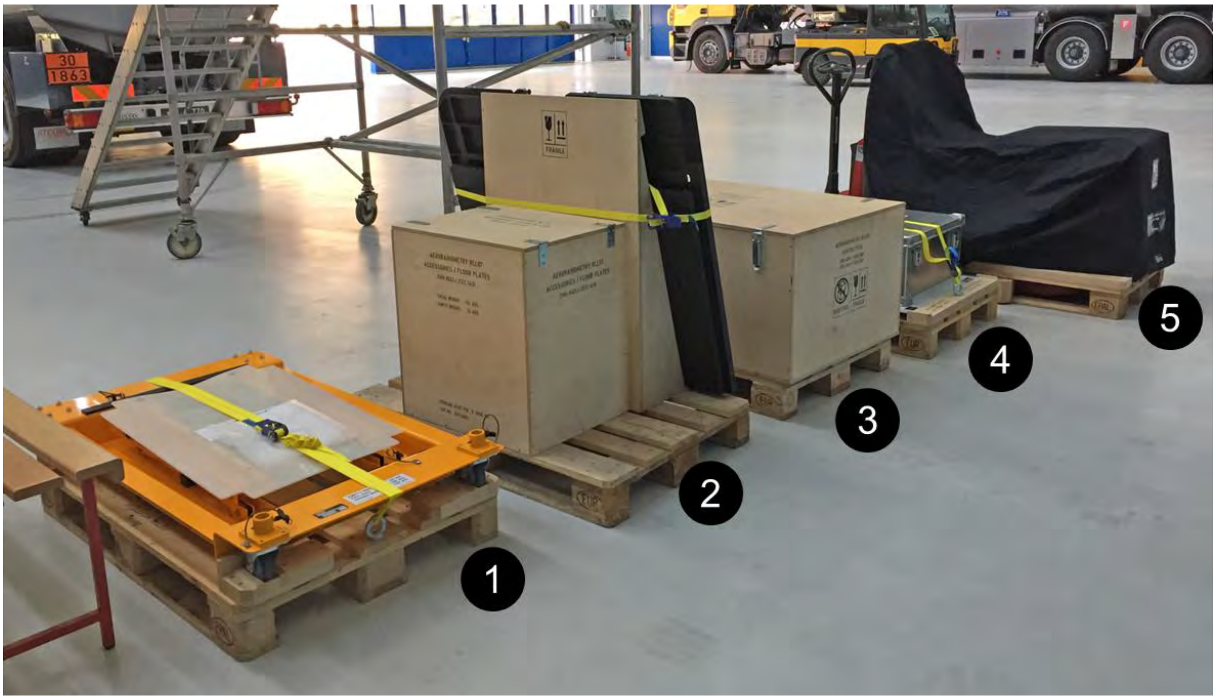

Figure 2: Components of the RLL system. 1. Lifting platform for the installation of the detection container. 2. Floor plates and accessories case. 3. Monitors and operator console. 4. Detection container. 5. Operator seats and equipment rack.

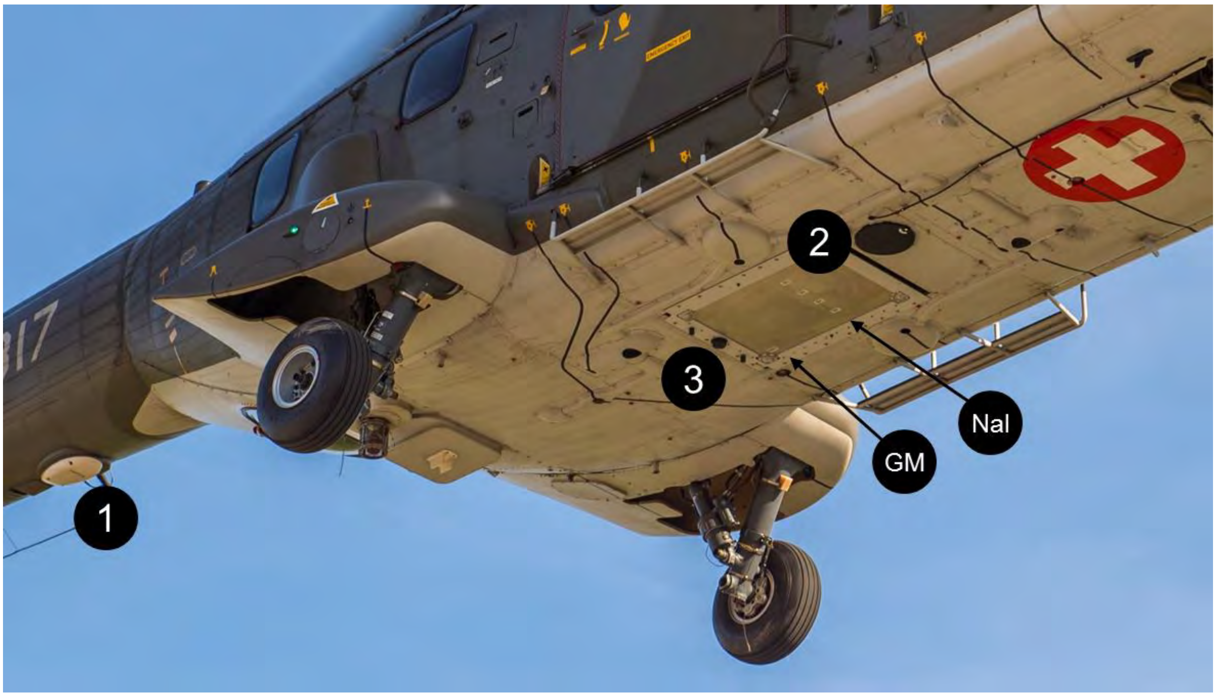

Figure 3: RLL detector mounted in the cargo bay of a Super Puma helicopter. 1. Radar altimeter. 2. Detection container marked with detector reference points. 3. UMTS antenna for data upload. GM. Geiger-Müller detector. NaI: Inorganic scintillation detector

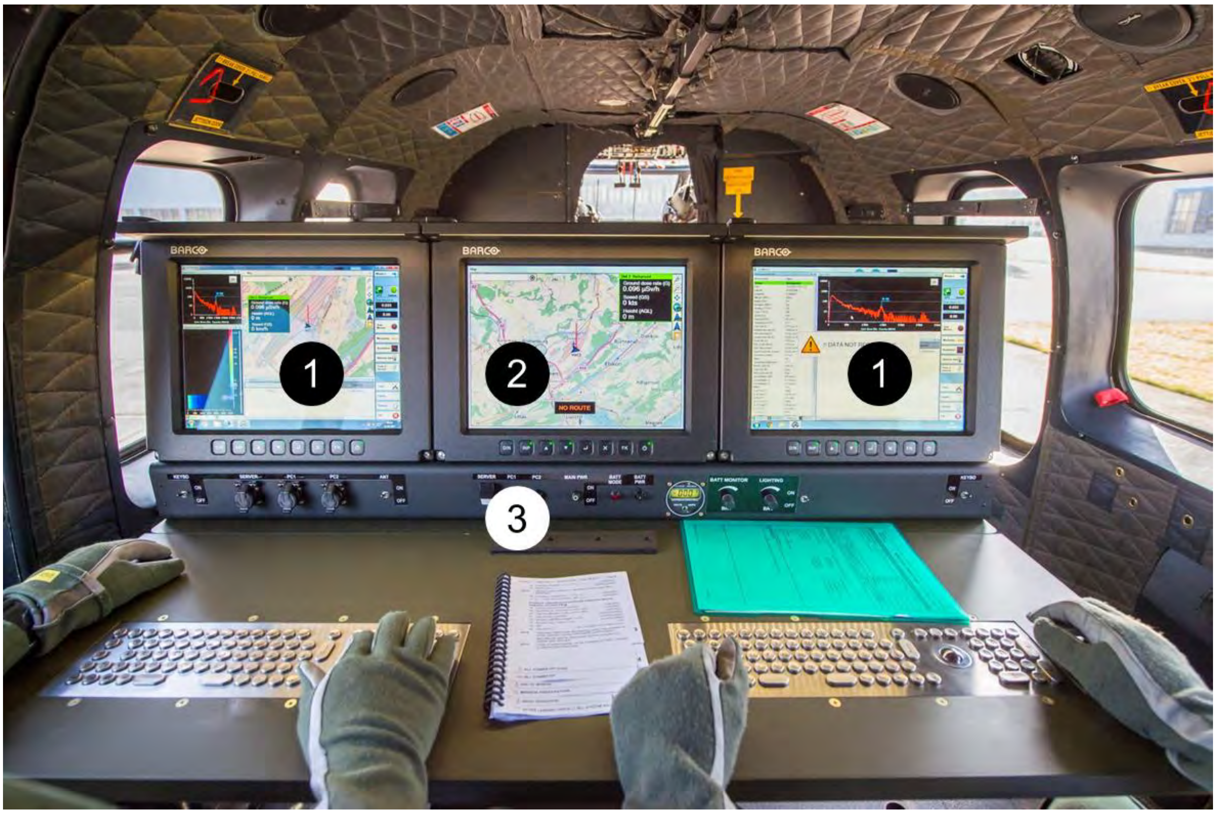

Figure 4: Operator console of the RLL system. 1. Displays of the client computers. 2. Common display (mirrored in the cockpit). 3. Control panel with switches for power, lighting and communication and USB ports for file exchange.

2.1.1 Characterisation of spectral cross-talk of RLL 002

Photons emitted from the soil are scattered due to Compton and Rayleigh effects in the soil itself, in buildings, in vegetation, in the air between surface and helicopter, in the helicopter and in the detector. The associated energy loss may lead to a registration of the photon in a lower photon energy window. Further contributions to cross-talk effects come from the limited energy resolution of a NaI(Tl)-detector compared to modern solid-state detectors, causing photons with energies near the boundaries of an energy window to be registered in the adjacent energy window. Additionally, as natural uranium and thorium are the entry point of a complete decay series, multiple photons are emitted throughout the whole energy spectrum. The spectral counts in the various energy windows associated with these photon emissions have to be corrected. The correction is implemented by applying stripping factors, which can be determined with measurements of radioactive point sources near the detector (Schwarz et al., 1997).

Although not used during this year's exercises, a characterisation of the detector RLL 002 was newly performed at the calibration laboratory of PSI in July 2024, since one of its crystals has been object of repair (Figure 5). During the characterisation, a deviation in the energy calibration of crystal four was noticed in comparison to the other three crystals, resulting in a distortion of the acquired spectrum. As can be appreciated in Figure 6, low energy peaks recorded by crystal four are shifted to lower energies in comparison to the other crystals, while high energy peaks are shifted towards even higher energies. Since the spectrum used for the evaluation of data is the sum of the signal generated by the four crystals, if not recognised, this effect would induce a broadening of the peaks of the sum spectrum, ultimately worsening the system resolution. The reason causing a distortion in the energy calibration of crystal four has been discussed with the manufacturer and was identified in an erroneous setting of the energy calibration parameters accounting for non-linearities. Once adjusted, before proceeding with the characterisation of the spectral cross-talk, the spectra of each crystal were assessed again, as reported in Figure 7, where all crystals show comparable energy calibrations. Since the energy calibration of each crystal can be easily checked and compared, a dedicated measurement before the beginning of an exercise could be adopted in the QA protocol during the system set-up. This would help recognising energy calibration issues that, if present, would worsen the quality of the results obtained during measurements.

As detectors RLL 001, RLL 003 and RLL 004 were not modified since the last characterisation, the stripping factors determined in previous characterisations are still valid. Table 1 gives an overview on the current stripping factors of the four Swiss systems, with the values of detector RLL 004 determined for three of the four NaI crystals, due to quality issues. The results indicate that the individual stripping factors determined for each detector may be replaced with a generic set of factors, under the condition that all four systems perform inside their specifications. The stripping factors are stored under the ISWS identifier in the header of the ERS 2.0 data files (Section 7).

Figure 5: Detector RLL 002 mounted in the laboratory for the determination of stripping factors.

Detector		RLL 001	RLL 002	RLL 003	RLL 004
Year		2020	2024	2022	2021
"‘from"’-window	"‘to"’-window	Stripping factor			
Uranium	Potassium	0.93	0.95	0.98	0.92
Thorium	Potassium	0.48	0.46	0.50	0.47
Cobalt	Potassium	0.07	0.06	0.05	0.04
Thorium	Uranium	0.36	0.33	0.34	0.34
Uranium	Thorium	0.05	0.06	0.06	0.05
Potassium	Caesium	0.45	0.44	0.48	0.37
Uranium	Caesium	3.16	3.21	3.18	2.78
Thorium	Caesium	1.65	1.59	1.64	1.44
Cobalt	Caesium	0.15	0.13	0.13	0.12
Potassium	Cobalt	0.76	0.75	0.79	0.66
Uranium	Cobalt	2.37	2.35	2.32	2.26
Thorium	Cobalt	0.68	0.66	0.63	0.65

Table 1: Stripping factors for relevant energy windows of the RLL detectors.

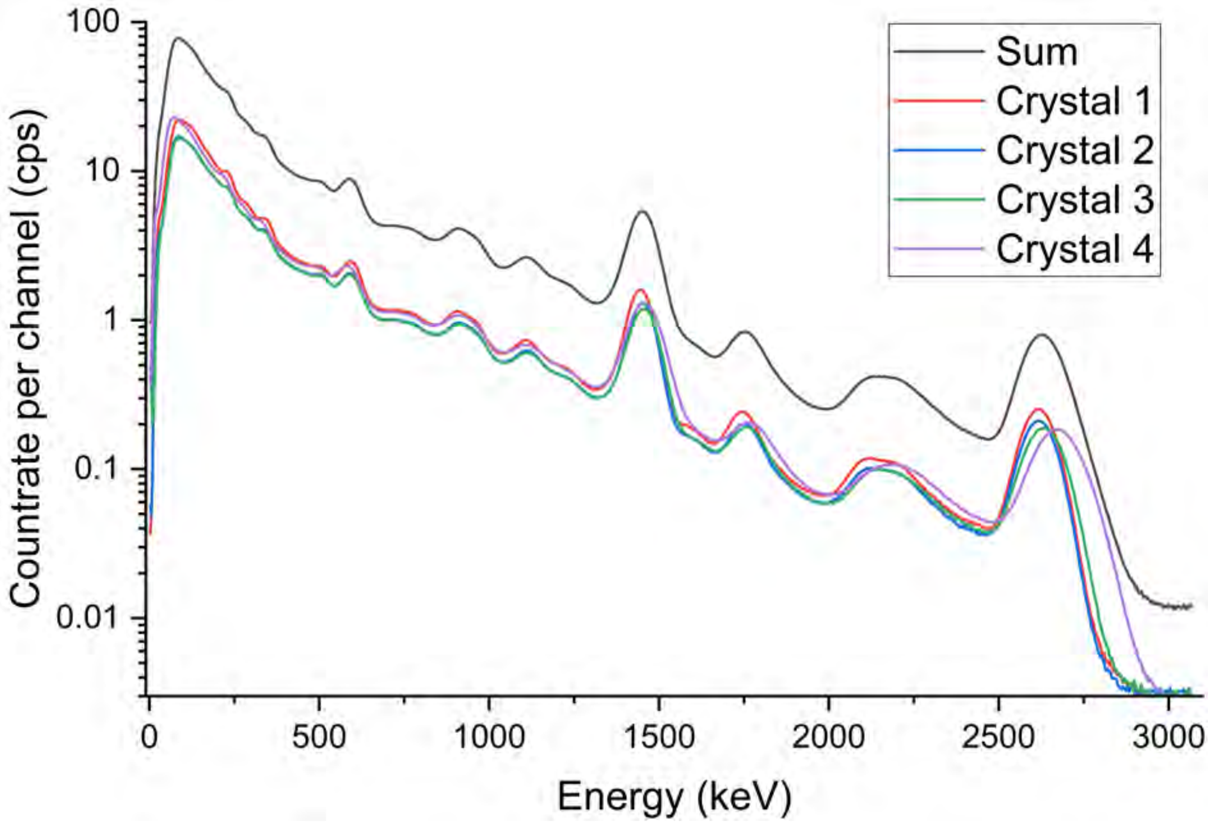

Figure 6: Energy calibration of single crystals of detector RLL 002 before parameter adjustment.

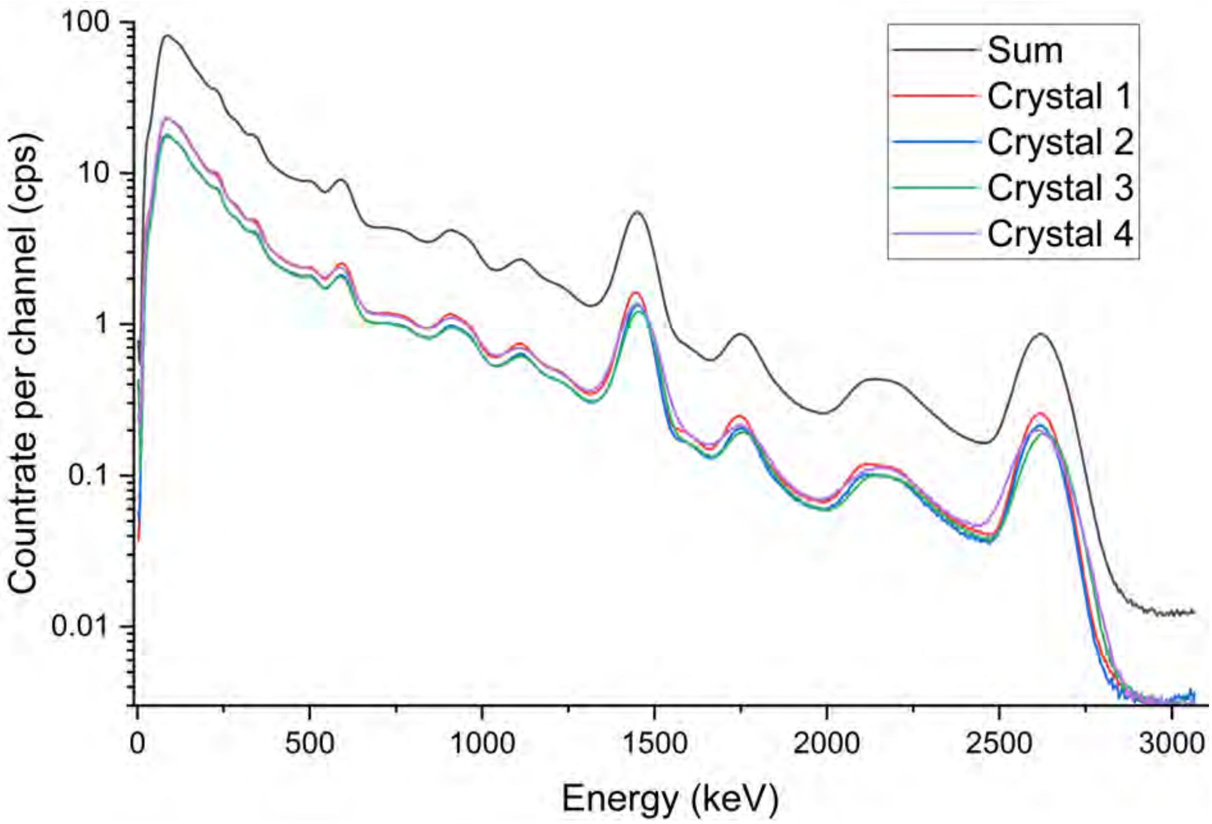

Figure 7: Energy calibration of single crystals of detector RLL 002 after parameter adjustment.

2.2 Measuring flights

The advantage of aeroradiometry lies in the high velocity of measurements in a large area, even over rough terrain. Uniform radiological information of an area is obtained from a regular grid of measuring points. This grid is composed from parallel flight lines, 250 m apart in the standard case. The flight altitude above ground is aspired to be constant during the measuring flight, with typical values lying between 50 m and 150 m above ground. Line spacing and altitude can be adjusted depending on the scope of the measurements: larger line spacing and higher altitude can be adopted for wider area screenings (though increasing the detection limits), whereas a narrower line spacing pattern at reduced altitudes is adopted for confirmation flights or to increase the location accuracy of confined sources of radiation. The spectra are recorded in regular time intervals of typically one second, yielding an integration over 28 m of the flight line considering a speed of 100 km/h.

2.2.1 Flights in Switzerland

The flights of the civil (ARM24c) and military (ARM24m) parts of the exercise were performed between May 29th and 31st and between September 17th and September 20th, respectively.

Flight velocity of the Super Puma helicopters of the Swiss Air Force was around 30 m/s with a target ground clearance of 90 m for all measuring flights. The sampling interval of the spectra was one second. The detection system RLL 001 was used for the civil part, whereas system RLL 004 was used for the military part of the exercise. The evaluation parameters used for these systems are listed in Section 7.

Personnel of the military units Stab BR NAZ and NBC-EOD Centre of Excellence performed the measurements supported by experts from ENSI, PSI, ETHZ, NBC-EOD Centre of Excellence and NEOC.

In the civil part (ARM24c), according to the biennial schedule, measurements were performed over the area of the nuclear installations of PSI, Zwilag, Kernkraftwerk Beznau (KKB) and Kernkraftwerk Leibstradt (KKL). Additionally, the area of the Bürgenstock mountain, on the southern shore of Lake Lucerne, was surveyed ahead of the event to obtain reference values for the venue hosting the High-Level Conference on Peace in Ukraine (HLCPU).

The military exercise (ARM24m) focused on expanding the measured area of the western part of Switzerland. To this aim, regions of Fleurier and Sainte-Croix at the border with France were screened, as well as the region of Concise on lake Neuchâtel and the regions of Ecuvillens and Gibloux in the canton of Fribourg. Due to adverse weather conditions, the regions of Concise and Sainte-Croix could not be entirely surveyed. These will be completed in future measurement campaigns.

2.2.2 Issues experienced with system RLL 004

The RLL 004 system, employed during the military campaign, encountered issues that affected the quality of the raw data collected during flights. These issues were only identified later, during the detailed data analysis conducted for this scientific report. Specifically, three distinct problems were identified, each affecting a different crystal within the RLL 004 system. Nonetheless, these problems did not prevent the evaluation of the measurements.

Energy calibration of crystal 2

During the ARM24m exercise, crystal 2 of system RLL 004 exhibited a different energy calibration compared to the other three crystals. This issue closely resembles the one observed with system RLL 002 during its characterisation, as described in Section 2.1.1. The shift in the spectrum acquired by crystal 2, resulting from the differing energy calibration, affects the combined signal of the sum of all four crystals, ultimately degrading the energy resolution. Figure 8 illustrates an example of the raw spectra acquired by each crystal of system RLL 004 during one of the flights in the ARM24m, where the shift in the spectrum of crystal 2 is evident in comparison to the others.

As mentioned, the issue with the energy calibration of crystal 2 was detected only at the time of the detailed data analysis conducted for this report, where individual crystal spectra were analysed separately using the AGS_CH software. The AGS_CH software also provides functionality for rebinning spectra acquired by a specific crystal (i.e. set anew the relationship between the acquisition channels of the multichannel analyser and the photon energy), based on the positions of full-energy peaks in the spectrum produced by naturally occurring radionuclides: ^{40}K, ^{232}Th, and ^{238}U. Figure 9 presents the spectra originally shown in Figure 8, after the rebinning of the spectrum of crystal 2 and the subsequent reconstructed sum spectrum considering the adjustment. As can be inferred from the figure, this a posteriori rebinning procedure compensates to a large extent for a spectral distortions arising from differing energy calibration. However, it remains preferable to conduct data acquisitions with correct energy calibration for all crystals. As suggested in Section 2.1.1 for system RLL 002, this can be ensured by performing a dedicated measurement prior to an exercise during the system set-up. Before analysis, all data acquired during the ARM24m exercise were processed to adjust the energy calibration of crystal 2.

Identical spectra acquired by crystal 1

Crystal 1 was also affected by an issue during the flights over the Gibloux, Fleurier and Sainte-Croix regions. A detailed data analysis conducted for this report revealed that the raw data acquired with crystal 1 were repeated, resulting in a constant spectrum throughout the entire flight, as shown in the waterfall representation of the spectrum in Figure 10. The cause of this issue could not be determined. For the evaluation of the data from the aforementioned regions, it was decided to exclude the spectra of crystal 1.

Gaps in the spectra acquisition of crystal 3

The detailed data analysis conducted for this report also revealed issues with crystal 3 during the measurements over the areas of Gibloux, Fleurier, and Sainte-Croix. The problem encountered involved gaps in the acquisition of the spectra, resulting in the absence of spectra from crystal 3 in the raw data for several points in the flown regions. This can be observed in the example shown in Figure 11, where the waterfall spectrum of crystal 3 is disrupted by white bands, indicating missing data. During the inspection of the RLL 004 system following the measurement campaign, a loose connector was detected in the acquisition chain of crystal 3, which could explain the data gaps experienced. For the evaluation of the data from the aforementioned regions, it was decided to exclude the spectra of crystal 3.

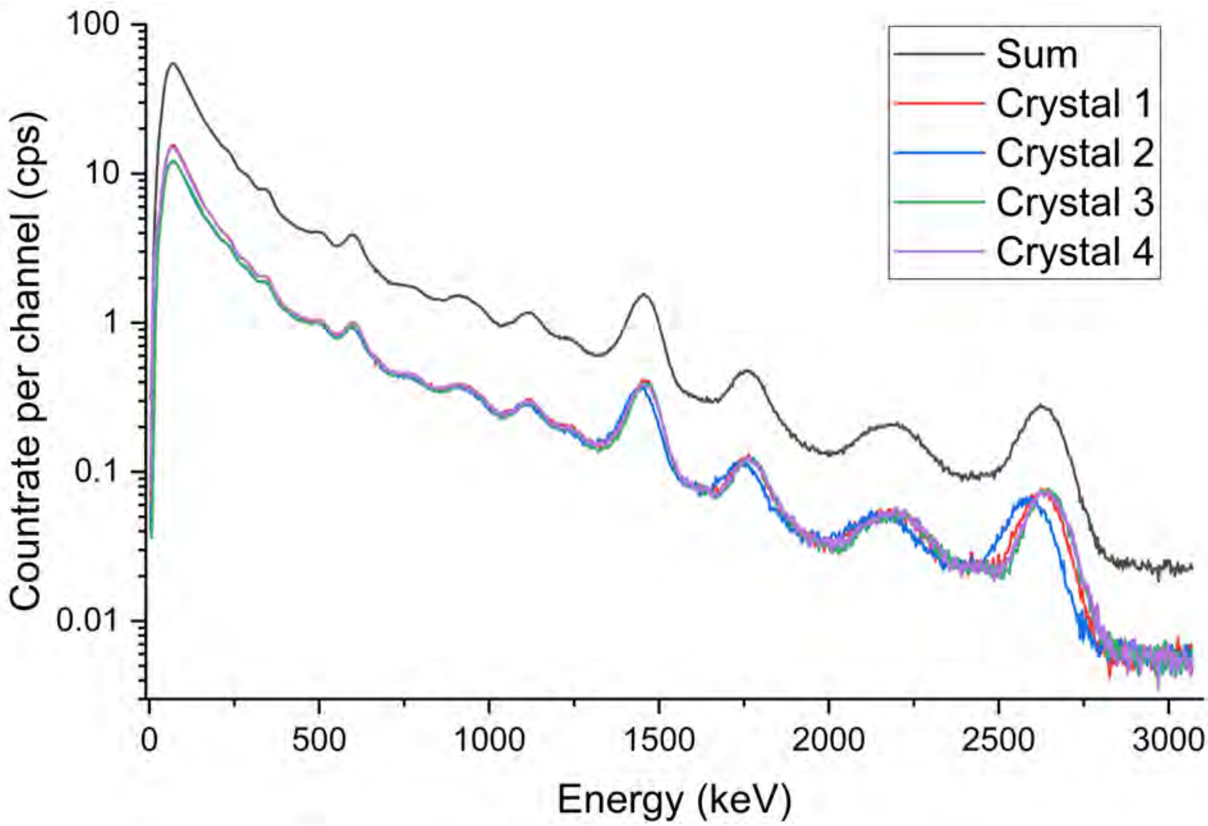

Figure 8: Energy calibration of single crystals and sum signal of detector RLL 004 before rebinning of crystal 2.

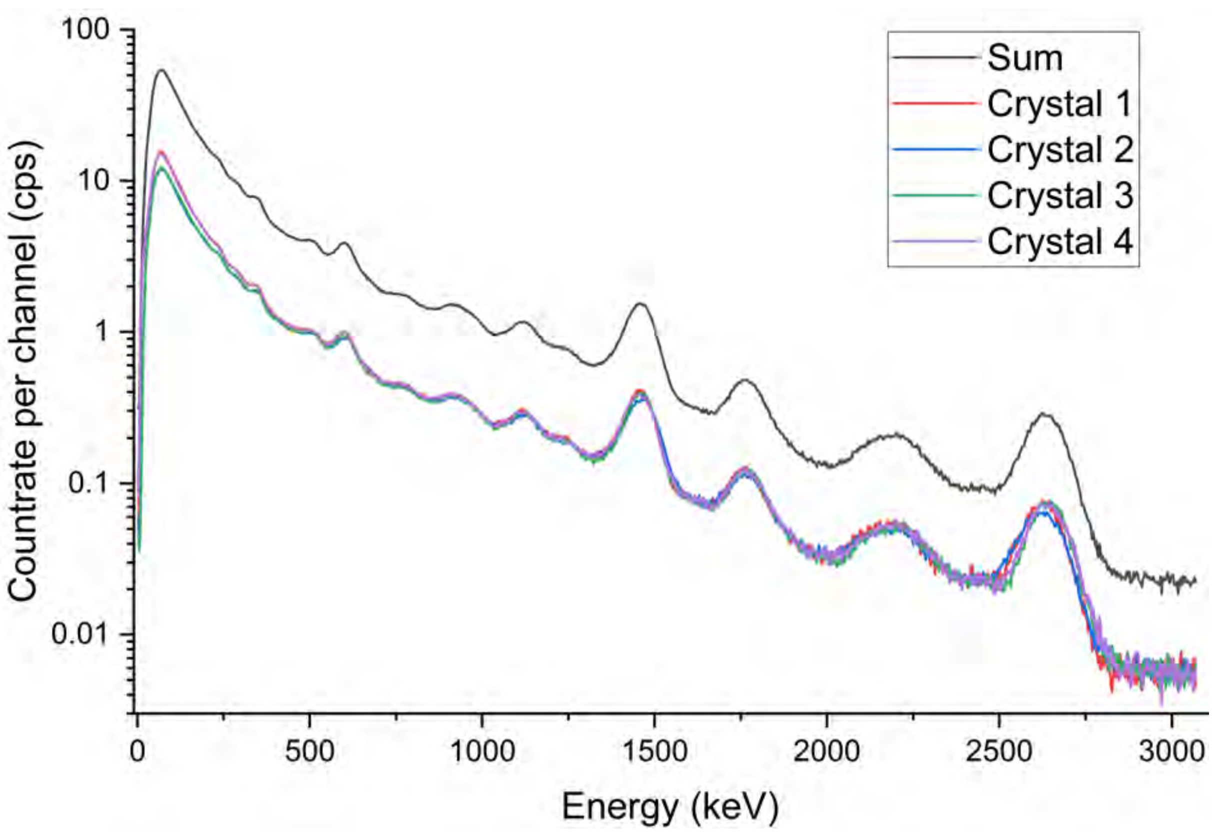

Figure 9: Energy calibration of single crystals and sum signal of detector RLL 004 after rebinning of crystal 2.

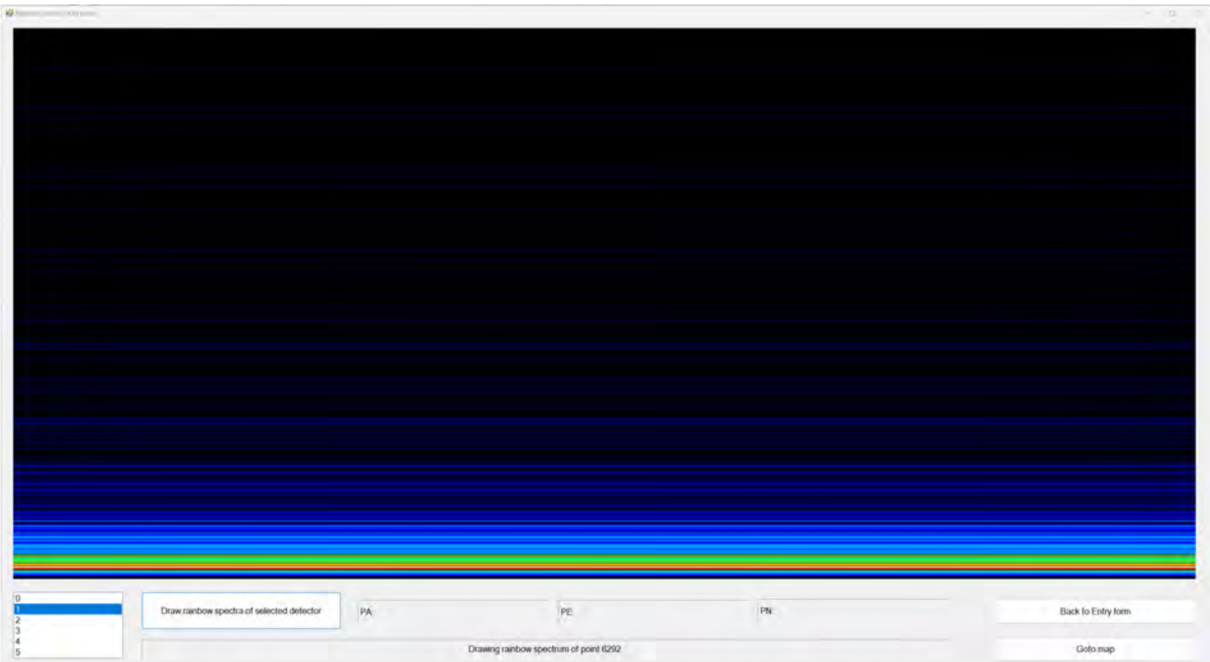

Figure 10: Issue affecting crystal 1 of system RLL 004, detected during the data analysis (identical spectra).

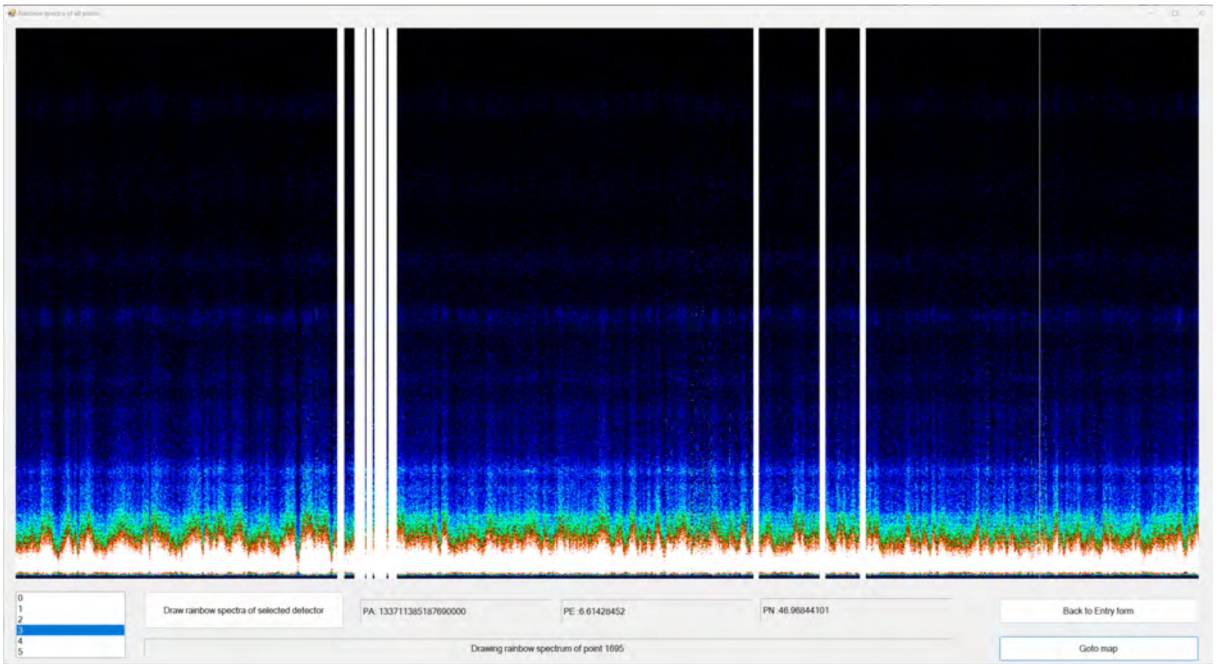

Figure 11: Issue affecting crystal 3 of system RLL 004, detected during the data analysis (gaps in acquisition).

2.2.3 AGC24

The international measurement campaign AGC24 took place in the Czech Republic from Monday, June 3rd to Friday, June 7th. The Swiss aeroradiometric team, alongside the local team of the Czech Institute of Radiation Protection (SÚRO) and the team from the French Institute for Radiation Protection and Nuclear Safety (IRSN) took part in the event. The Přerov airport (CZE) served both as base for flight operations as well as a station for the evaluation teams. The exercise involved reference measurements in designated areas characterised with in-situ measurements, the search and identification of radioactive sources, the assessment of a radiologically significant region with uranium-rich soil and subsoil, and composite mapping. The program included four missions, or "Tasks", that each team was required to complete. Preliminary results were shared on the final day of the measurement campaign as data files in the "‘ERS 2.0"’ format, described in the PSI-Report 18-04. The adoption of this format for sharing results among teams during an international exercise was introduced for the first time in this international campaign and proved to be very effective.

Task I - Vyskov (VYK): Reference area mapping

Task I (VSK) assigned the measurement of a reference area of approximatively 1 km^2 in the surroundings of the city of Vyskov. Within the allotted time of 60 minutes, the area had to be screened twice, with two different ground clearances: 70 m and 140 m respectively (Task I-A). Additionally, for each flight altitude, the centre of the area (49.340559N, 16.961147E) had to be hovered for 5 minutes (Task I-B). Further flight parameters were not specified, and left to be decided by each team. The objective was to provide, for each specific flying altitude and task, the total dose rate at 1m from the ground and the activity concentration of ^{40}K, ^{232}Th, ^{238}U and ^{137}Cs.

Task II - Vysocina (VYS): Bohemian - Moravian uplands

Task II (VYS) foresaw the measurement of a 23 km^2 area in the Bohemian - Moravian uplands near Vysocina, displayed in Figure 12. Within the perimeter of the defined area, to be screened at a flying speed of 100 km/h and a ground clearance of 100 m, the two regions identified in yellow in Figure 12 were given higher priority. Flight time allotted to accomplish the task was 90 minutes. The reported measurements were required to include the total dose rate at one metre above the ground, along with the activity concentrations of: ^{40}K, ^{232}Th, ^{238}U and ^{137}Cs, as well as any location exhibiting anomalies or unusual values.

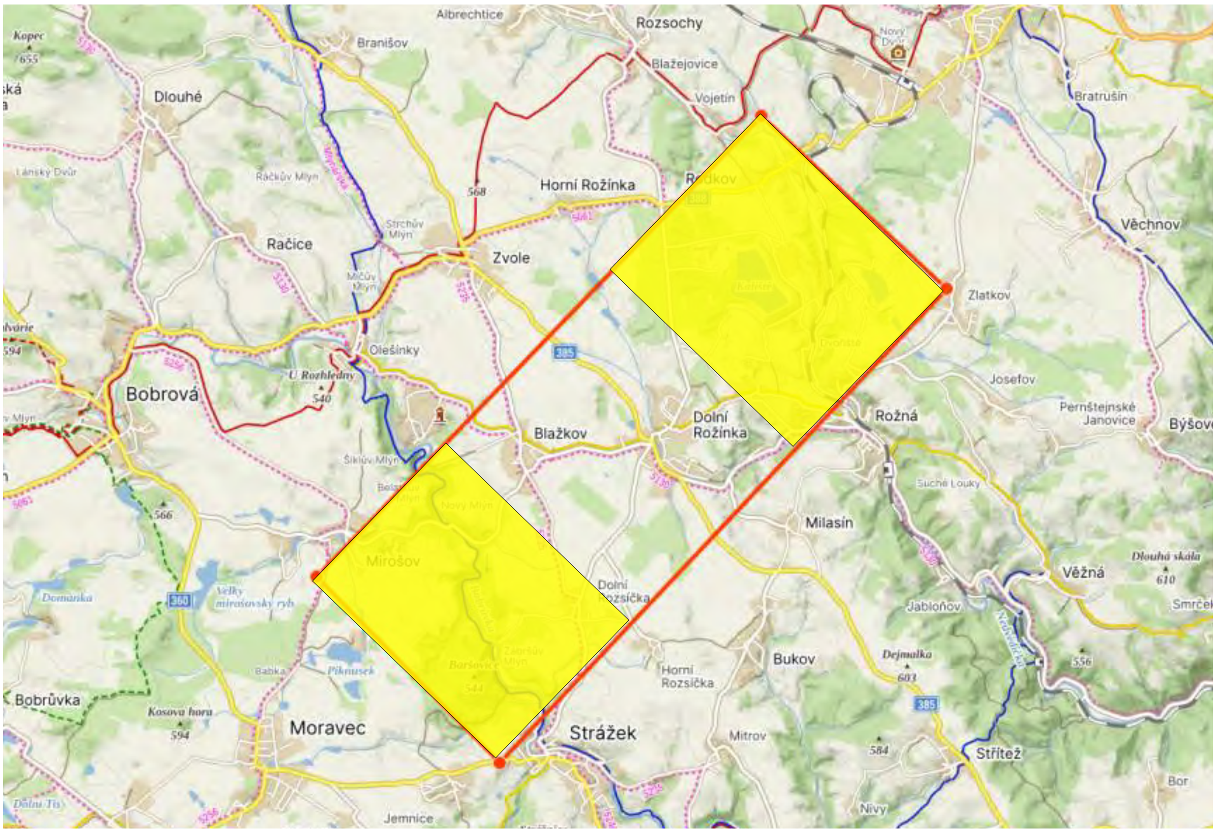

Figure 12: Map of Task II - Vysocina (VYS): Bohemian - Moravian uplands. Source: AGC24 Organisers.

Task III - Opavsko (OPA): Composite mapping

Task III (OPA) was devoted to composite mapping. A large area, laying in the south of the city Opava, had to be jointly screened by the participating teams. As part of the exercise, the teams had to agree on a screening strategy and subdivide the area to be screened by each team, according to each team measuring protocol and aircraft flight capabilities and range. Except a maximum flight altitude of 150 m, no flight parameter was constrained. At the end of the measurement, each team had to deliver a map of the total dose rate at 1 m from the ground and the activity concentration of: ^{40}K, ^{232}Th, ^{238}U and ^{137}Cs.

Task IV - Libava (LIB): Source search

Task IV (LIB) foresaw a source search within the specified perimeter reported in Figure 13, with the additional constraint that the eastern part of the polygon marked in blue could not be crossed by helicopters. The task had to be carried out within 90 minutes, with a flight clearance of 100 m and a speed of 100 km/h to 120 km/h. The goal was to locate, identify and estimate the activity of any radioactive source placed on the area.

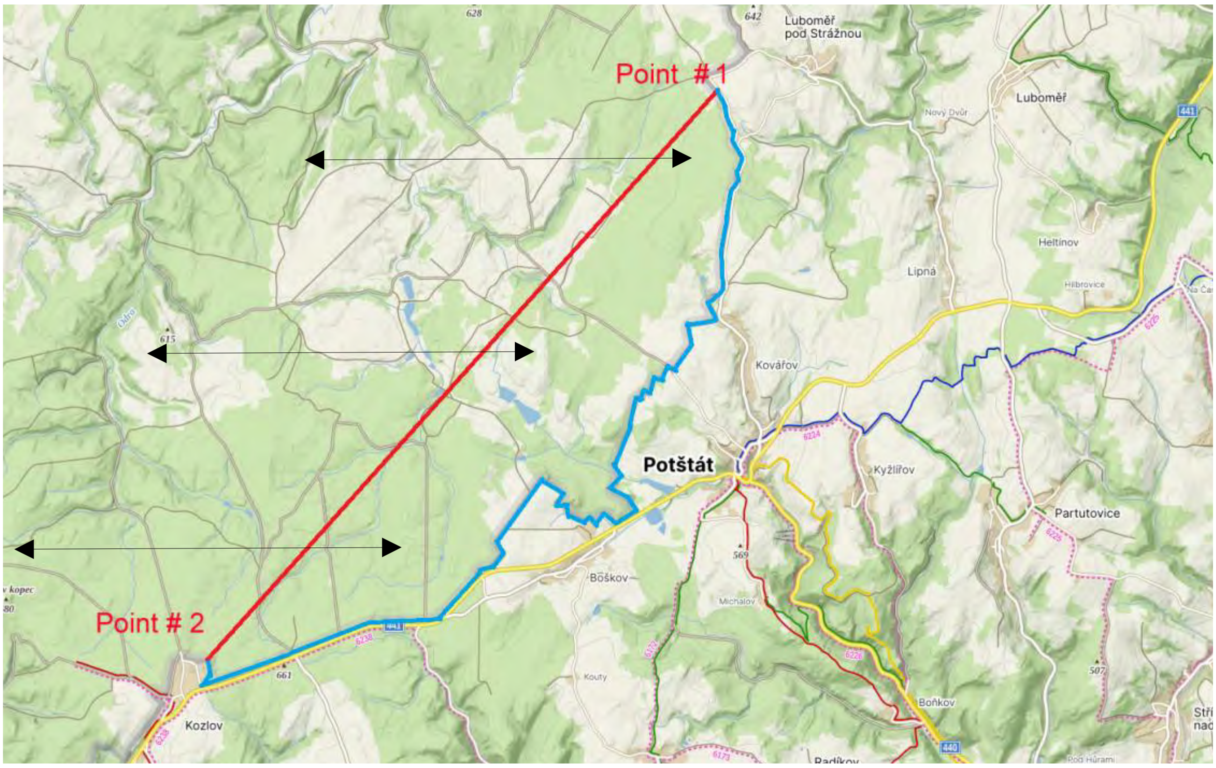

Figure 13: Map of Task IV - Libava (LIB): Source search. Source: AGC24 Organisers.

2.3 Data evaluation

The proprietary software for data acquisition and evaluation provided by the manufacturer of the RLL system was tested sufficient for supplying data to support decisions in radiological emergencies and was used to produce the short reports of NEOC (ARM24c & AGC24) and NBC-EOD Centre of Excellence (ARM24m). An outline of the algorithms used can be found in Butterweck et al. (2018).

2.3.1 AGS_CH

An additional independent off-line data evaluation software (named AGS_CH) following the methodology developed at ETHZ described in Schwarz (1991) and Bucher (2001) is used to produce the results presented throughout the PSI reports since 2020. The measured spectra are evaluated using energy windows for relevant radionuclides and the spectrum dose index (SDI) to determine dose rates.

Background and cosmic correction

The background and cosmic correction is based on a series of altitude profiles measurements acquired in the past years over Swiss lakes. Table 2 summarises the slopes of the Deming regression (Butterweck et al.,2021) obtained from these measurements and the average slope used as estimator for the cosmic correction. With the average slope, intercepts of the linear model for cosmic correction can be calculated, representing the constant background of the measuring system. Table 3 shows the backgrounds based on the average slopes listed in Table 2. Being the estimated cosmic background the result of a process including averaging procedures, negative values may occur, when values are particularly close to zero.
The background and slope used for the data evaluation of the current exercise are stored under identifiers ISWB_winname and ISWC_winname in the header section of all ERS 2.0 files (Section 7) generated for ARM24 data evaluation.

	Slope of cosmic correction [ ]						
Energy Window	Total	^{40}K	^{238}U	^{232}Th	^{137}Cs	^{60}Co	SDI
Lake Constance 2023c	4.11	0.23	0.13	0.30	0.17	0.36	3.15
Lake Geneva 2018c	5.20	0.28	0.21	0.29	0.45	0.60	3.96
Lake Neuchâtel 2019c	5.48	0.31	0.23	0.26	0.60	0.66	4.09
Lake Neuchâtel 2021c	5.68	0.33	0.23	0.29	0.57	0.72	4.28
Lake Neuchâtel 2021m	6.32	0.35	0.27	0.30	0.75	0.76	4.70
Lake Thun A 2022c	6.32	0.48	0.30	0.33	0.91	1.09	4.66
Lake Thun B 2022c	7.17	0.41	0.32	0.31	0.92	0.80	5.21
Lake Zug 2017c	5.96	0.31	0.25	0.29	0.69	0.70	4.51
Average	5.78	0.34	0.24	0.30	0.63	0.71	4.32
Standard deviation	0.91	0.08	0.06	0.02	0.25	0.21	0.62

Table 2: Determination of the average slope for cosmic correction from seven altitude profiles with sufficient altitude range.

Energy Window	Background count rate [cps] Total	^{40}K	^{238}U	^{232}Th	^{137}Cs	^{60}Co	SDI
Lake Constance 2023c	124	8	6	0.3	20	12	85
Lake Geneva 2018c	147	10	7	0.3	23	15	101
Lake Neuchâtel 2016c	129	7	6	1.2	21	10	88
Lake Neuchâtel 2019c	104	8	5	-1.0	16	10	70
Lake Neuchâtel 2021c	121	8	5	0.0	18	11	84
Lake Neuchâtel 2021m	145	9	7	0.4	23	14	98
Lake Neuchâtel 2022m	111	7	6	-0.8	19	10	74
North Sea 2018c	34	4	0	-0.1	5	1	22
Lake Thun A 2020c	73	6	3	-0.4	11	6	48
Lake Thun B 2020c	73	5	3	-0.4	11	6	48
Lake Thun A 2022c	134	9	6	-0.1	22	13	91
Lake Thun B 2022c	157	9	8	0.6	25	15	109
Lake Zug 2017c	56	5	2	-0.2	8	3	38

Table 3: Determination of the background count rate using the average slope of cosmic stripping from Table 2.

2.3.2 Monte Carlo based full-spectrum Bayesian inversion

While the AGS_CH data evaluation software has proven effective in quantifying natural terrestrial radionuclides, it faces significant limitations in quantifying anthropogenic gamma-ray sources due to its reliance on empirical calibration and simplified physics models (Breitenmoser, 2024). To address these limitations, a new Monte Carlo based Full-Spectrum Bayesian Inversion (FSBI) methodology was developed and rigorously validated through extensive laboratory and field radiation measurements as part of a PhD project co-financed by ENSI and PSI (grant no. CTR00836 & CTR00491). This methodology allows for the quantification of any gamma-ray source, whether terrestrial or atmospheric, with an unprecedented level of accuracy and sensitivity, successfully overcoming the limitations of the current approach.

In this report, we describe the first successful application of the newly developed FSBI methodology to analyse an anomaly detected during a routine exercise, which the current method could not resolve. The results of the FSBI analysis are detailed in Section 3.1.2. Below, we provide a brief, non-technical summary of the FSBI methodology. A detailed description of the newly developed FSBI methodology is available in Breitenmoser (2024).

One of the main differences between the current data analysis software and the new FSBI methodology is the transition from an empirical to a numerical calibration approach, leveraging high-fidelity Monte Carlo simulations with the `FLUKA` code (Ahdida et al., 2022). This numerical approach allows for the accurate simulation of the full-spectrum detector response to arbitrarily complex gamma-ray sources. To account for scintillation non-proportionality effects, the adopted scintillation physics models are calibrated using Compton edge probing (Breitenmoser et al., 2023).

Another key advancement of the FSBI methodology over the current data analysis software is the application of full-spectrum analysis (FSA) instead of the spectral window approach for inferring gamma-ray source strengths from measured pulse-height spectra. In contrast to the spectral window approach, which relies on a small subset of pulse-height channels, FSA evaluates the entire spectrum channel-by-channel. As a result, no information is lost during the analysis, resulting in a substantial increase in sensitivity and accuracy (Breitenmoser, 2024). The FSA approach is performed using Bayesian statistics, specifically Markov Chain Monte Carlo (MCMC) sampling (Goodman et al., 2010) implemented in the UQLab code (Marelli, 2014).

For the FSBI analysis in this report, we adopted a gamma-Poisson mixture likelihood function with noncommittal, statistically independent marginal priors for all model parameters, as suggested in the original work by Breitenmoser (2024). To enable Bayesian model comparison (Trotta, 2008), we extended the FSBI methodology from Breitenmoser (2024) by integrating a dedicated importance sampling algorithm, providing accurate estimates of marginal likelihoods and Bayes factors (Perrakis, 2014).

2.4 Data presentation

Brief reports of the measurement results are compiled by the respective measurement teams and published immediately after the end of the exercise on the homepage of NEOC and the homepage of NBC-EOD Centre of Excellence. These reports are also archived at `https://far.ensi.ch` under Publications as: Short Report - NEOC and Short Report NBC-KAMIR. A combined detailed analysis of both parts of the exercise is published in the form of a PSI-report within the responsibility of the FAR. These reports are archived at `https://far.ensi.ch` (as Scientific Reports) and at Paul Scherrer Institute Digital Object Repository (DORA PSI) `https://www.dora.lib4ri.ch/psi`.

Concerning the measurement in Switzerland, maps are given in EPSG:2056 - CH1903+ /LV95 coordinates. For all measuring areas, a map of the total dose rate (ambient dose equivalent rate dH*(10)/dt extrapolated to 1 m above ground) and the flight lines is presented together with a map of the Man-Made-Gross-Count (MMGC) ratio and the one of ^{232}Th activity concentration.

The MMGC-ratio is defined as the quotient between the count rate summed over the energy window (MMGC1), between 400 keV and 1400 keV, and the count rate summed over the energy window (MMGC2), between 1400 keV and 3000 keV. As most anthropogenic radionuclides emit photons below 1400 keV, the ratio will rise due to these additional photons, whereas natural radionuclides are registered in both energy windows, keeping the ratio relatively constant. Although the MMGC-ratio is undoubtedly a useful quantity, it is worth mentioning that it is prone to show artefacts when particularly low counts in the MMGC2 energy window occur due to limited counting statistics. As this can also lead to increased MMGC-ratios, a careful inspection of the MMGC2 counts is required for elevated values. If the dose rate or the MMGC-ratio indicate elevated values, maps of individual radionuclides (like e.g. ^{40}K or ^{137}Cs activity concentrations) are added based on the average photon spectrum over the affected area.

The map of the ^{232}Th activity concentration (activity per wet mass) provides information on the quality of the measurements for recurrent sites, as this quantity is expected to remain constant over time.

In the case of large changes of topography in the measured area, a map of the terrestrial dose rate, calculated from the total dose rate deducted by the altitude-dependent cosmic component, is included. In the case of measuring flights aiming at mapping natural radionuclide concentrations, a supplementary map of the ^{40}K activity concentration (activity per wet mass) may also be presented.

^{238}U activity concentration maps (activity per wet mass) are presented as needed. These maps are however affected, especially for low ^{238}U concentrations, by the variable concentration of radon and its progeny in the atmosphere at the time of measurement.

Concerning the international exercise AGC24, maps are given in EPSG:32633 - WGS84 UTM zone 33N coordinates. Results and maps are provided according to the request of the organiser. If needed, these are accompanied by additional ones to address specific aspects of the results. As an additional quality measure, an appendix with the basic parameters of the data evaluation is added to simplify a re-evaluation of the data in the future.

A discrete colour scale was defined by the Swiss Expert Group for Aeroradiometrics (FAR) in 2019. The colours and their representation as red, green and blue (RGB) values are listed in Table 4 together with the represented ranges of measured values. The unit of ambient dose-equivalent rates used in previous reports, $[\mathrm{nSv/h}]$, was changed with the new representation to $[\mu\mathrm{Sv/h}]$, the unit used to store ambient dose-equivalent rate values in the ERS 2.0 format (Butterweck et al. (2018)).

Colour	Red	Green	Blue	Dose rate [μSv/h]	MMGC-ratio [ ]	Activity per mass [Bq/kg] ^{40}K	^{238}U, ^{232}Th, ^{137}Cs	Activity per area [kBq/m^2] ^{137}Cs (β=9.5 g/cm^2)
	153	0	153	> 10	> 100	> 10000	> 5000	> 1000
	204	0	102	5 - 10	50 - 100	5000 - 10000	1000 - 5000	200 - 1000
	204	0	0	2 - 5	15 - 50	2000 - 5000	500 - 1000	100 - 200
	255	0	0	0.5 - 2	9 - 15	1500 - 2000	250 - 500	50 - 100
	255	176	51	0.3 - 0.5	8 - 9	1000 - 1500	200 - 250	40 - 50
	255	235	51	0.2 - 0.3	7 - 8	800 - 1000	150 - 200	30 - 40
	230	255	128	0.15 - 0.2	unused	600 - 800	100 - 150	20 - 30
	173	255	153	0.1 - 0.15	unused	400 - 600	75 - 100	15 - 20
	073	255	106	0.08 - 0.1	6 - 7	200 - 400	50 - 75	10 - 15
	102	255	255	0.06 - 0.08	5 - 6	100 - 200	25 - 50	5 - 10
	77	148	255	0.04 - 0.06	unused	50 - 100	12.5 - 25	2.5 - 5
	51	102	179	< 0.04	< 5	< 50	< 12.5	< 2.5

Table 4: Quantification of the colour scale.

3 Results

Parameters describing the measuring flights performed in 2024 are listed in Table 5 and an overview of the corresponding flight lines (in Switzerland) is shown in Figure 14.

Location	Flight identification	Measuring time [s]	Length of run [km]	Area [km^2]
	Recurrent measuring areas over nuclear installations			
Region PSI KKB KKL	Heli 1_20240529 1524 Heli 1_20240531 0845	11290	470.5	110.7
	AGC24 International campaign			
Vyskov	Heli 1_20240603 1155	1127	27.8	2.2
	Heli 1_20240603 1220	1233	31.8	2.6
Vysocina	Heli 1_20240604 1341 Heli 1_20240604 1417 Heli 1_20240604 1436 Heli 1_20240604 1505	5466	232.7	30.6
Opavsko	Heli 1_20240606 1026	6666	373.2	89.1
Libava	Heli 1_20240506 1310	2659	96.1	20.1
	Heli 1_20240506 1400	2396	96.5	18.9
	Background measurements over cities, towns and regions			
Bürgenstock	Heli 1_20240529 1044	1484	54.8	7.4
Concise	Heli 4_20240918 1005 Heli 4_20240920 0835 Heli 4_20240920 0845	9305	401.2	87.7
Ecuvillens	Heli 4_20240919 0845	3862	156	33.9
Fleurier	Heli 4_20240918 1440 Heli 4_20240919 1350	14659	681.2	159.9
Gibloux	Heli 4_20240917 1030 Heli 4_20240917 1410 Heli 4_20240919 1140	19887	858	202.2
Sainte-Croix	Heli 4_20240920 0945	5474	215.5	50.6

Table 5: Flight data of ARM24.

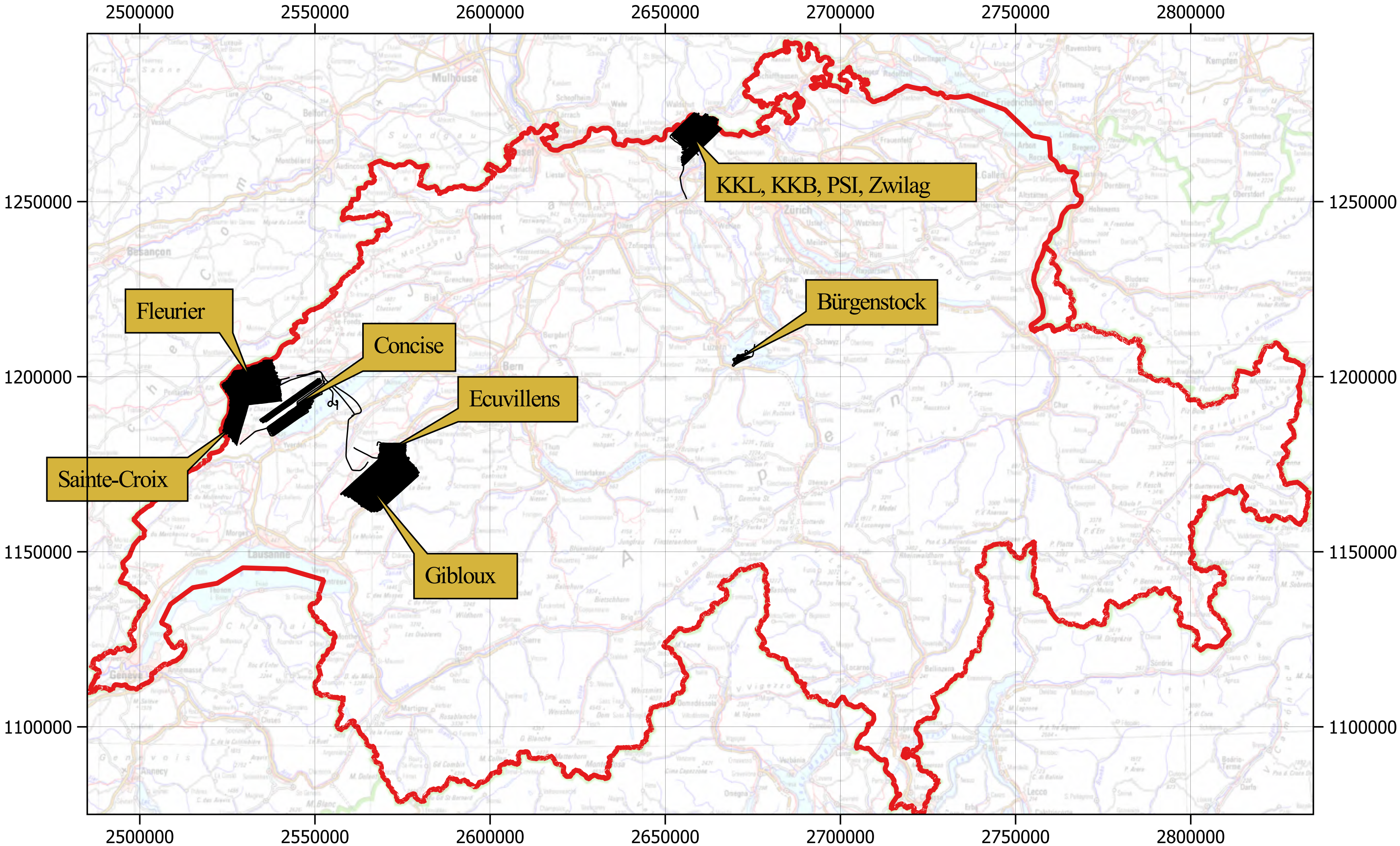

Figure 14: Overview of the measurement areas of ARM24 (Switzerland). Geodaten©swisstopo.

3.1 Measurements in Switzerland

3.1.1 Bürgenstock

The area of Bürgenstock mountain was added to the survey schedule to obtain, ahead of the event, reference values for the venue hosting the High Level Conference on Peace in Ukraine (HLCPU). The terrain in the area show peculiar alpine features, as the northern wall of the mountain, facing lake Lucern, present steep cliffs, which pose a further challenge in terms of flight navigation.

The map of the measured dose rate in Figure 15 shows typical values found in the alpine region, ranging from 0.04 μSv/h along the lake shore to 0.15 μSv/h on the mountain peaks. The area is characterised by low ^{232}Th concentration, mostly below 25 Bq kg^{-1}, as reported in Figure 16. The ^{40}K map (Figure 17) features a limited region, centred on the souther slope of the mountain, where slightly larger values (< 800 Bq kg^{-1}) have been detected.

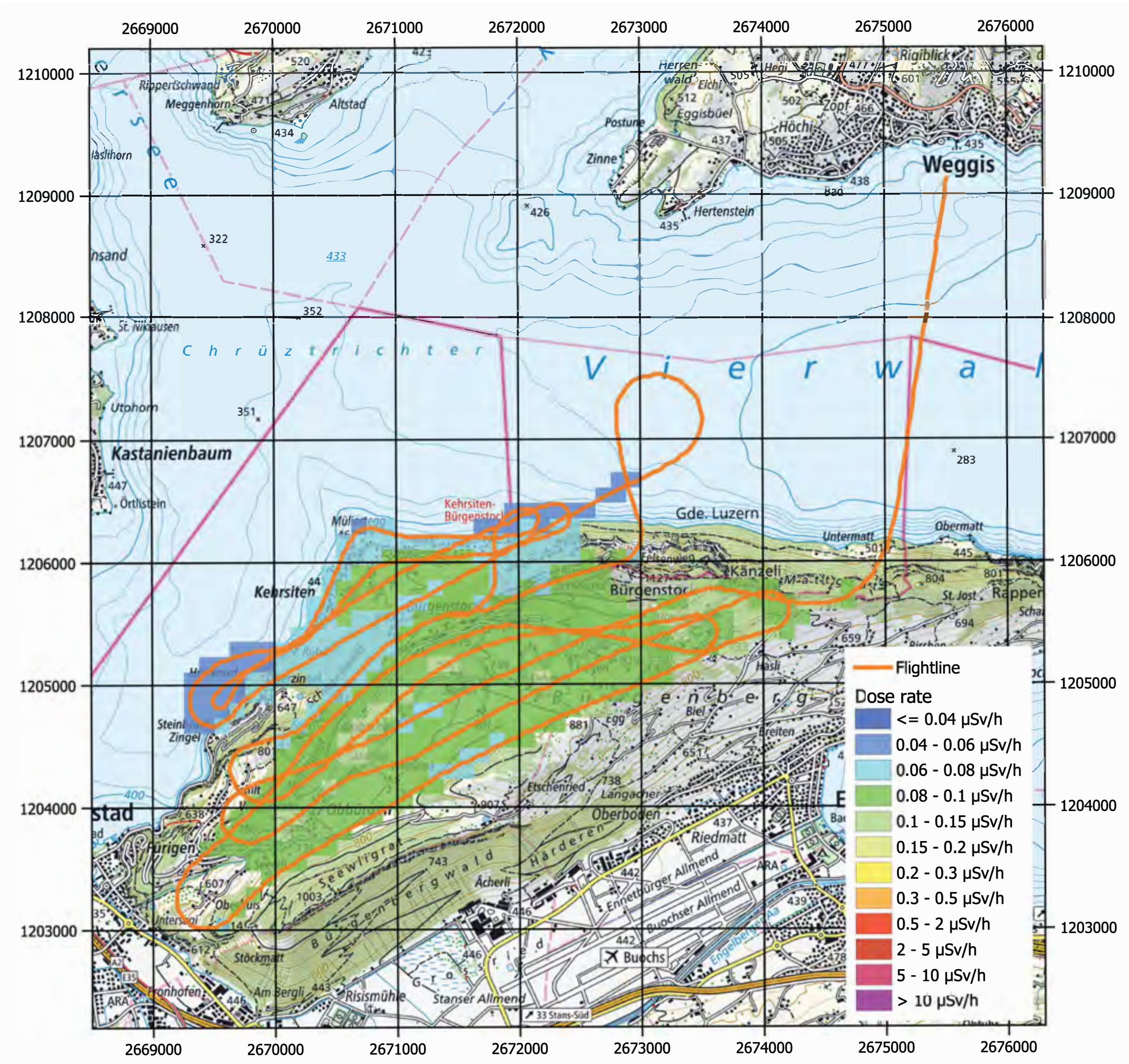

Figure 15: Dose rate measured at Bürgenstock. Geodata©Swisstopo.

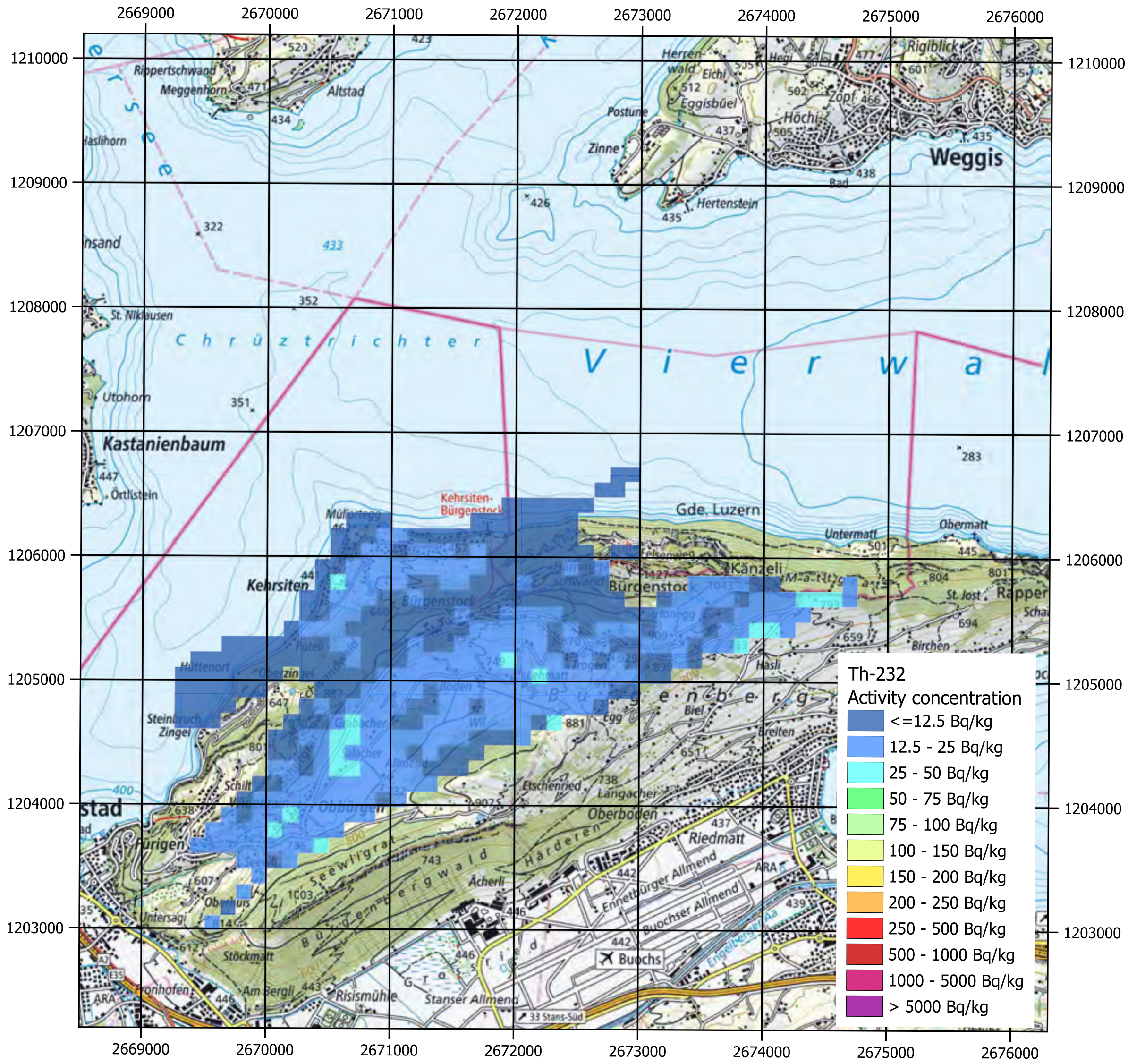

Figure 16: ^{232}Th activity concentration measured at Bürgenstock. Geodata©Swisstopo.

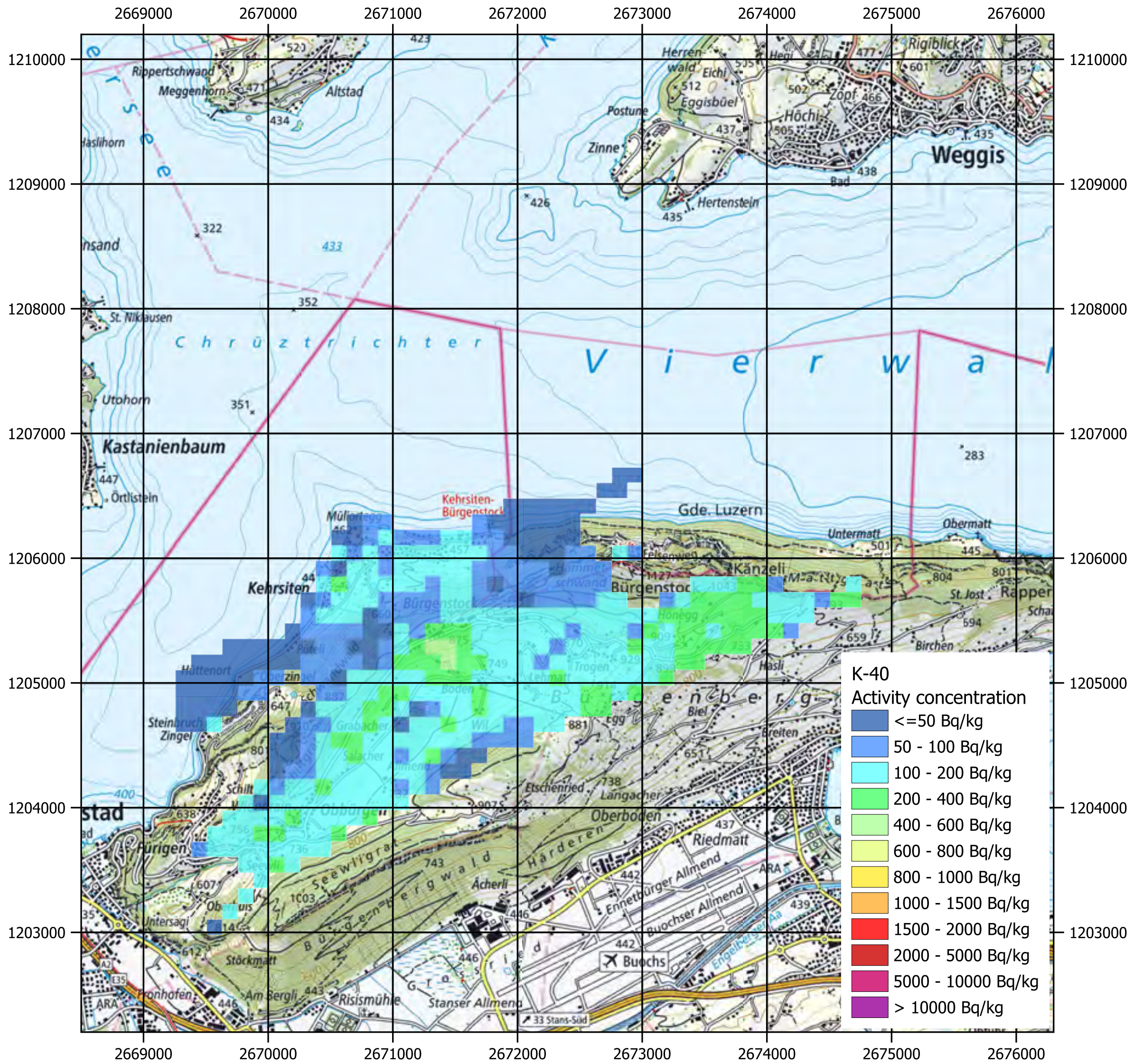

Figure 17: ^{40}K activity concentration measured at Bürgenstock. Geodata©Swisstopo.

3.1.2 Recurring measurements: PSI, KKB, KKL

Measurements of the area surrounding the nuclear power plants of Beznau and Leibstadt, the interim nuclear waste repository Zwilag and the Paul Scherrer institute were performed on two different days (29th and 31st May) with similar wet and mildly windy weather conditions. Due to adverse weather conditions during the scheduled national measurements ahead of AGC24, the German regions bordering Switzerland and the Leibstadt nuclear power plant could not be surveyed.

The dose rate map of Figure 18 shows values in line with previous measurements (PSI-Report 23-01): due to the water attenuation effect, lowest dose rates are found along the rivers Rhine and Aare. Marginally increased dose rates can be noticed over the Paul Scherrer institute (Figure 22), primarily due to annihilation radiation, and over the nuclear power plant of Leibstadt (Figure 21), due to ^{16}N, as measured and reported in the previous years. At the time of measurements, the nuclear power plant of Leibstadt was restarting activities after the yearly revision and was operated at a power of 25%, producing hence a much less marked contribution in the measurements with respect to the previous years, where the plant was operating at full power. All the anthropogenic emissions measured are allowed by the competent authorities and constantly monitored.
Slightly increased dose rate values are also found in the region of the "^{232}Th anomaly", situated in the area of Rotbergegg near the village of Mandach. This anomaly, also well known and documented in the previous reports, is characterised by a natural higher concentration of thorium, clearly recognisable in Figure 19.

In the MMGC-Ratio map shown in Figures 20 and 23, the contribution of β^+-emitting radionuclides released from the stack of the PSI West facility is clearly visible. During the measurements, eastward-blowing winds caused the detection of these radionuclides to be slightly displaced towards the east from the emission point of the stack. A closer comparison of Figures 22 and 23 reveals that the detection of these β^+ radionuclides in the MMGC map spatially corresponds with the region in the dose rate map where slightly elevated dose rates were measured over the eastern bank of the River Aare at PSI. This correlation is further supported by the spectrum shown in Figure 24, highlighted by the red line, which was acquired over the area showing higher MMGC-Ratio counts. The spectrum distincly exhibits the annihilation peak centred at 511 keV. In contrast, this peak is absent from the background spectrum, represented by the black line in Figure 24, which was obtained from measurements near the research institute, outside the region with elevated MMGC-Ratio counts.

In addition to the dose rate increase caused by the emitted β^+ radionuclides, Figure 22 shows elevated dose rates directly above the experimental hall building, which however do not correspond to increased MMGC-Ratio values in Figure 23. The spectrum acquired above the experimental building, depicted by the blue line in Figure 24, displays a skewed annihilation peak, suggesting the presence of ^{24}Ne, as indicated in previous reports (PSI-Report 23-01). It also shows an increased signal in the high-energy region of the spectrum, pointing to the presence of high-energy-emitting radionuclides. This high-energy signal results in lower MMGC-Ratio values despite the presence of the annihilation peak at lower energies, since the MMGC-Ratio is calculated as the ratio of low-energy to high-energy count rates.

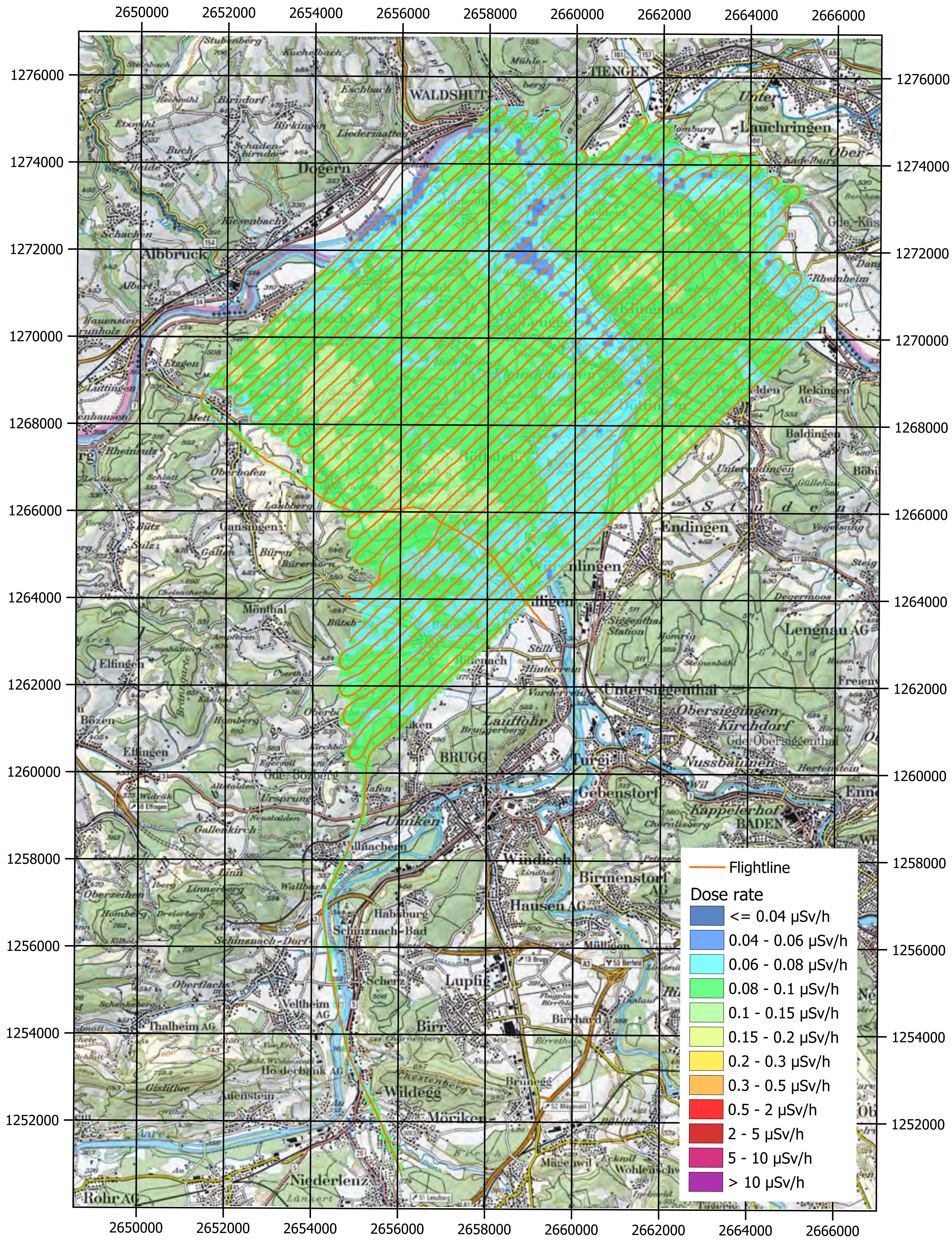

Figure 18: Dose rate measured in the area of PSI KKB and KKL. Geodata©Swisstopo.

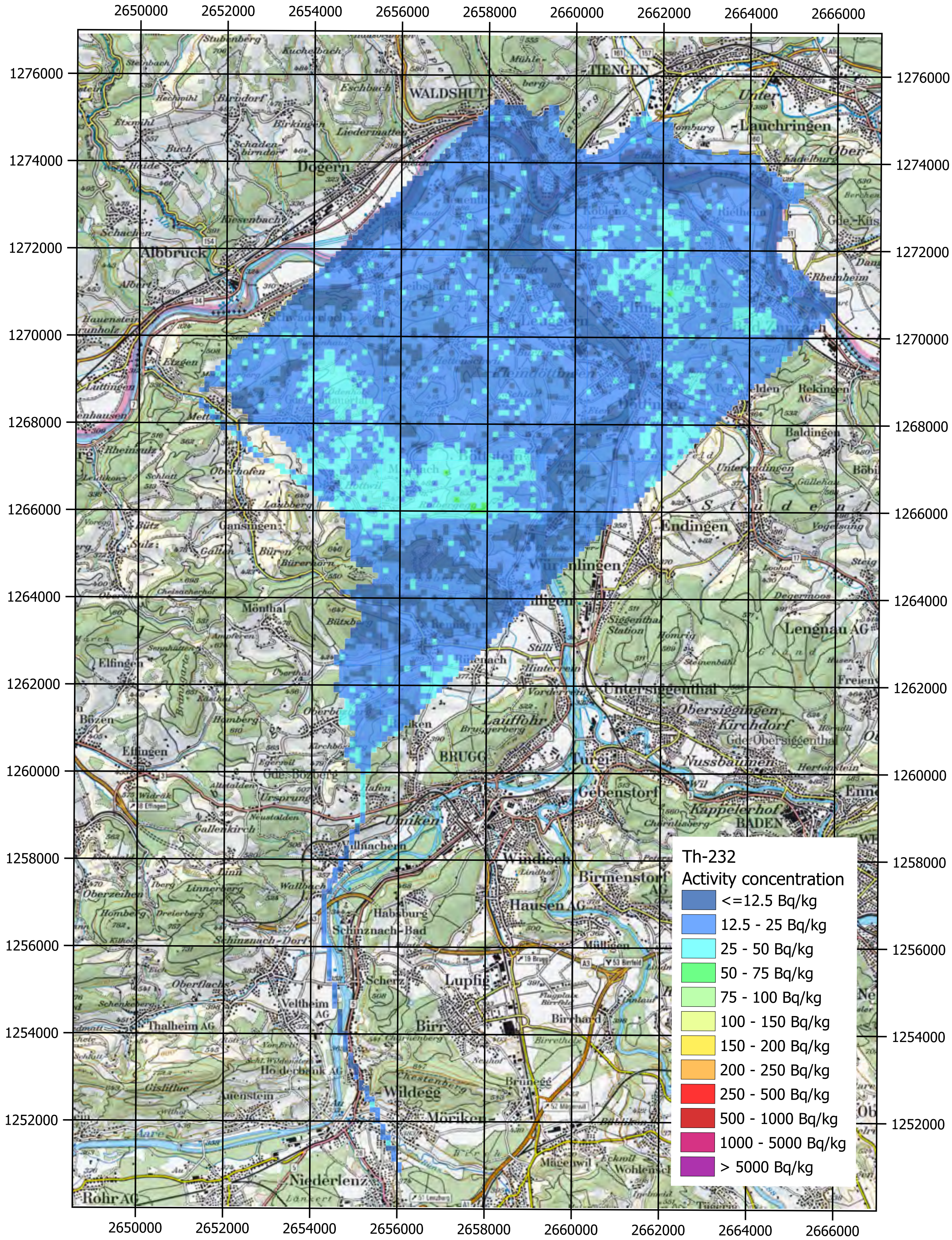

Figure 19: ^{232}Th activity concentration measured in the area of PSI KKB and KKL. Geodata©Swisstopo.

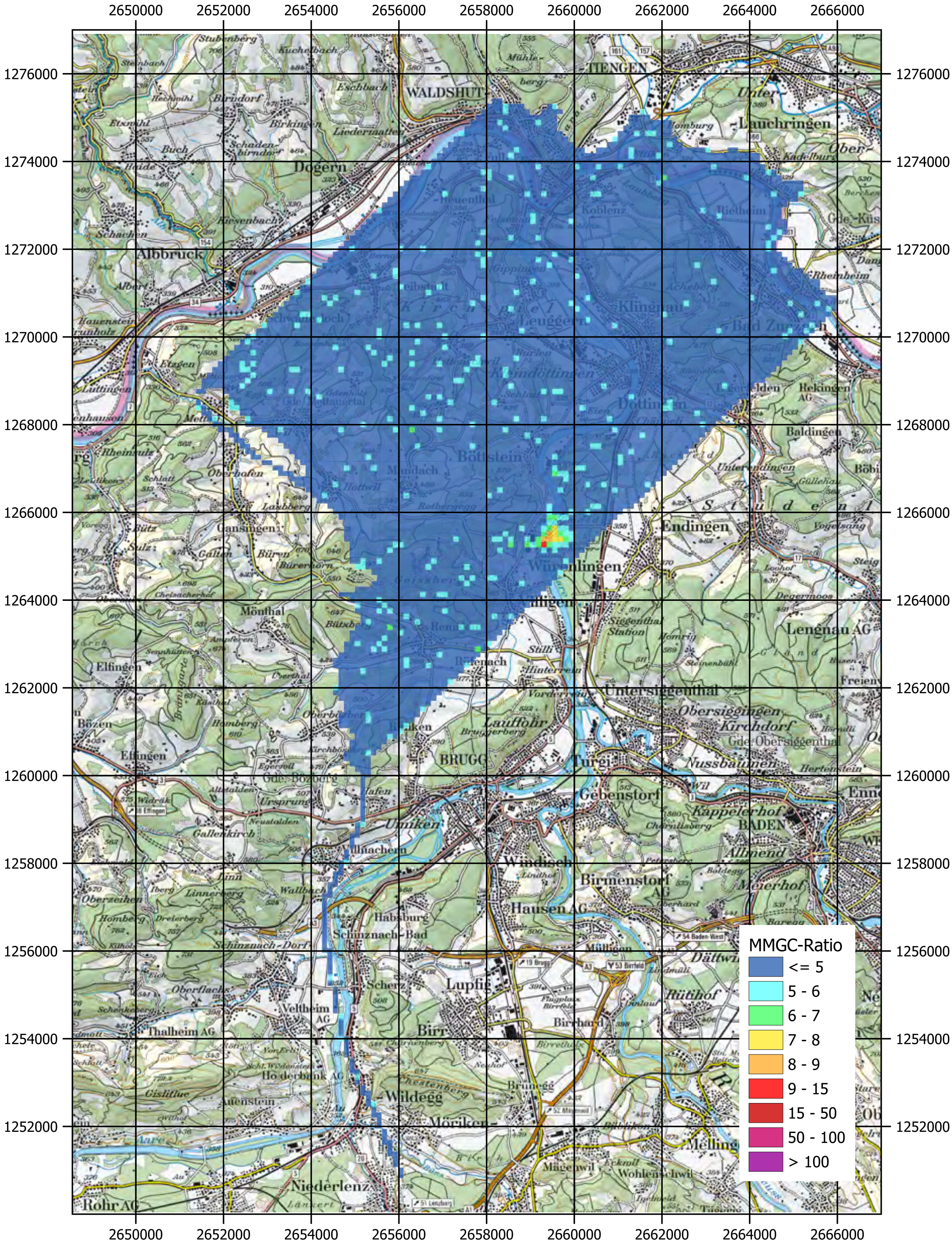

Figure 20: MMGC measured in the area of PSI KKB and KKL. Geodata©Swisstopo.

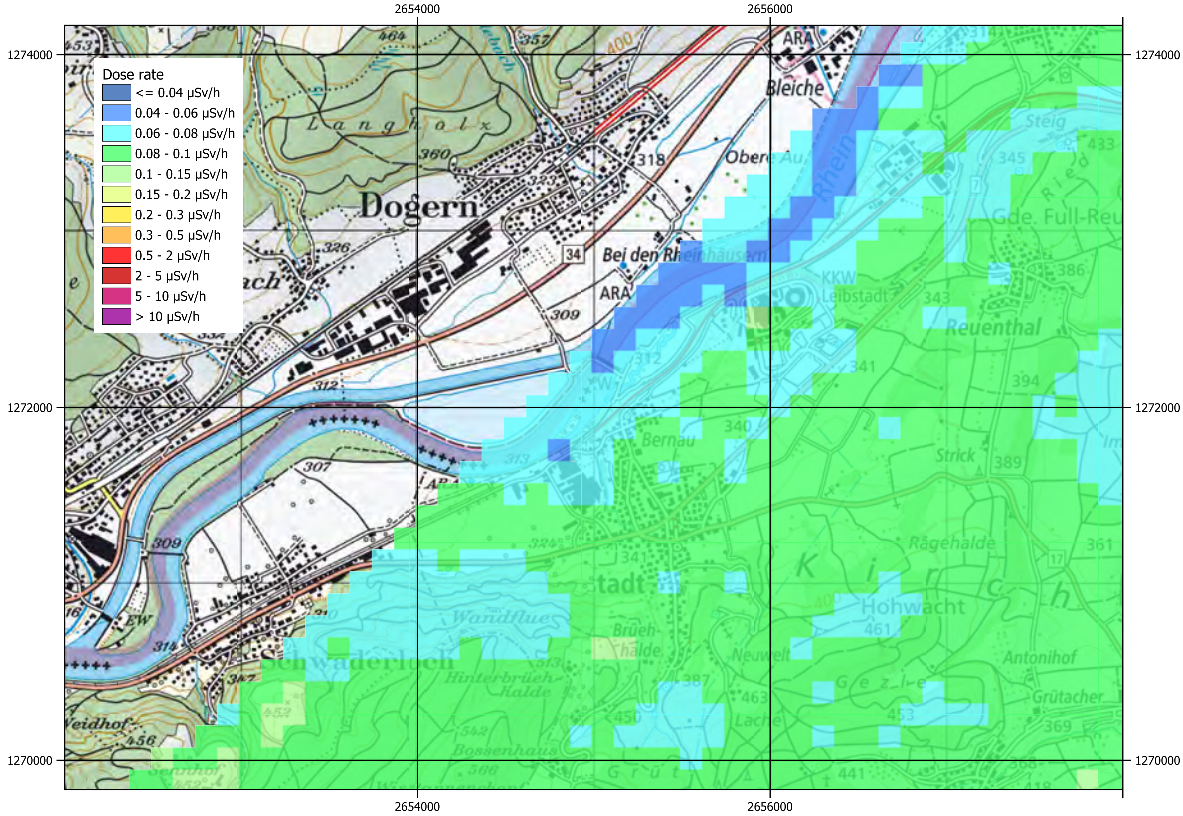

Figure 21: Dose rate measured at KKL. Geodata©Swisstopo.

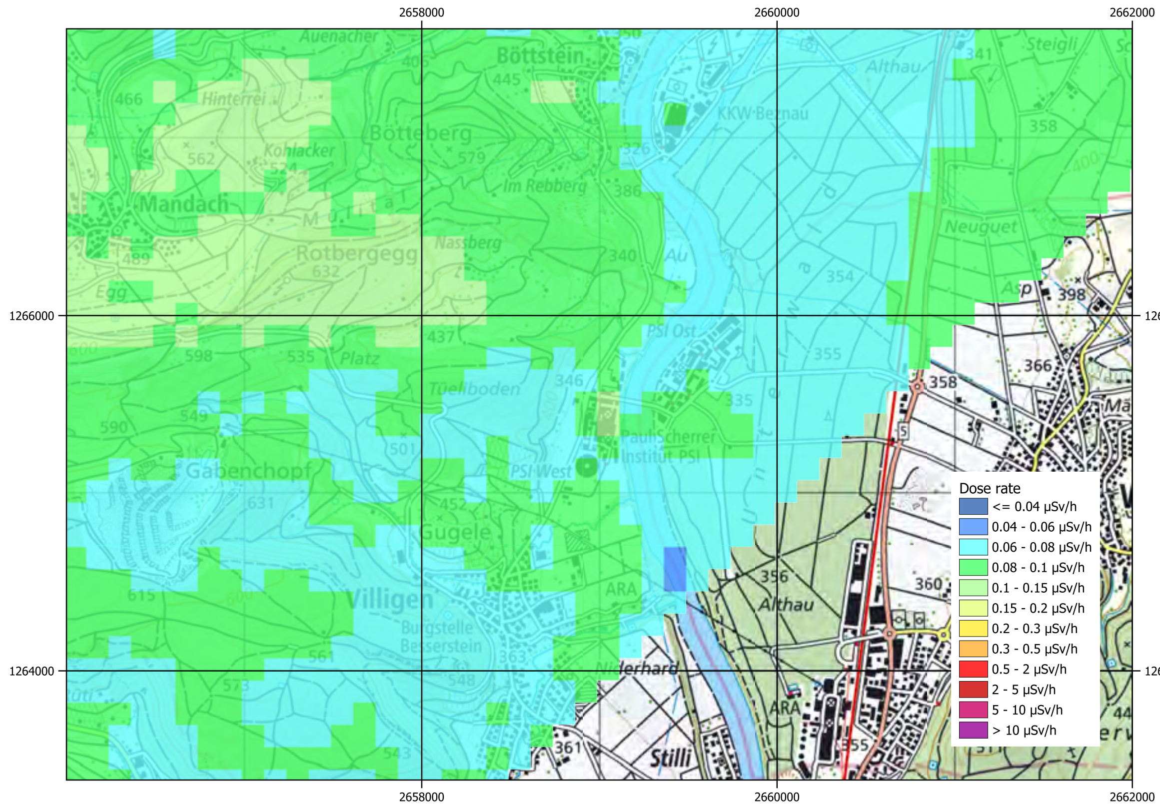

Figure 22: Dose rate measured at PSI. Geodata©Swisstopo.

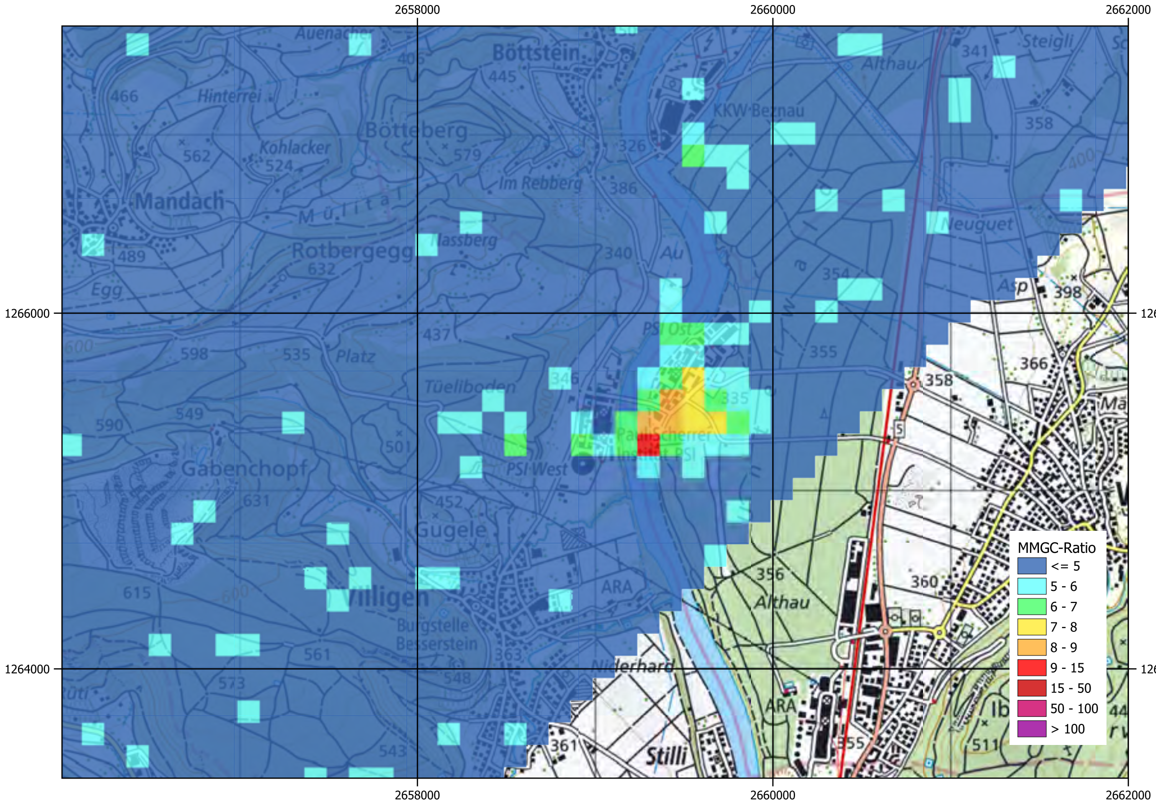

Figure 23: MMGC measured at PSI. Geodata©Swisstopo.

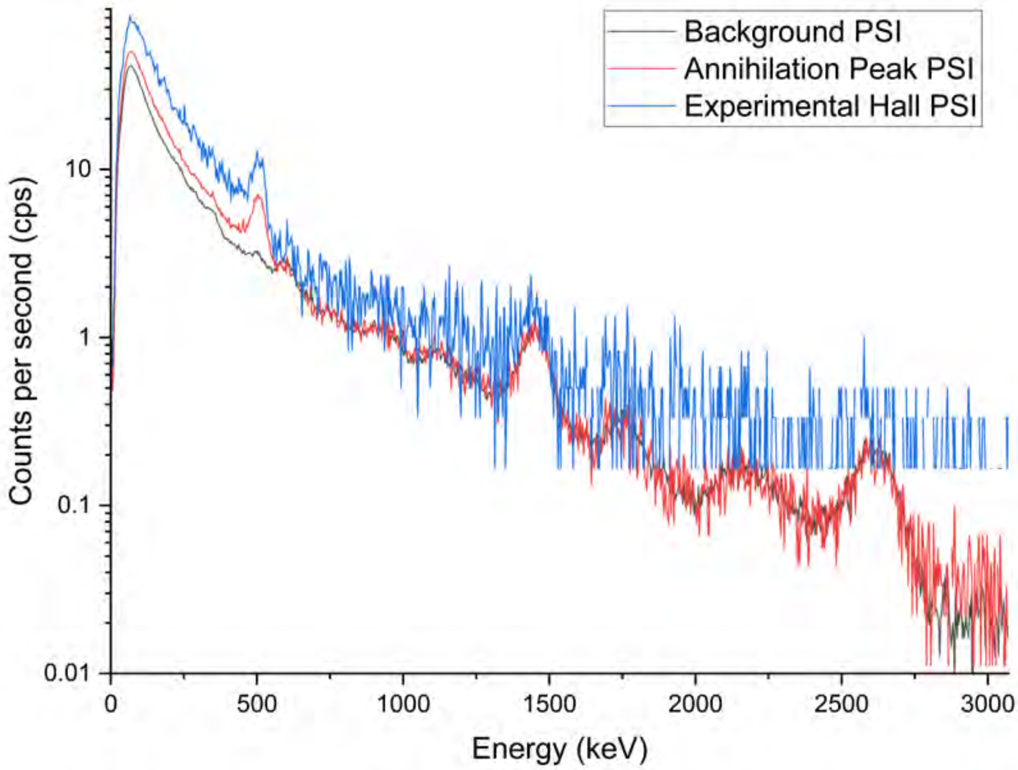

Figure 24: Spectra measured at PSI.

As the current data analysis software AGS_CH does not allow for the identification or quantification of atmospheric gamma-ray sources, the newly developed FSBI methodology described in Section 3.1.2 was applied to investigate the origin of the high-energy spectral component over PSI West and to confirm the presence of ^{24}Ne. Specifically, we performed FSBI for the eight pulse-height spectra recorded in the acquisition channel (sum channel) that showed the highest elevated dose rates over the PSI West facilities, each having an acquisition real time $\Delta t = 1\,\mathrm{s}$ (see Figure 25). Given the unknown origin of the high-energy spectral component over PSI West, various source models were tested using FSBI and Bayesian model comparison. The baseline model included the known source terms, i.e. the natural terrestrial radioactive elements K_{nat}, Th_{nat}, and U_{nat}, along with atmospheric β^+ radionuclides. Intrinsic, cosmic-ray, and radon backgrounds were estimated empirically from measured pulse-height spectra acquired on the same survey flight downstream of the Aare river ($\sim 10^3$ m from PSI West). Since no active monitoring for airborne gamma-ray emitting radionuclides, apart from the β^+ emitters, is currently conducted at PSI, we relied on expert input from members at the Department of Radiation Safety and Security to identify the most likely high-energy gamma-ray source candidates. Radionuclide sources that could give rise to the observed high-energy spectral component are atmospheric ^{16}N, ^{87}Kr, and ^{137}Xe emitted via the central exhaust air systems at PSI West. In addition to these atmospheric sources, terrestrial ^{16}N accumulated in the cooling water of the Ultra Cold Neutron Source (UCN) facility could also account for the high-energy spectral component observed over PSI West. Based on this expert input, we defined four candidate source models, each including the baseline model combined with the suspected atmospheric ^{24}Ne and one of the aforementioned high-energy gamma-ray emitting radionuclides, i.e. ^{16}N (atmospheric/terrestrial), ^{87}Kr (atmospheric), and ^{137}Xe (atmospheric). Using FSBI to evaluate all candidate source models, the retrieved Bayes factors $\log(B_{1,0})$ provide decisive evidence on the Jeffreys' scale in favour of terrestrial ^{16}N as the most likely explanation for the observed high-energy component in the spectrum over PSI West ($\log(B_{1,0}) > 5$, significance $>3.5\sigma$). Currently, in-situ gamma-ray spectroscopic measurements are being conducted by the Department of Radiation Safety and Security to confirm the presence of ^{16}N at the UCN facility. To assess the significance of the individual anthropogenic source terms within the fiducial source model (baseline combined with atmospheric ^{24}Ne and terrestrial ^{16}N), we performed again Bayesian model comparison. This involved systematically comparing the fiducial model against reduced models obtained by sequentially excluding each anthropogenic term. We found decisive evidence on the Jeffreys' scale for the presence of terrestrial ^{16}N ($\max\log(B_{1,0}) = 113.512(2)$, significance $>15.2084(1)\sigma$) and atmospheric β^+ ($\max\log(B_{1,0}) = 15.772(1)$, significance $>5.8385(2)\sigma$). Additionally, very strong evidence was found for atmospheric ^{24}Ne ($\max\log(B_{1,0}) = 3.902(1)$, significance $>3.0646(4)\sigma$). These results are also highlighted in Figure 26 alongside the retrieved maximum a posteriori (MAP) point estimates for the source strengths and the net count rate pulse-height spectra. Analysis of the temporal evolution of the source strengths reveals expected trends for both anthropogenic terrestrial and atmospheric sources. For the atmospheric ^{24}Ne and β^+ radionuclides, activity concentrations show a gradual rise, followed by a sudden decrease — a typical pattern observed during flights through the plume of anthropogenic airborne radionuclides opposite the wind direction. The activity for the terrestrial ^{16}N point source is symmetric around the maximum between 13:56:19 UTC and 13:56:21 UTC, corresponding to the most likely location of the point source and aligning with the location of the UCN facility (see Figure 25).

In addition to the temporal analysis, we present a spectral analysis in Figure 27 for the four pulse-height spectra that contain the peak source strengths for the anthropogenic atmospheric and terrestrial sources over the PSI West facilities between 13:56:17 UTC and 13:56:21 UTC. Both the left-skewed annihilation peak at $\sim$511 keV in Sub-figures (a) and (b), as well as the high-energy spectral component above $\sim$2.7 MeV in Sub-figures (c) and (d) are successfully described by the inferred fiducial source model.

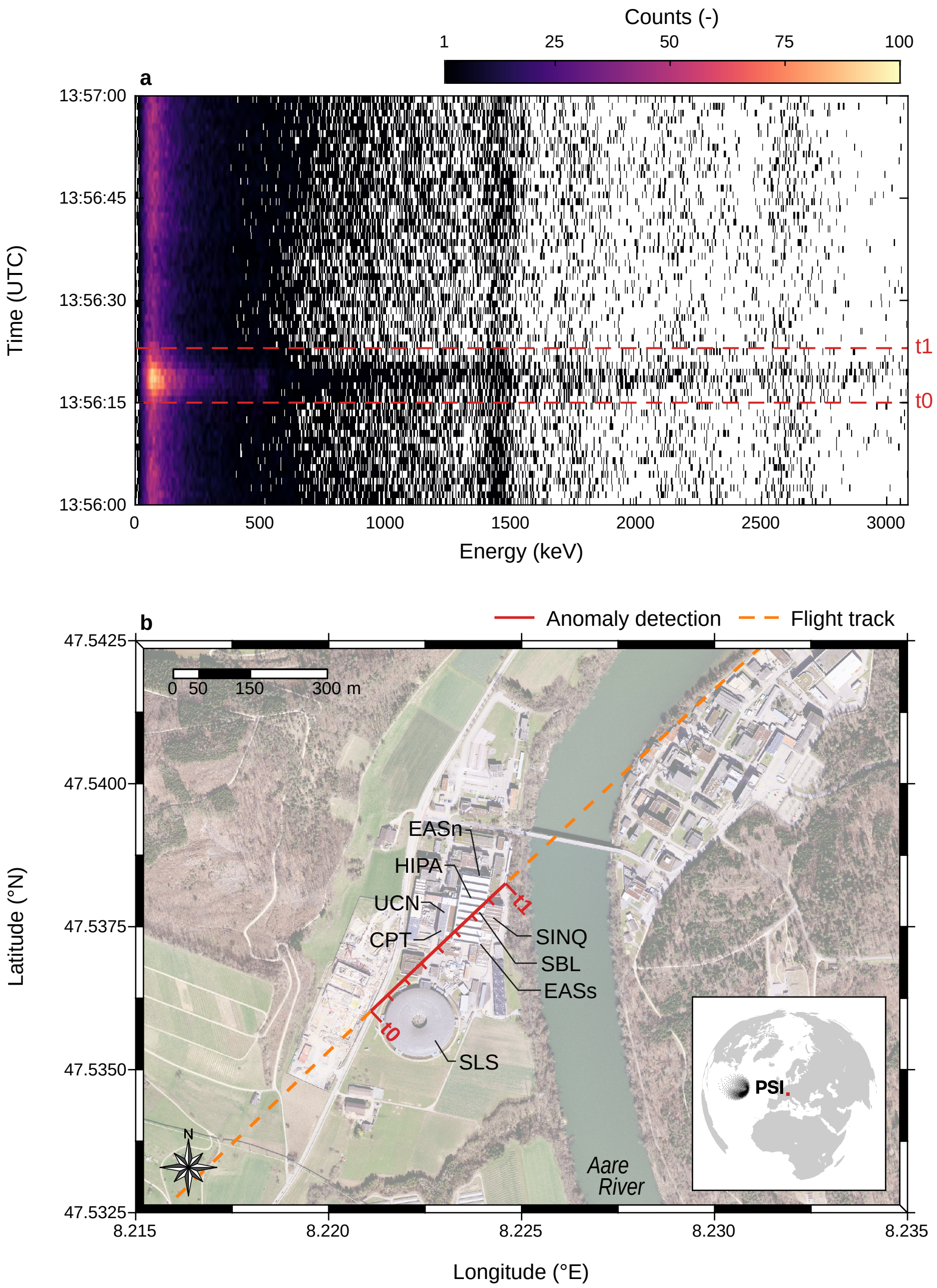

Figure 25: Anomaly detection over PSI West. (a) Waterfall plot illustrating the measured counts acquired as a function of spectral energy and time, corresponding to the flight track depicted in Sub-figure (b). The temporal range, analysed with FSBI to assess the detected anomaly, spans from t0 = 13:56:15 UTC to t1 = 13:56:23 UTC on May 29, 2024. (b) Flight track over PSI West, with the evaluated anomaly region highlighted. Key infrastructures known to produce or emit ionizing radiation are indicated: HIPA: High Intensity Proton Accelerator, SBL: Secondary Beam Lines, SINQ: Swiss Spallation Neutron Source, SLS: Swiss Light Source, UCN: Ultra Cold Neutron Source, CPT: Center for Proton Therapy, EASn: Exhaust Air System north, EASs: Exhaust Air System south. The displayed map was generated using the `m_map` software package (Pawlowicz et al., 2020). Geodata©Swisstopo.

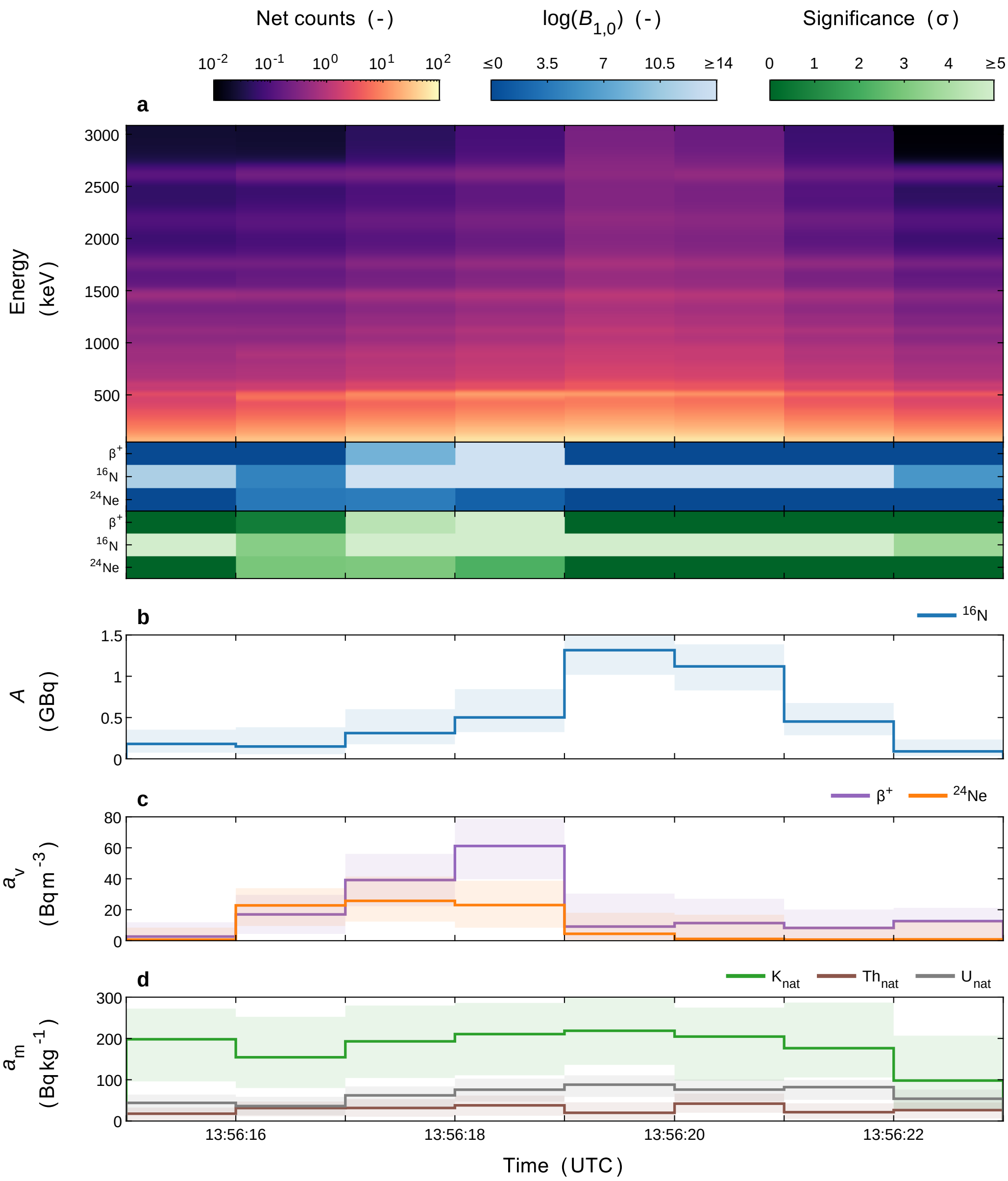

Figure 26: Temporal analysis of the anomaly detected over PSI West. In these graphs, we present the source strengths inferred by FSBI of the six sources considered in the fiducial model as a function of time. (a) Point posterior prediction for the net count rate are displayed as a function of time and spectral energy alongside log Bayes factors ($\log(B_{1,0})$) and sigma values (σ), characterising the significance of the individual anthropogenic gamma-ray sources, i.e. the atmospheric β^+ and ^{24}Ne radionuclides, as well as the terrestrial ^{16}N point source. (b–d) Source strength time evolutions are shown for the terrestrial ^{16}N point source (activity A), the atmospheric β^+ and ^{24}Ne sources (activity volume concentration a_v), and the three natural terrestrial radionuclides K_{nat}, Th_{nat}, and U_{nat} (activity mass concentration a_m). Source strengths are displayed as point posterior predictions derived by the MAP estimates (solid line) and 95 % credible intervals (shaded area).

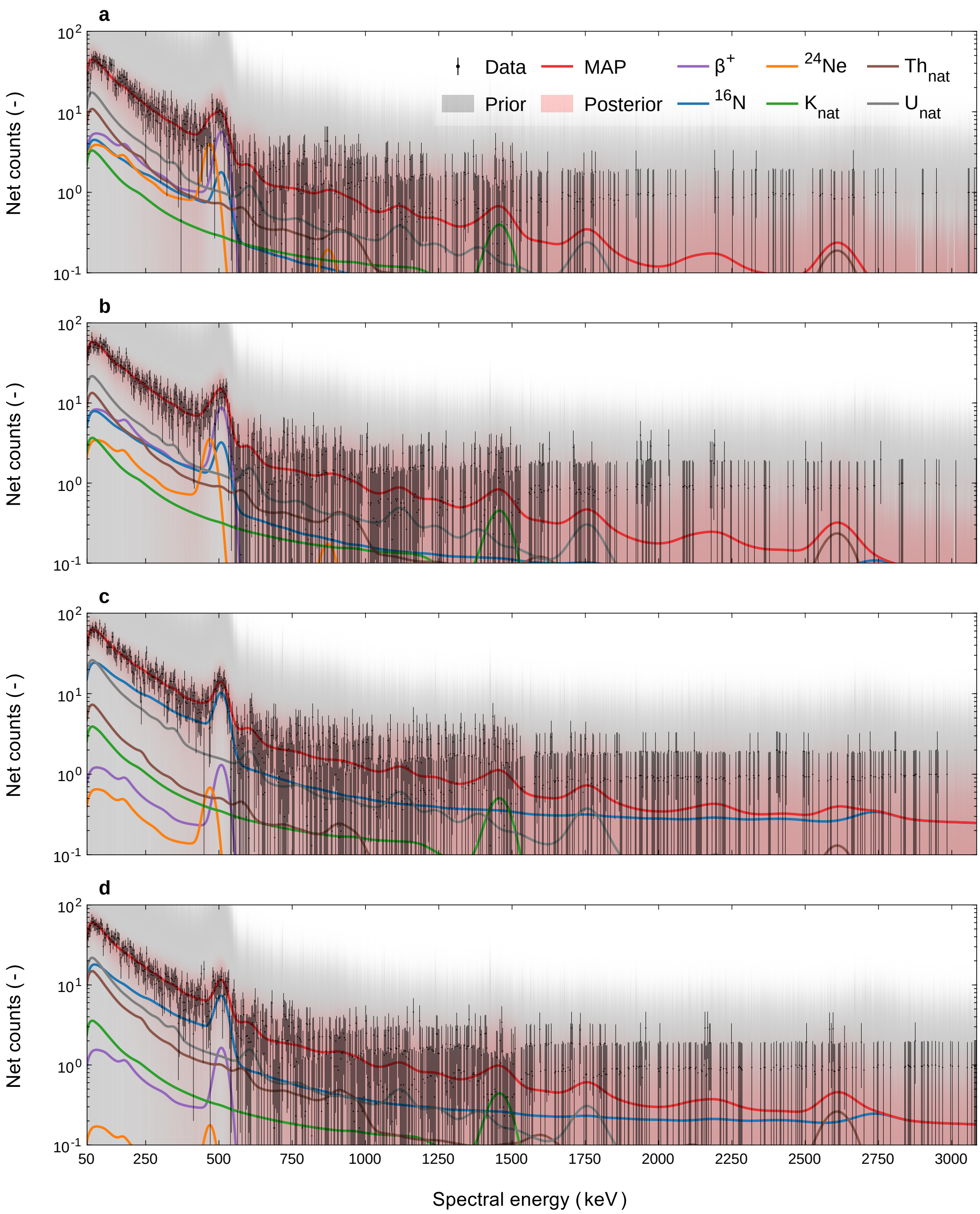

Figure 27: Spectral analysis of the anomaly detected over PSI West. In these graphs, we present prior and posterior predictive distributions (colour-coded) obtained by FSBI alongside the measured pulse-height spectra, each having an acquisition real time $\Delta t = 1\,\mathrm{s}$, with the measurement start time being 13:56:17 UTC to 13:56:20 UTC for the Sub-figures (a)–(d), respectively. For the measured spectra, uncertainties are indicated as one standard deviation of the mean values. In addition to the posterior predictive distributions, we also display the point posterior predictions derived by the MAP estimates (red line). The spectral signatures scaled by the MAP source strengths and the acquisition live time for all six sources considered in the fiducial model are indicated: the atmospheric β^{+} and ^{24}Ne sources, a generic terrestrial ^{16}N point source as well as the three natural terrestrial radionuclides K_{nat}, Th_{nat}, and U_{nat}. All spectral quantities were empirically corrected for the intrinsic, radon, and cosmic-ray backgrounds.

3.1.3 Concise

The map of the total dose rate in Figure 28 illustrates a typical pattern along lake coastlines, characterised by the attenuation of the dose from terrestrial radionuclides over water bodies. The recorded dose rate values are consistent with those observed in adjacent regions during previous measurement campaigns (PSI-Report 24-02). The maps of ^{232}Th and the MMGC, shown respectively in Figures 29 and 30, also display typical values, with ^{232}Th activity concentrations below 50 Bq/kg and MMGC ratios under 6.

In the coastal area between the towns of Concise and Yverdon-les-Bains, an area with elevated concentrations of ^{40}K is evident in Figure 31. This increased ^{40}K activity correlates well with the geology of the region (Figure 32 and 33), which is characterised by glacial moraines.

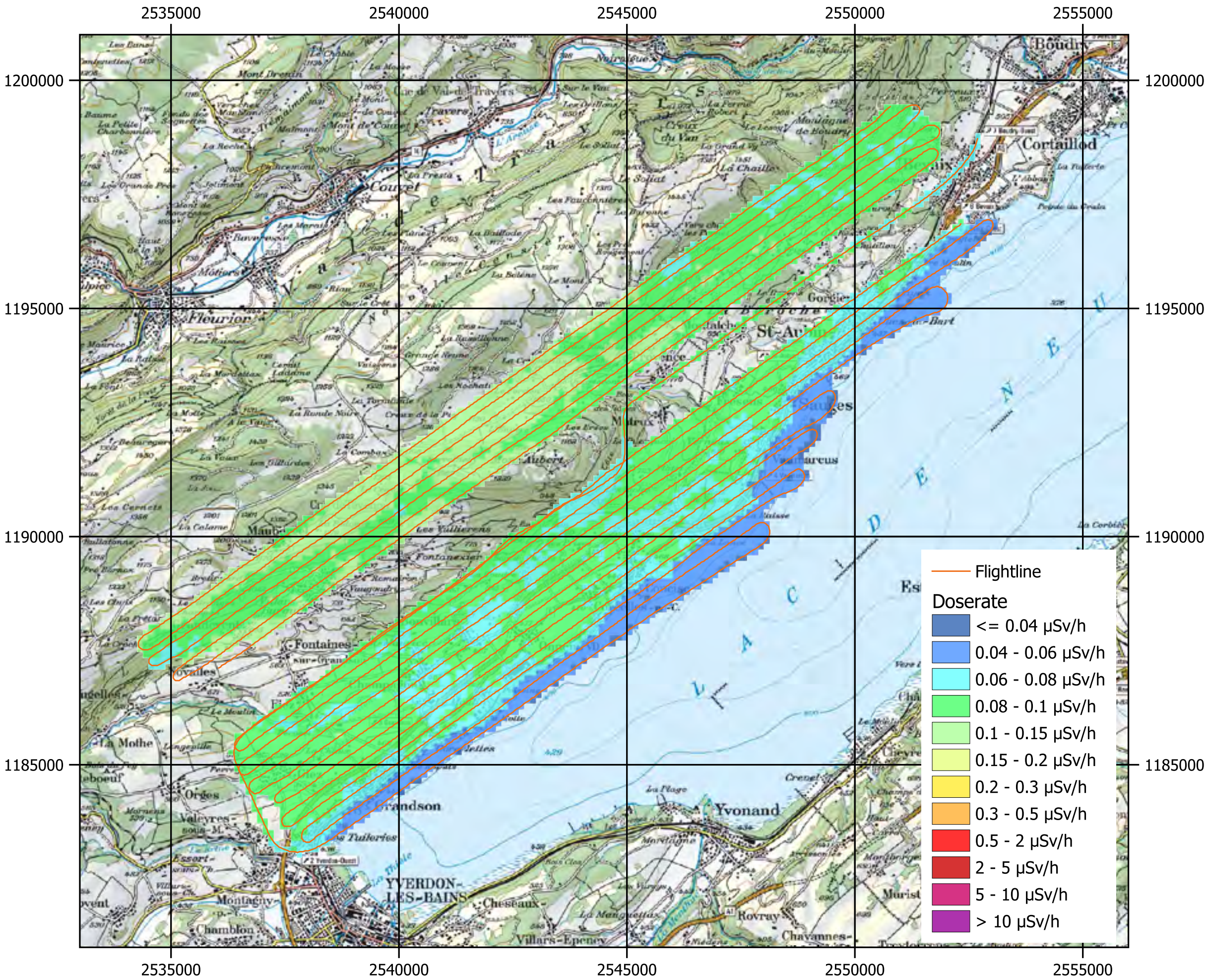

Figure 28: Dose rate measured in the area of Concise. Geodata©Swisstopo.

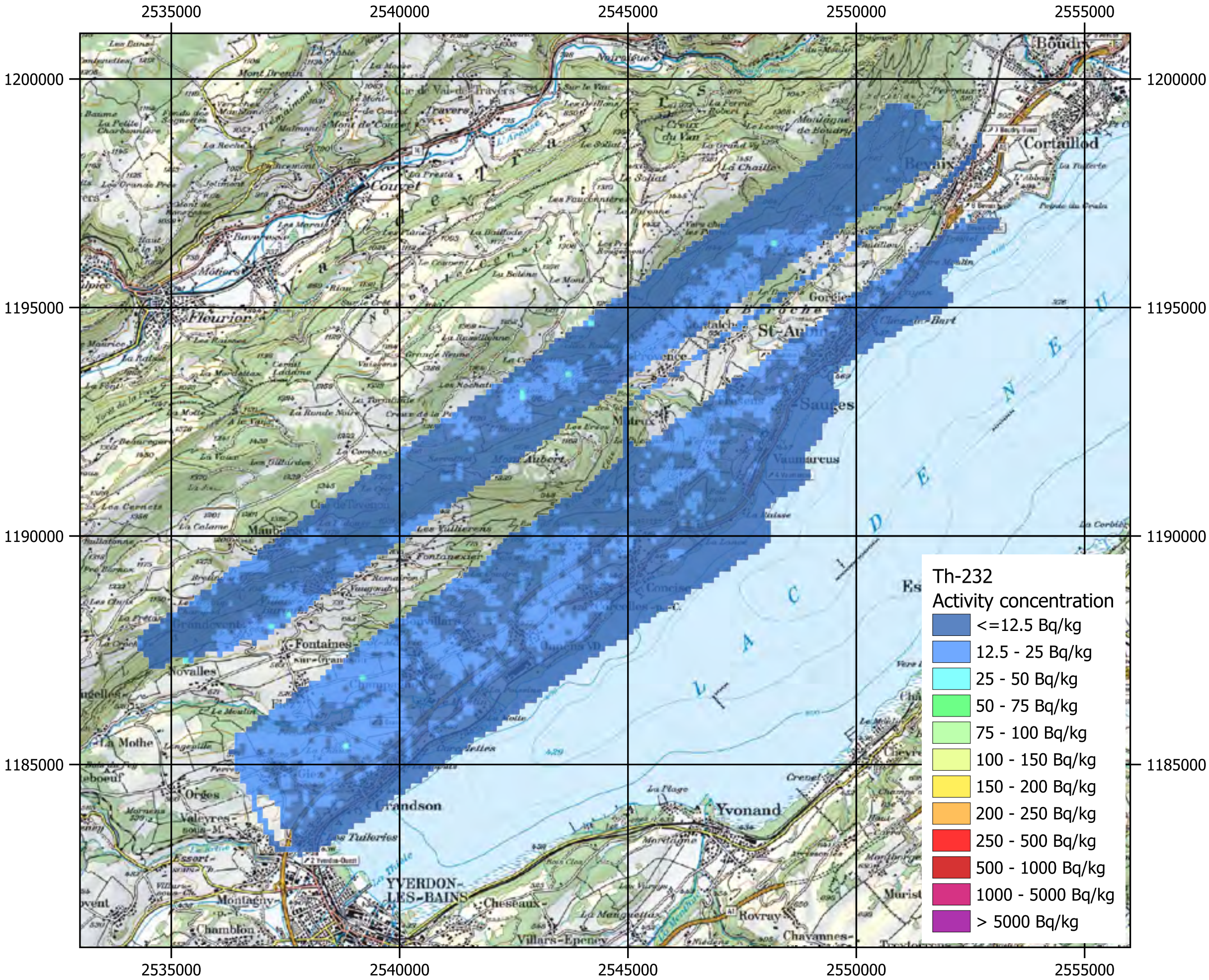

Figure 29: ^{232}Th activity concentration measured in the area of Concise. Geodata©Swisstopo.

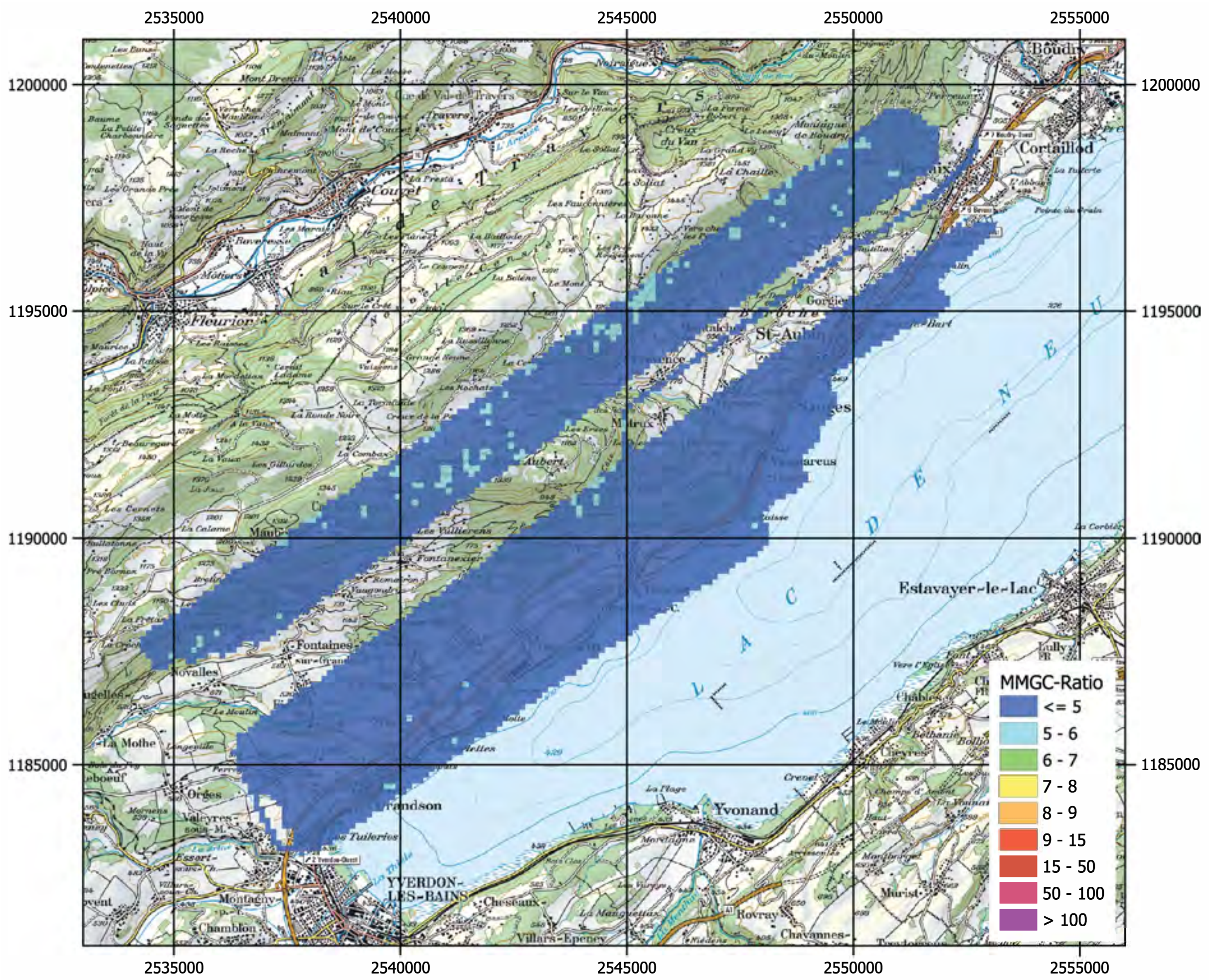

Figure 30: MMGC measured in the area of Concise. Geodata©Swisstopo.

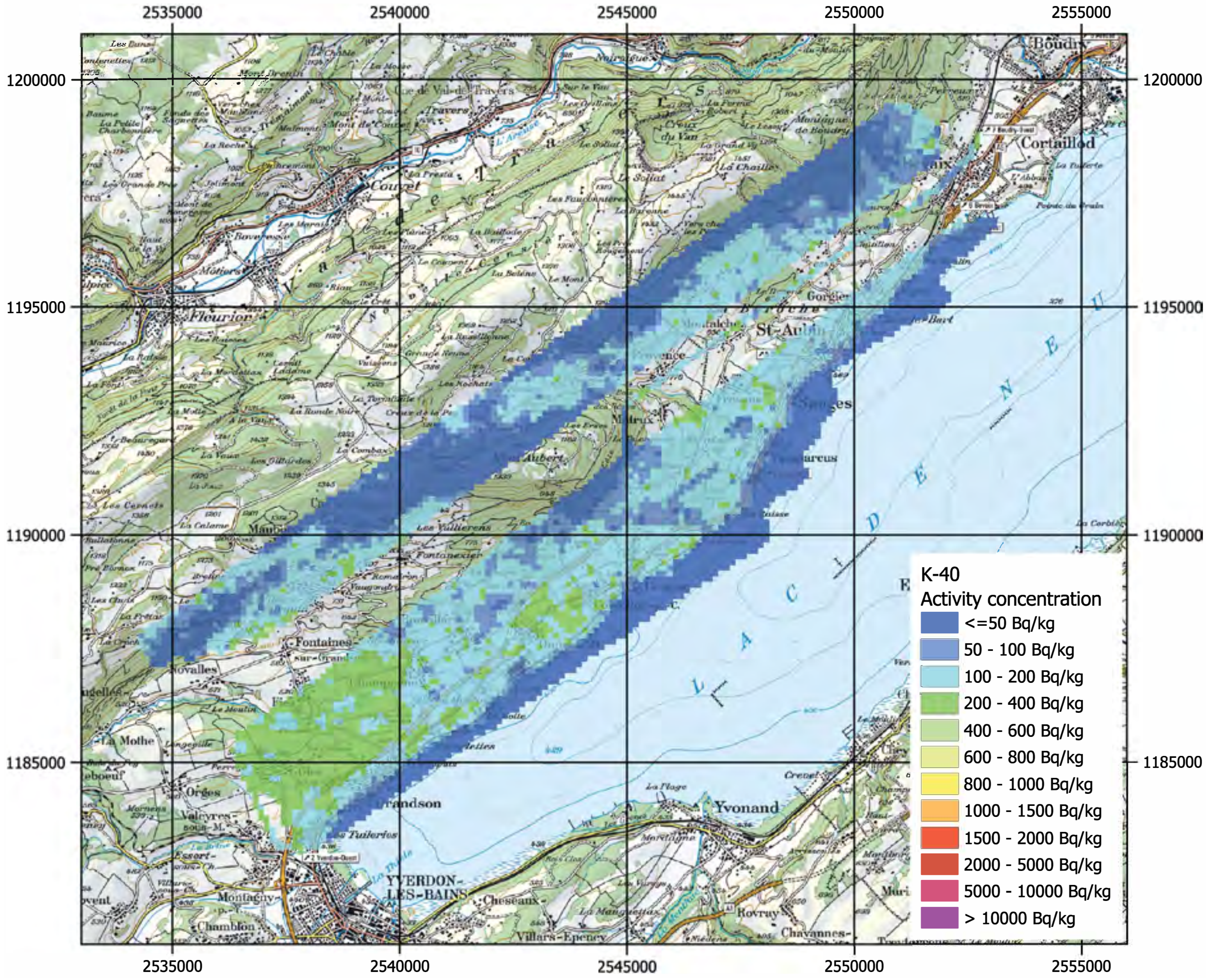

Figure 31: ^{40}K activity concentration measured in the area of Concise. Geodata©Swisstopo.

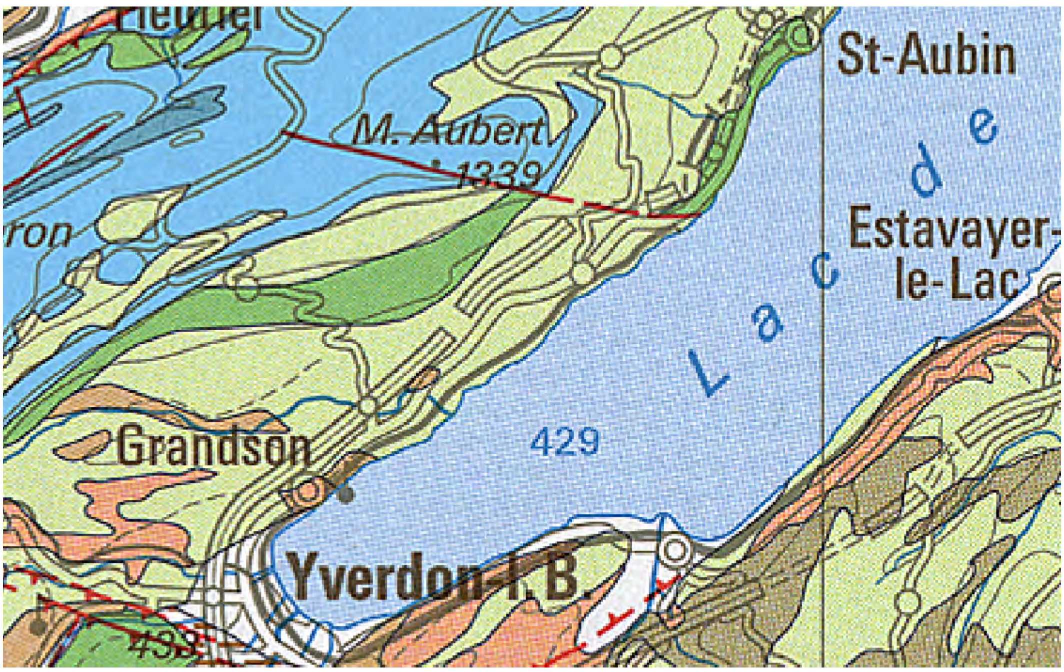

Figure 32: Geological map of the area of Concise.Geodata©Swisstopo.

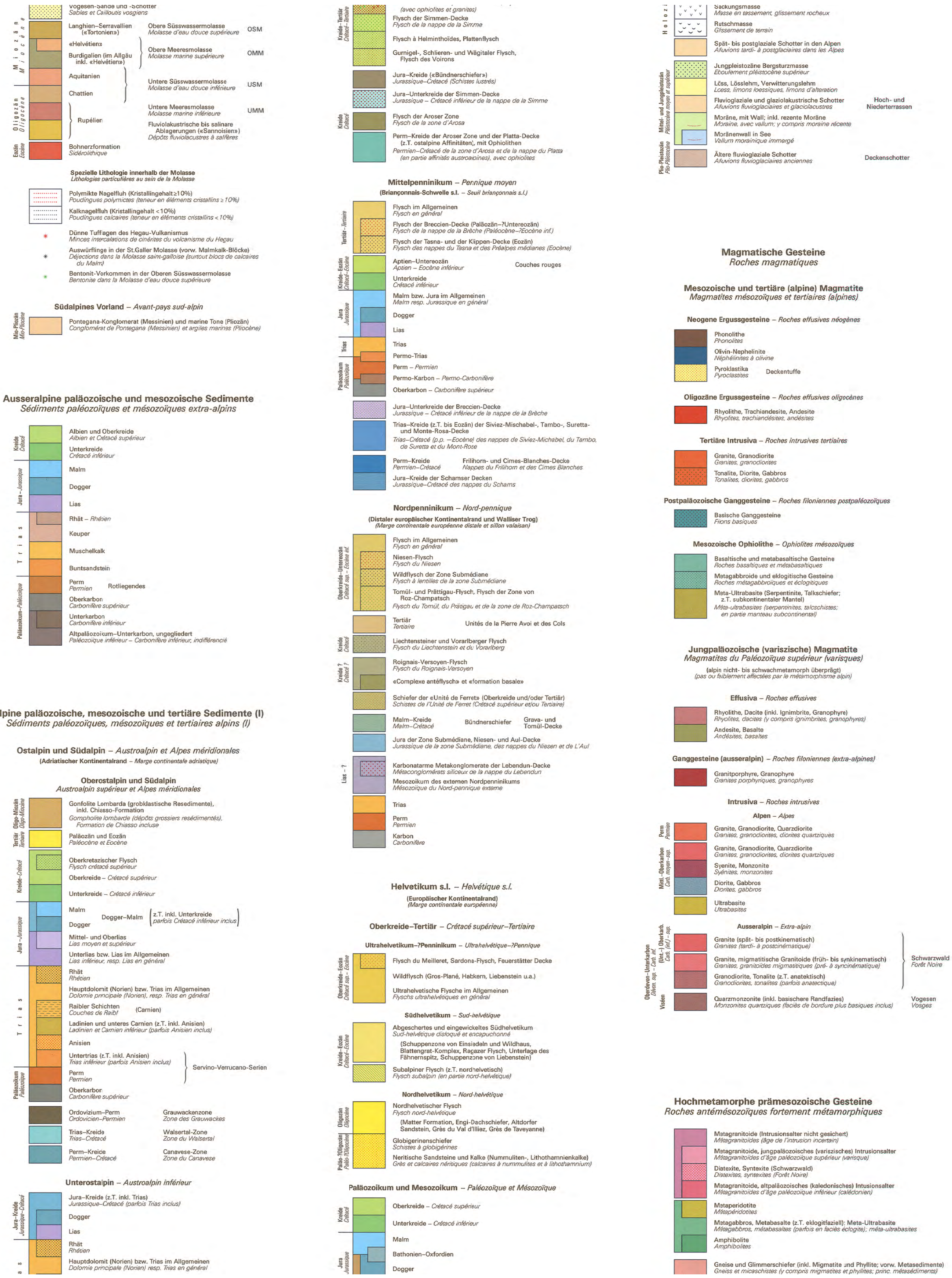

Figure 33: Legend of Geological map.Geodata©Swisstopo.

3.1.4 Ecuvillens

Ordinary dose rates (<0.15 µSvh) have been measured in the region of Ecuvillens and are illustrated in the map of Figure 34. The ^{232}Th activity concentration and the MMGC-Ratio, measured over the small region surrounding the local airport, do not show remarkable values, as reported in Figures 35 and 36.

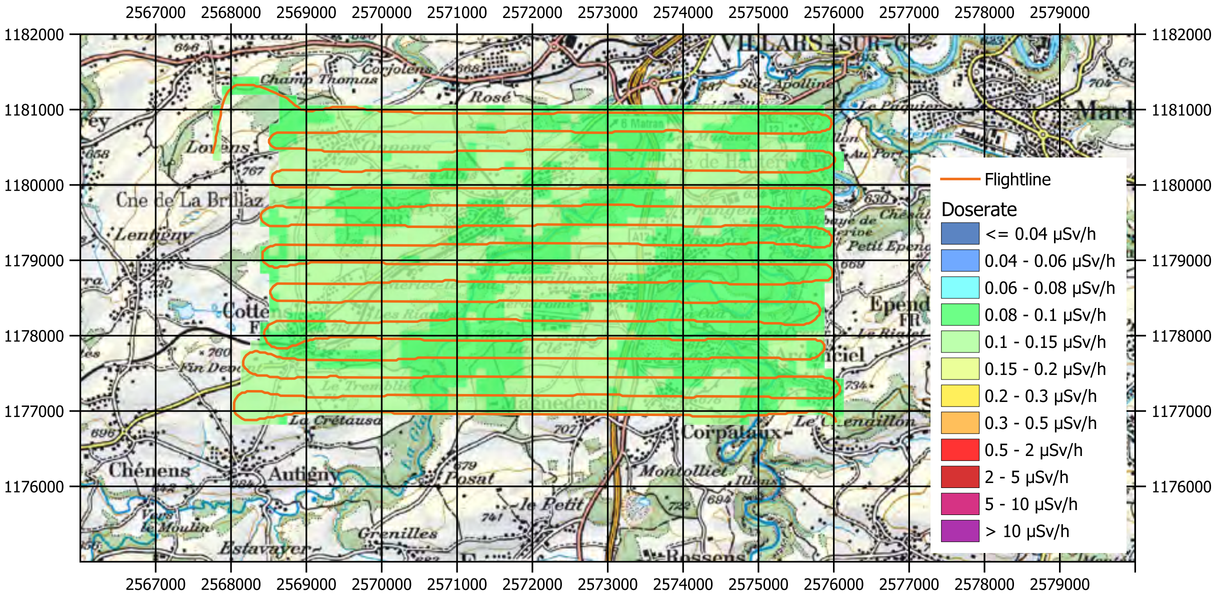

Figure 34: Dose rate measured in the area of Ecuvillens. Geodata©Swisstopo.

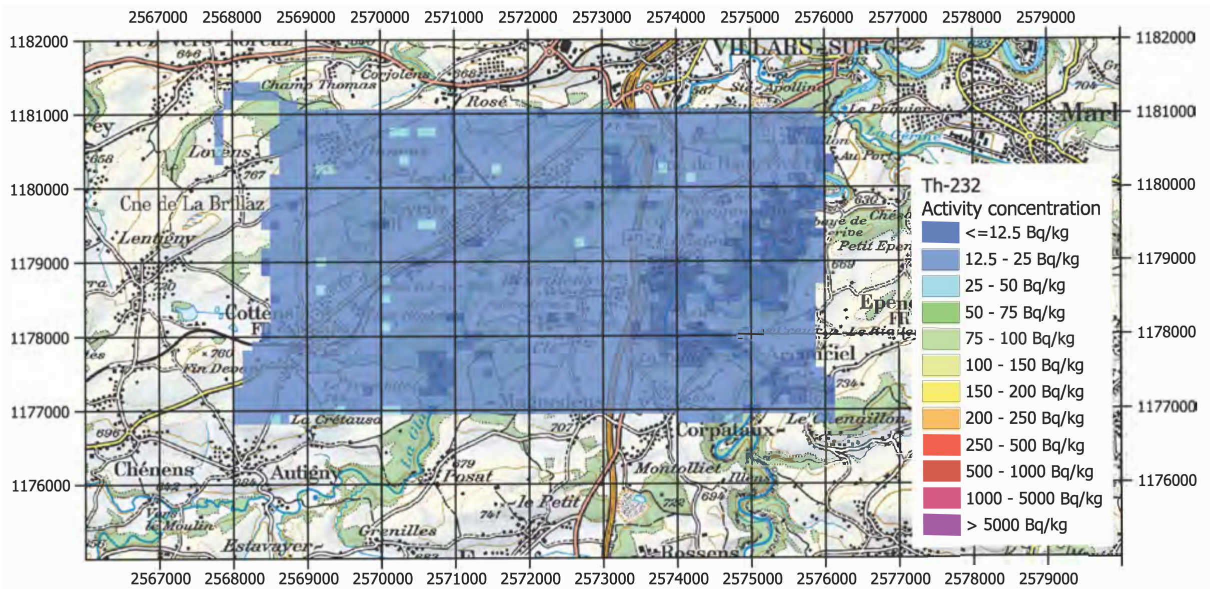

Figure 35: ^{232}Th activity concentration measured in the area of Ecuvillens. Geodata©Swisstopo.

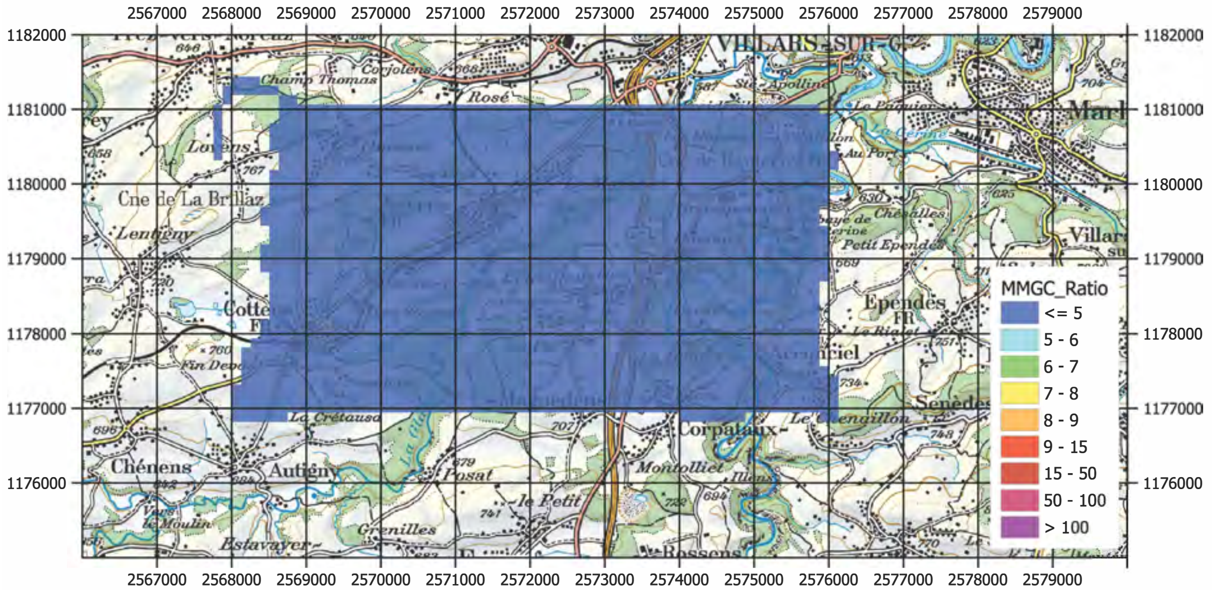

Figure 36: MMGC measured in the area of Ecuvillens. Geodata©Swisstopo.

3.1.5 Fleurier

Measurements over the Fleurier region, extending up to the border with France, indicate uniform dose rate values (37). The ^{232}Th and ^{40}K activity concentration maps shown in Figures 38 and 39 reveal marginally higher values in regions associated with glacial deposits.

Traces of ^{137}Cs have been detected in the Fleurier area; their presence, previously documented in adjacent regions (PSI-Report No. 22-02), is attributed to the Chernobyl fallout. Slightly higher values are observed in the areas of Saint-Sulpice and to the east and south of Lac des Taillères. These can be seen in both the ^{137}Cs activity concentration map (Figure 40) and the MMGC-ratio map displayed in Figure 41. The detected ^{137}Cs concentrations remain very low and pose no radiological concern.

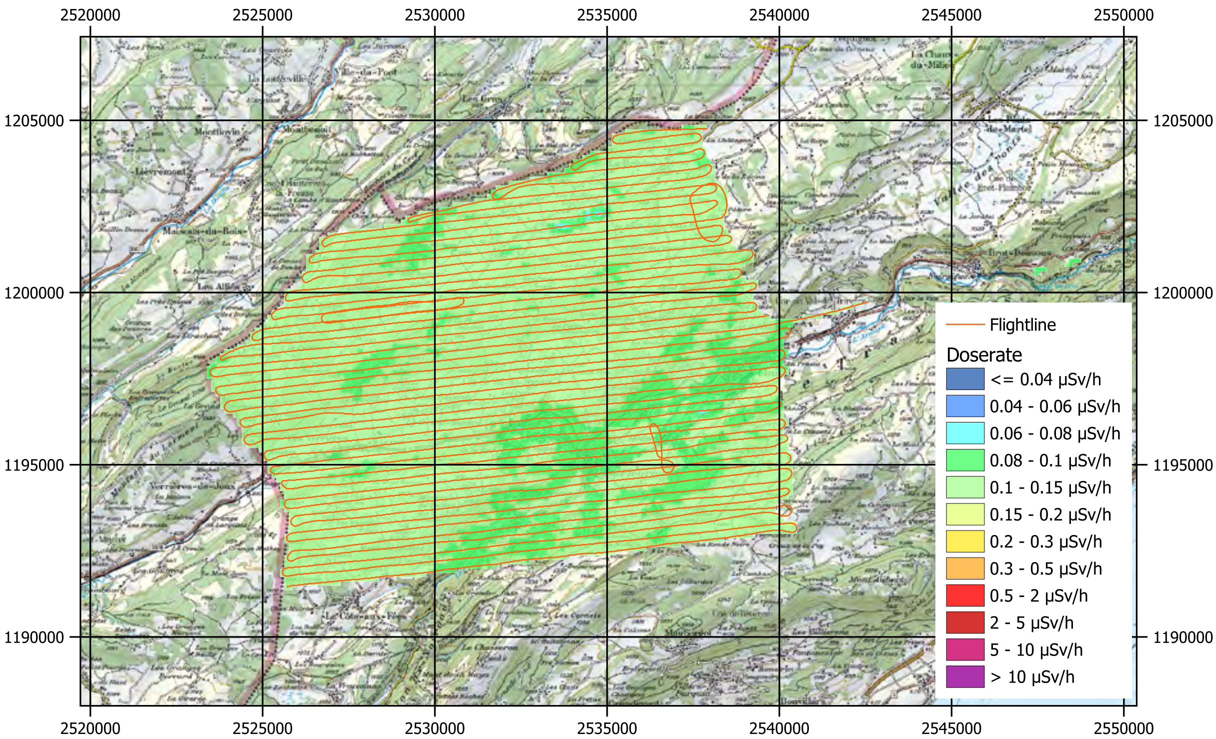

Figure 37: Dose rate measured in the area of Fleurier. Geodata©Swisstopo.

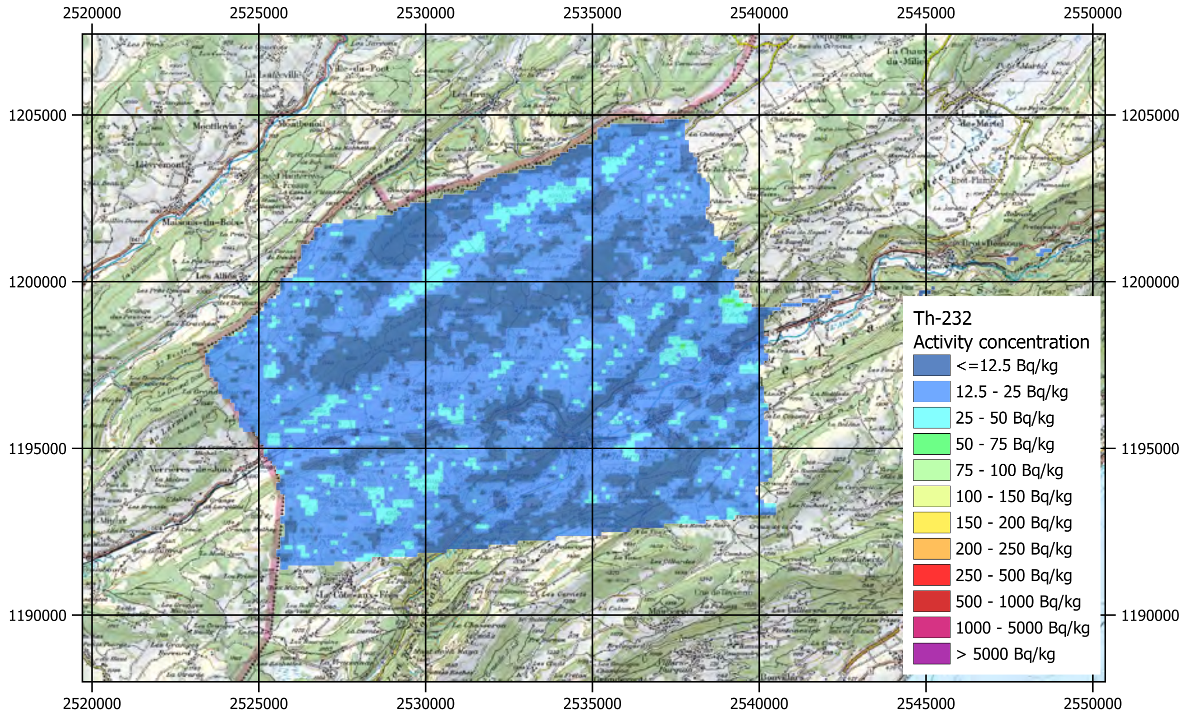

Figure 38: ^{232}Th activity concentration measured in the area of Fleurier. Geodata©Swisstopo.

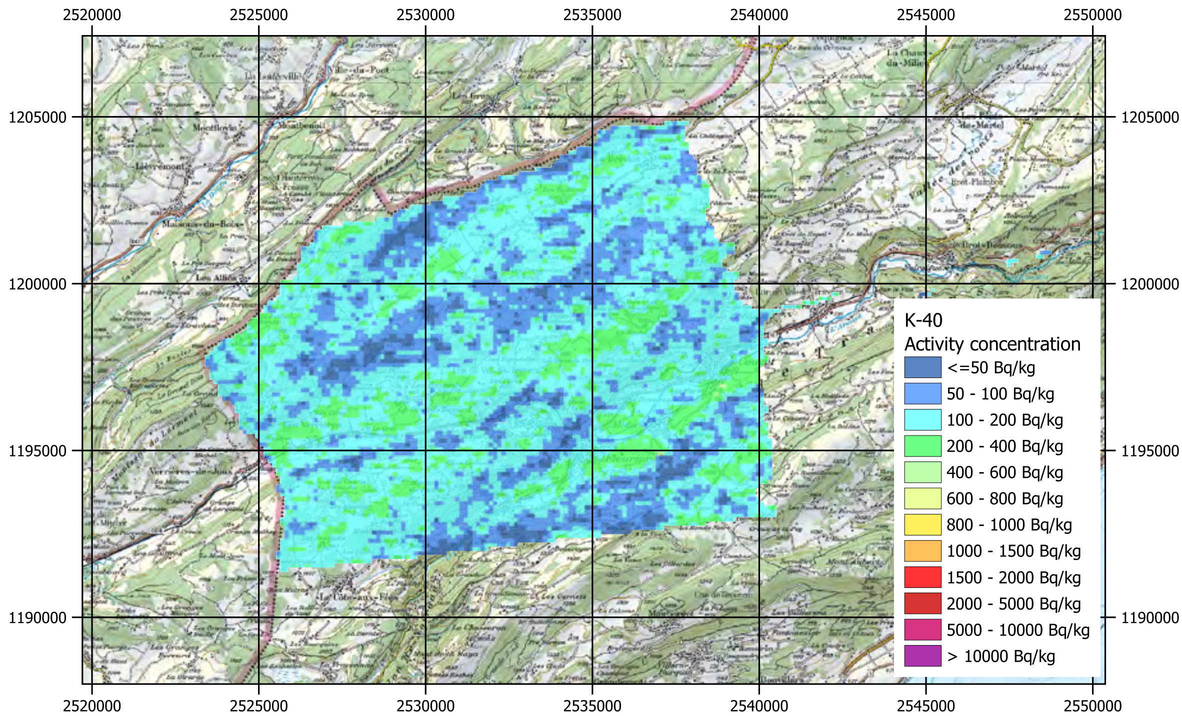

Figure 39: ^{40}K activity concentration measured in the area of Fleurier. Geodata©Swisstopo.

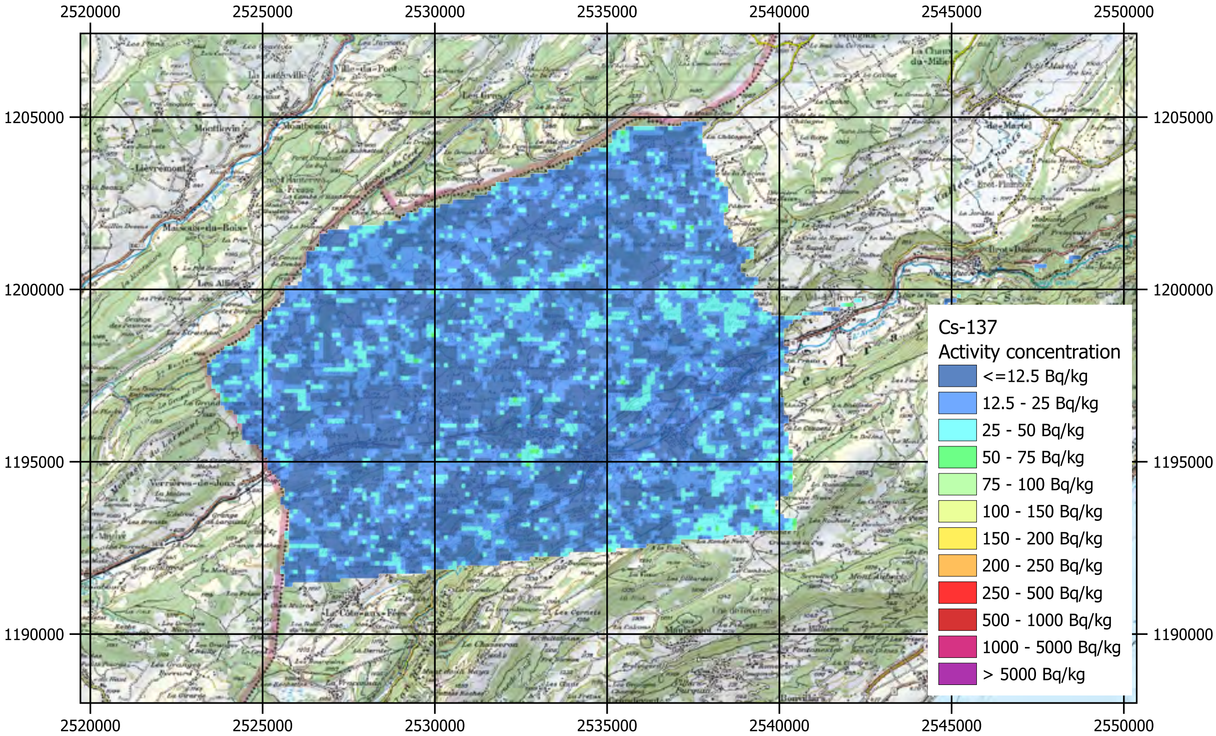

Figure 40: ^{137}Cs activity concentration measured in the area of Fleurier. Geodata©Swisstopo.

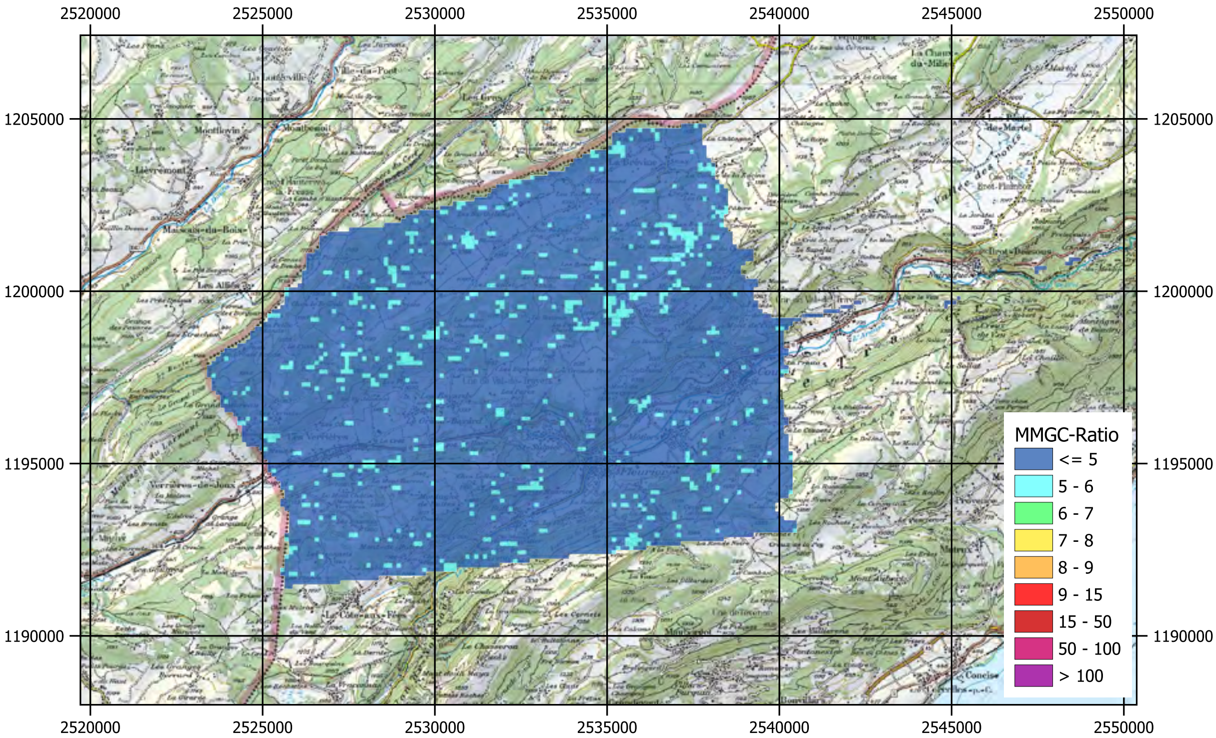

Figure 41: MMGC measured in the area of Fleurier. Geodata©Swisstopo.

3.1.6 Gibloux

The survey of the Gibloux area reports typical dose rates for western Switzerland, as illustrated in Figure 42. Lower values are observed over Lac de la Gruyère, due to water attenuating radiation emitted by terrestrial radionuclides in the lakebed. The ^{232}Th activity concentration map in Figure 43 shows no significant deviations from the expected concentrations in the region, with a slightly higher average concentration along the eastern shore of the lake. The MMGC-ratio map in Figure 44 does not indicate the presence of any man-made radionuclide.

The survey of the region was at different times, one of which coincided with a rainfall. The effect of the rain introduced a strong bending in the ^{238}U map of Figure 45 that exhibits significant variation, with the central area characterised by higher activity concentrations. This phenomenon is caused by rain depositing radon progeny onto the ground, which would otherwise remain in the air; in particular the deposition of ^{214}Bi, whose decay is used to quantify the presence of uranium in the soil.

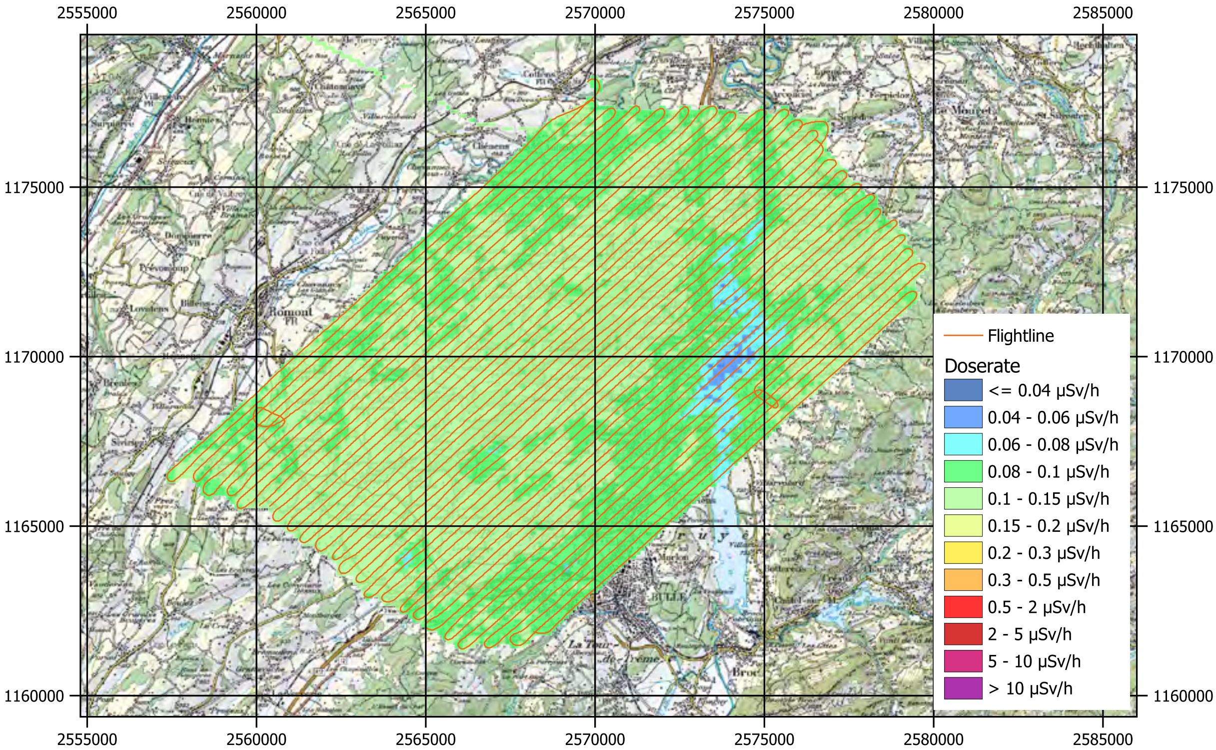

Figure 42: Dose rate measured in the area of Gibloux. Geodata©Swisstopo.

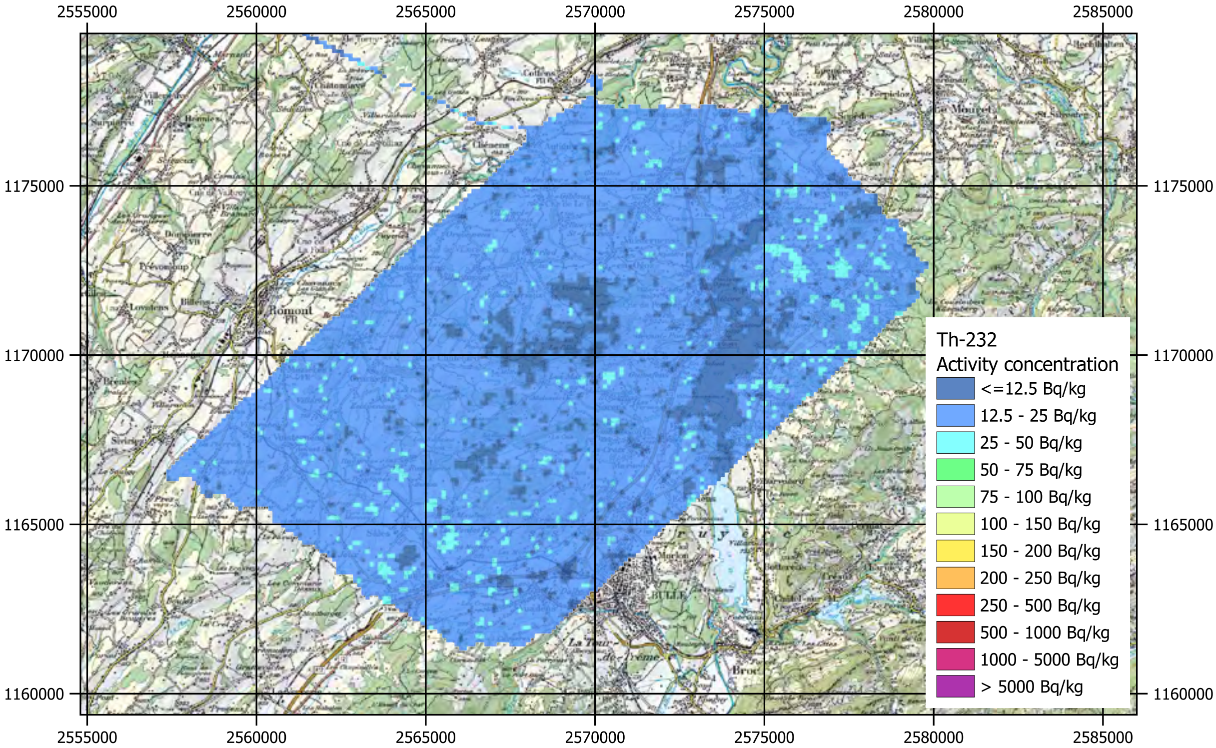

Figure 43: ^{232}Th activity concentration measured in the area of Gibloux. Geodata©Swisstopo.

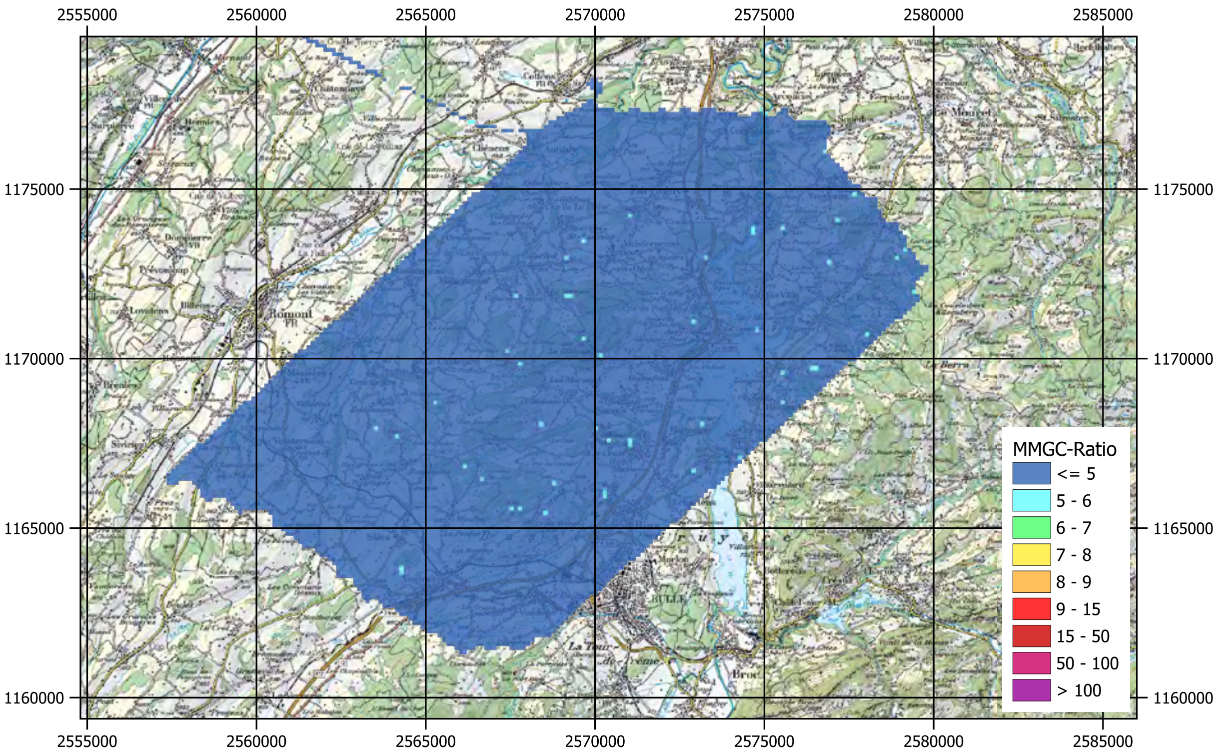

Figure 44: MMGC measured in the area of Gibloux. Geodata©Swisstopo.

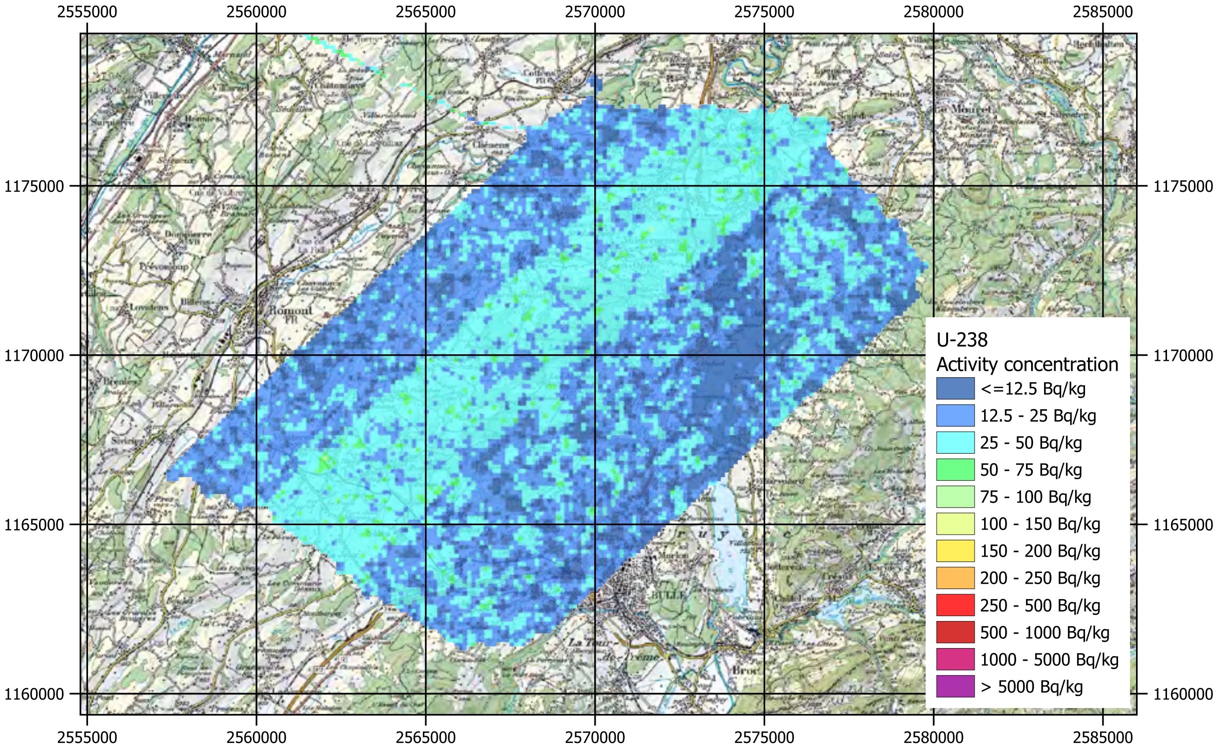

Figure 45: ^{238}U activity concentration measured in the area of Gibloux. Geodata©Swisstopo.

3.1.7 Sainte-Croix

The dose rate map in Figure 46, derived from measurements over the Sainte-Croix region, displays typical values consistent with those observed in neighbouring areas. The ^{232}Th activity concentration map in Figure 47 indicates levels below 50 Bq/kg, except for a small area in the north-western part of the surveyed region.

Traces of ^{137}Cs have been detected in the north-east and south of the surveyed area (Figure 49), which correlate well with the MMGC-ratio map shown in Figure 48. As for the adjacent region of Fleurier, the presence of the man made radionuclide is attributed to the Chernobyl accident. The amount of ^{137}Cs detected does not pose any radiological concern.

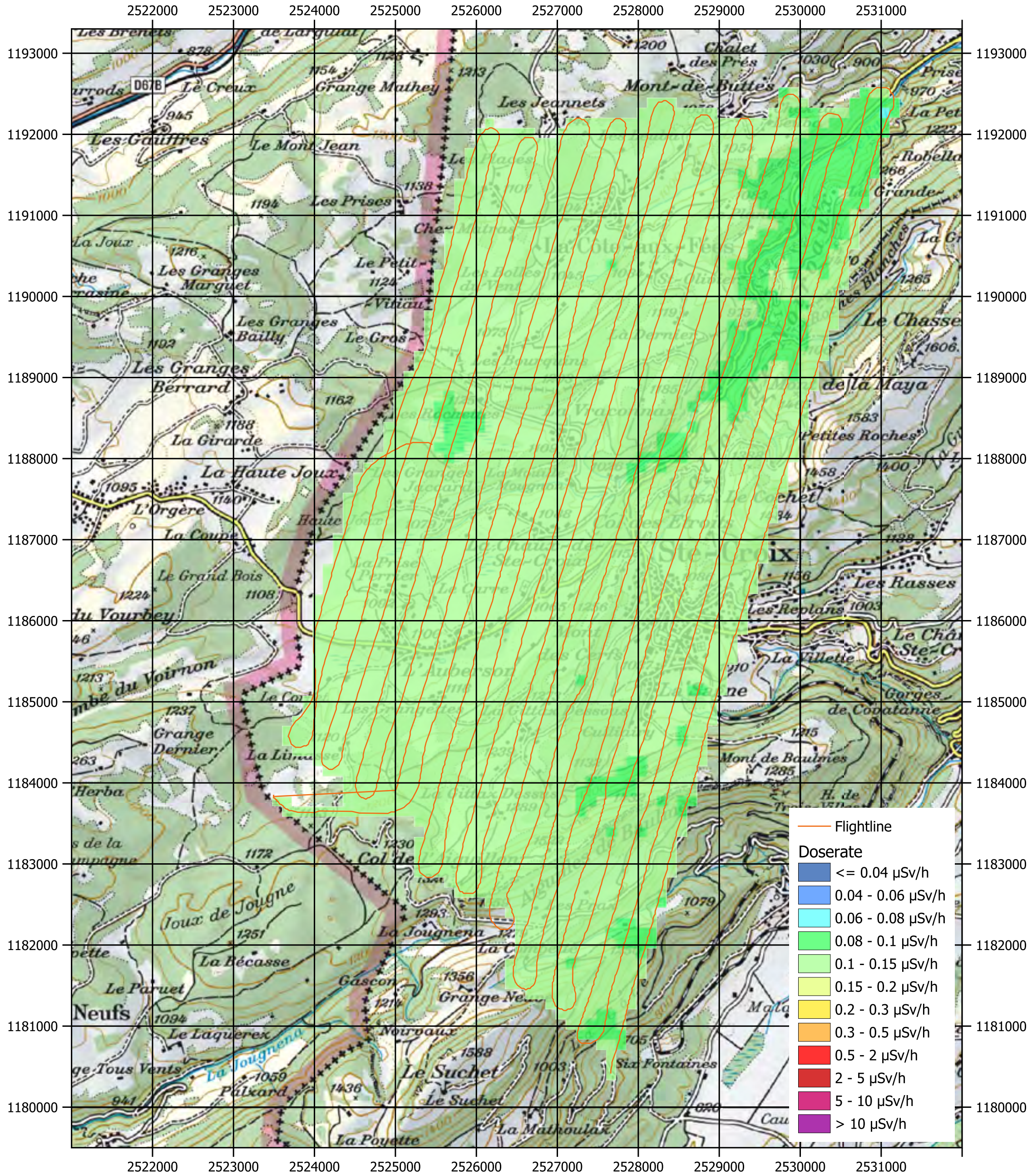

Figure 46: Dose rate measured in the area of Sainte-Croix. Geodata©Swisstopo.

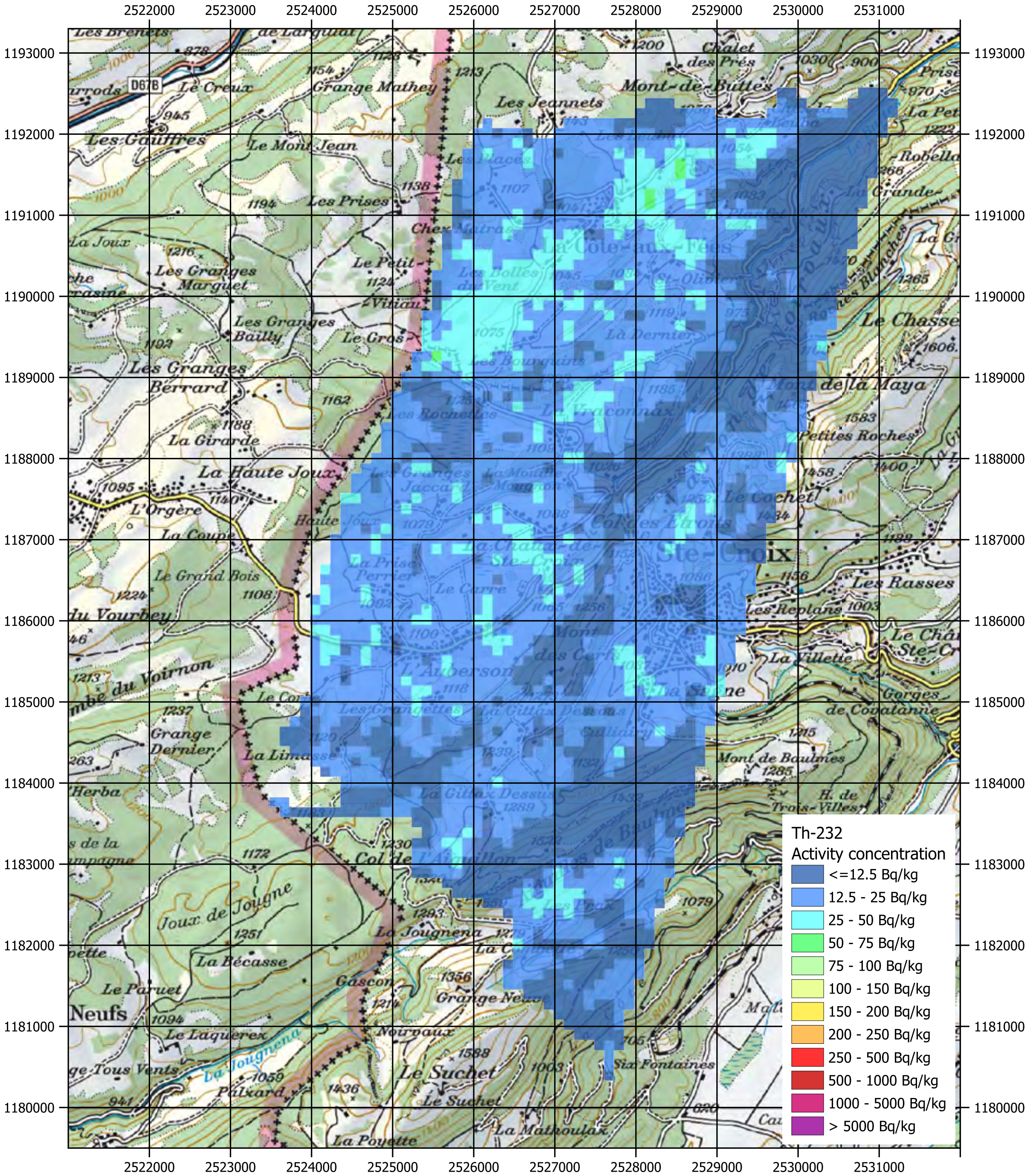

Figure 47: ^{232}Th activity concentration measured in the area of Sainte-Croix. Geodata©Swisstopo.

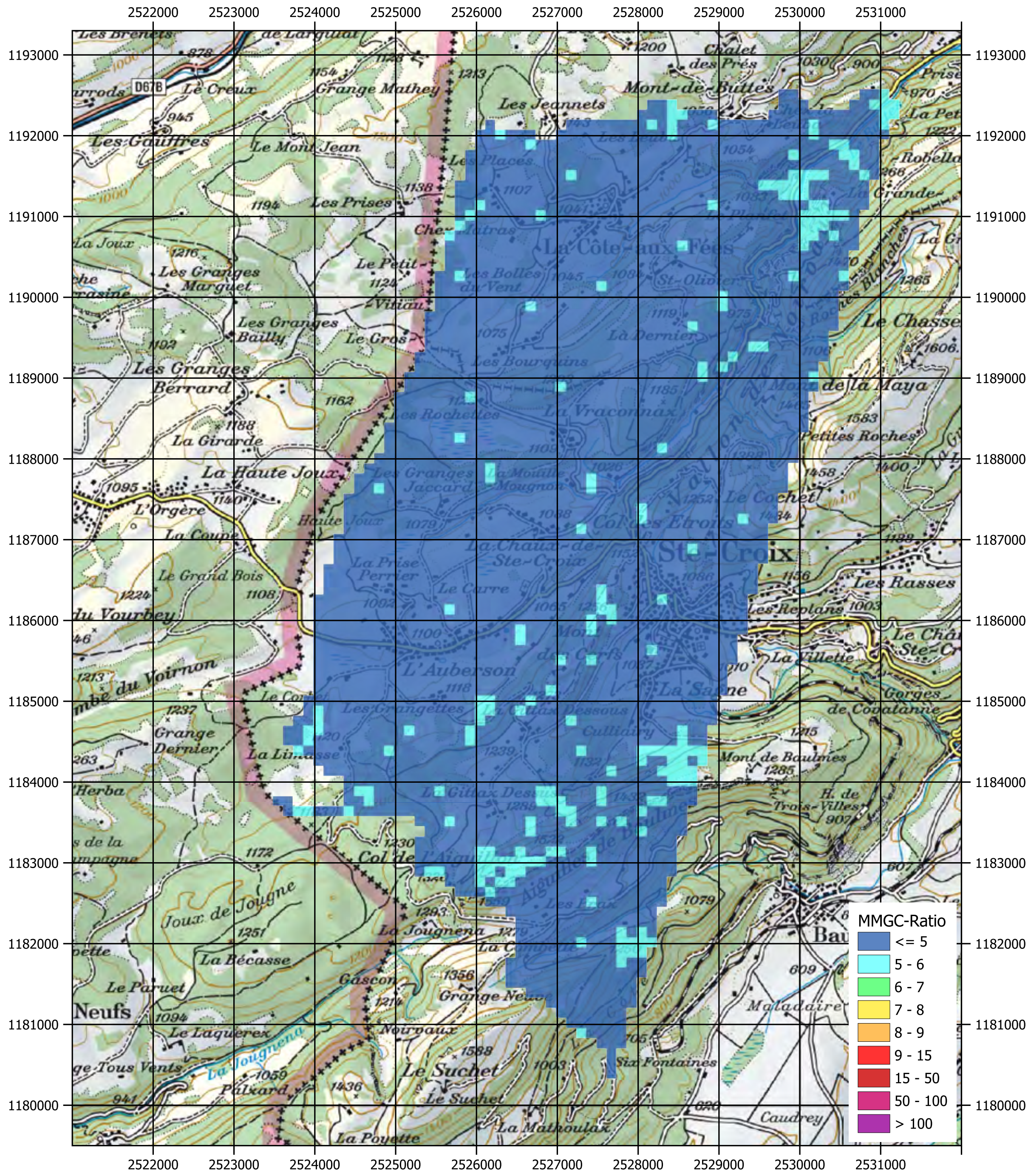

Figure 48: MMGC measured in the area of Sainte-Croix. Geodata©Swisstopo.

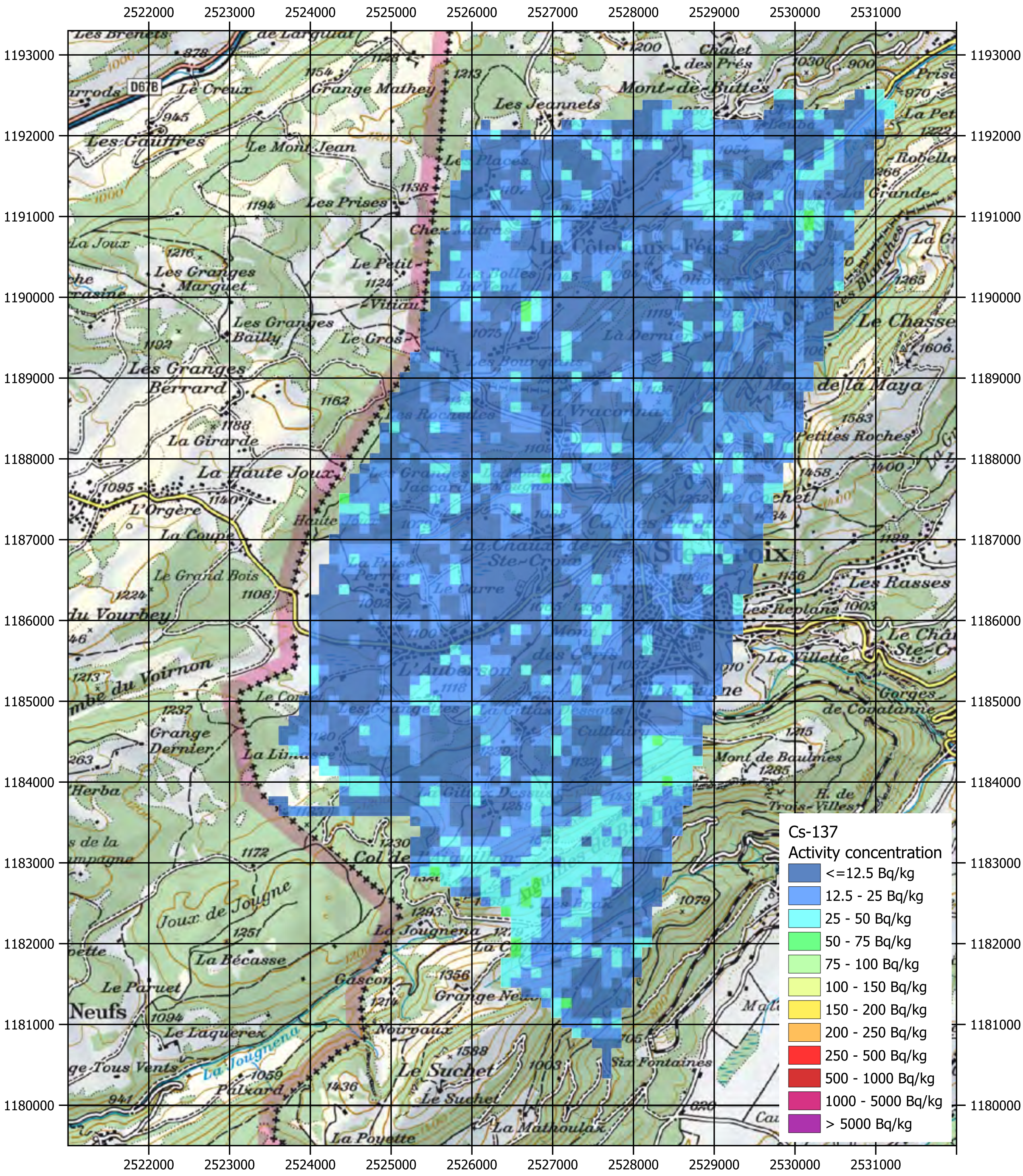

Figure 49: ^{137}Cs activity concentration measured in the area of Sainte-Croix. Geodata©Swisstopo.

3.2 International exercise AGC24 in the Czech Republic

3.2.1 Ground clearance

Figure 50 summarises the distribution of the ground clearances adopted for each task during the measuring flights of the AGC24 measurement campaign in the Czech Republic. Consecutive numbers indicate subsequent measurements during each task, as indicated in Table 5, with the only exception of VYS_1, which merges files "Heli 1_20240604 1341" and "Heli 1_20240604 1417", pertaining to the same measurement. The distributions feature relatively narrow peaks centred on prescribed ground clearances of 70 m, 90 m, 100 m and 140 m, demonstrating that the altitude above ground could be kept reasonably constant during the whole survey flights.

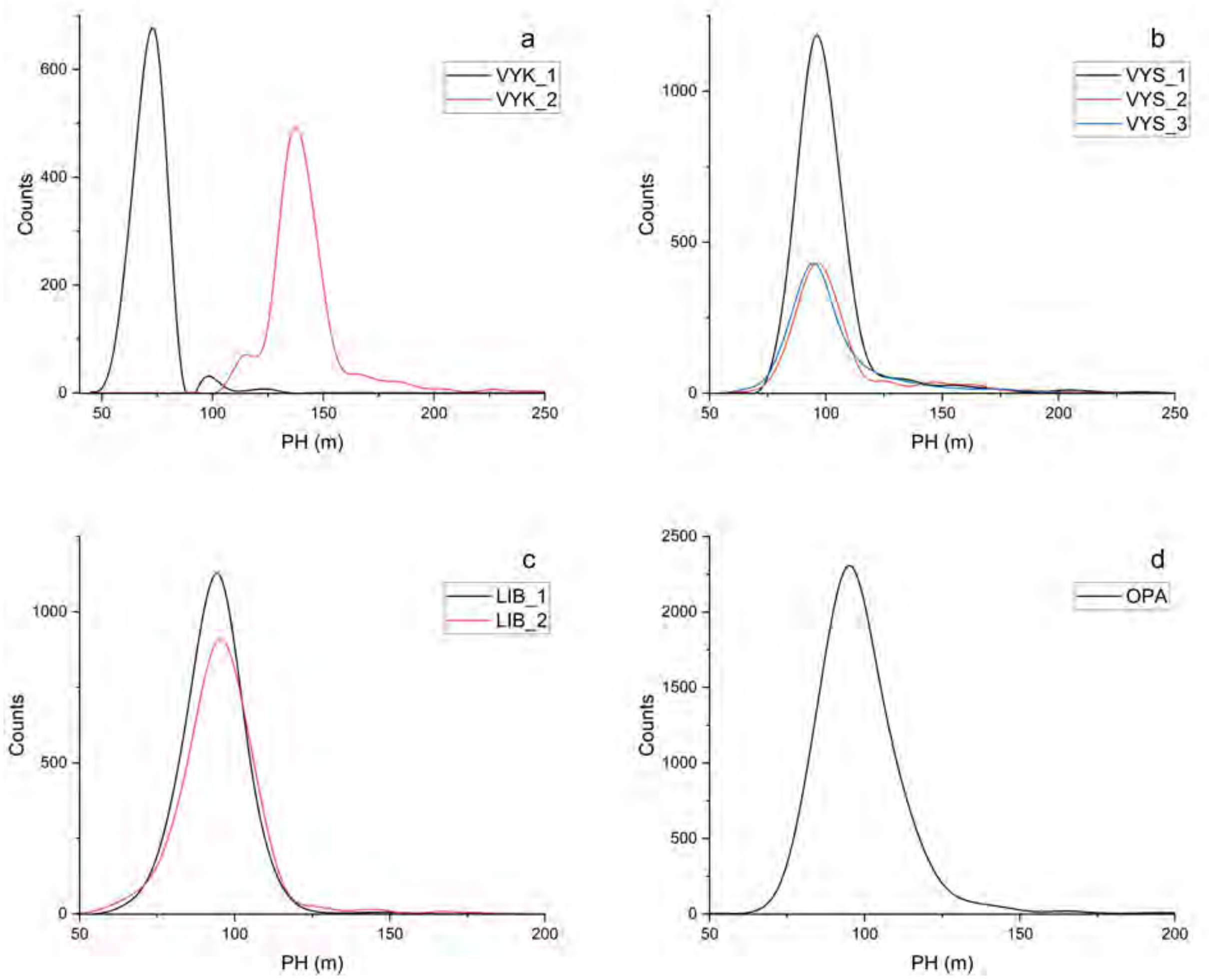

Figure 50: Flight altitude distribution grouped by task.

3.2.2 Task 1: VYK

Dose rate maps (Figure 51) obtained from flights at altitudes of 70 m and 140 m show uniform values of approximately 0.1 μSv/h across the measured area, with lower values observed in correspondence of sharp turns. These lower values are likely due to the helicopter's tilt during manoeuvres, which causes the detector to be partially shielded from the ground by the fuselage and an overall smaller detector response as the large unshielded cross-section is not facing the ground directly. A similar pattern is observed in the activity concentration maps of ^{232}Th and ^{238}U (Figures 52 and 53), which predominantly show concentrations ranging from 25 Bq kg^{-1} to 50 Bq kg^{-1} for ^{232}Th and a slightly wider range of 25 Bq kg^{-1} to 75 Bq kg^{-1} for ^{238}U. The activity concentration of ^{40}K (Figure 54) correlates well with ground vegetation. Lower concentrations are found in wooded areas, while slightly higher values are observed in open fields and along gravel roads.

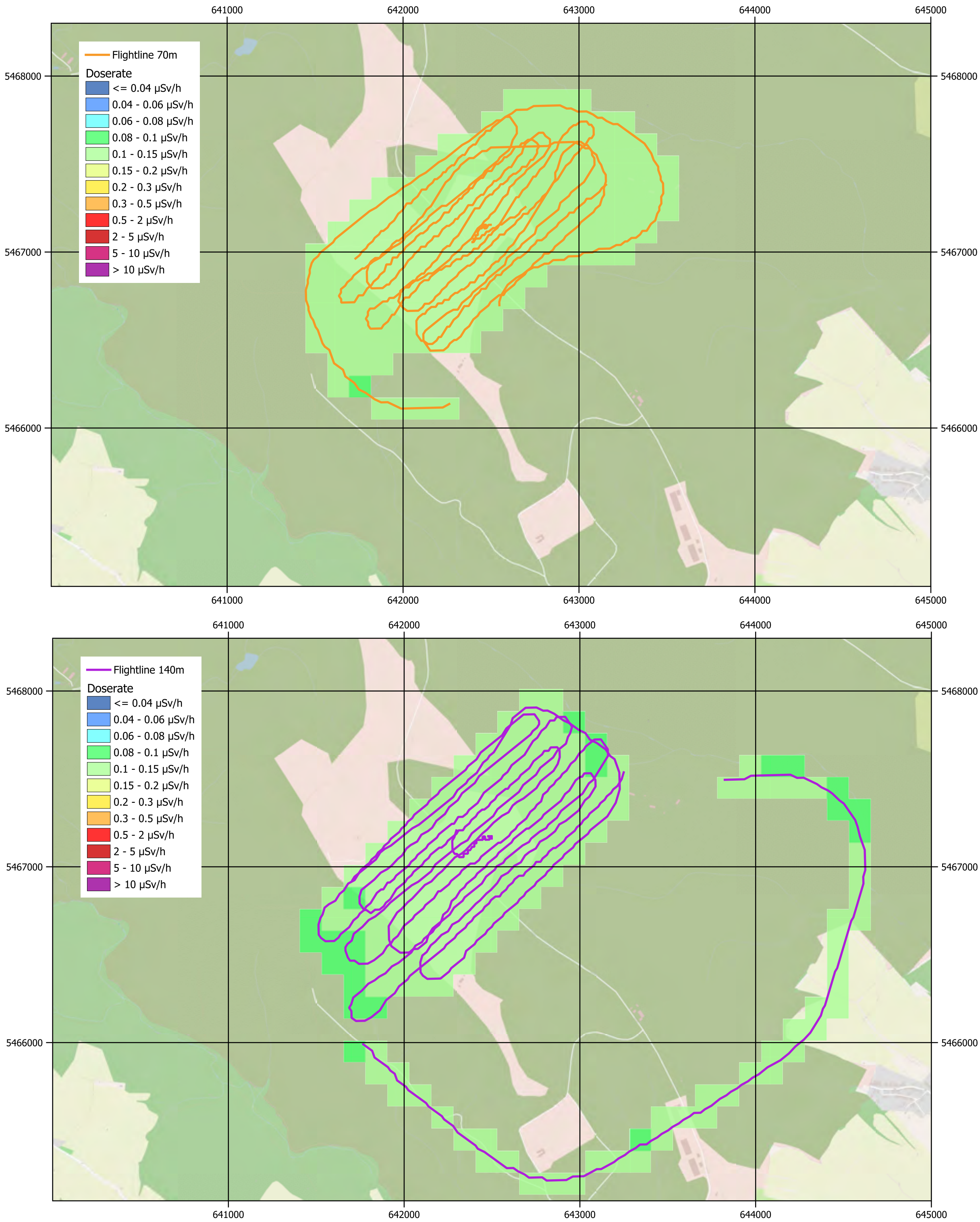

Figure 51: Dose rate measured at VYK with a flight clearance of 70m (top) and 140m (bottom). Geodata©OpenStreetMap.

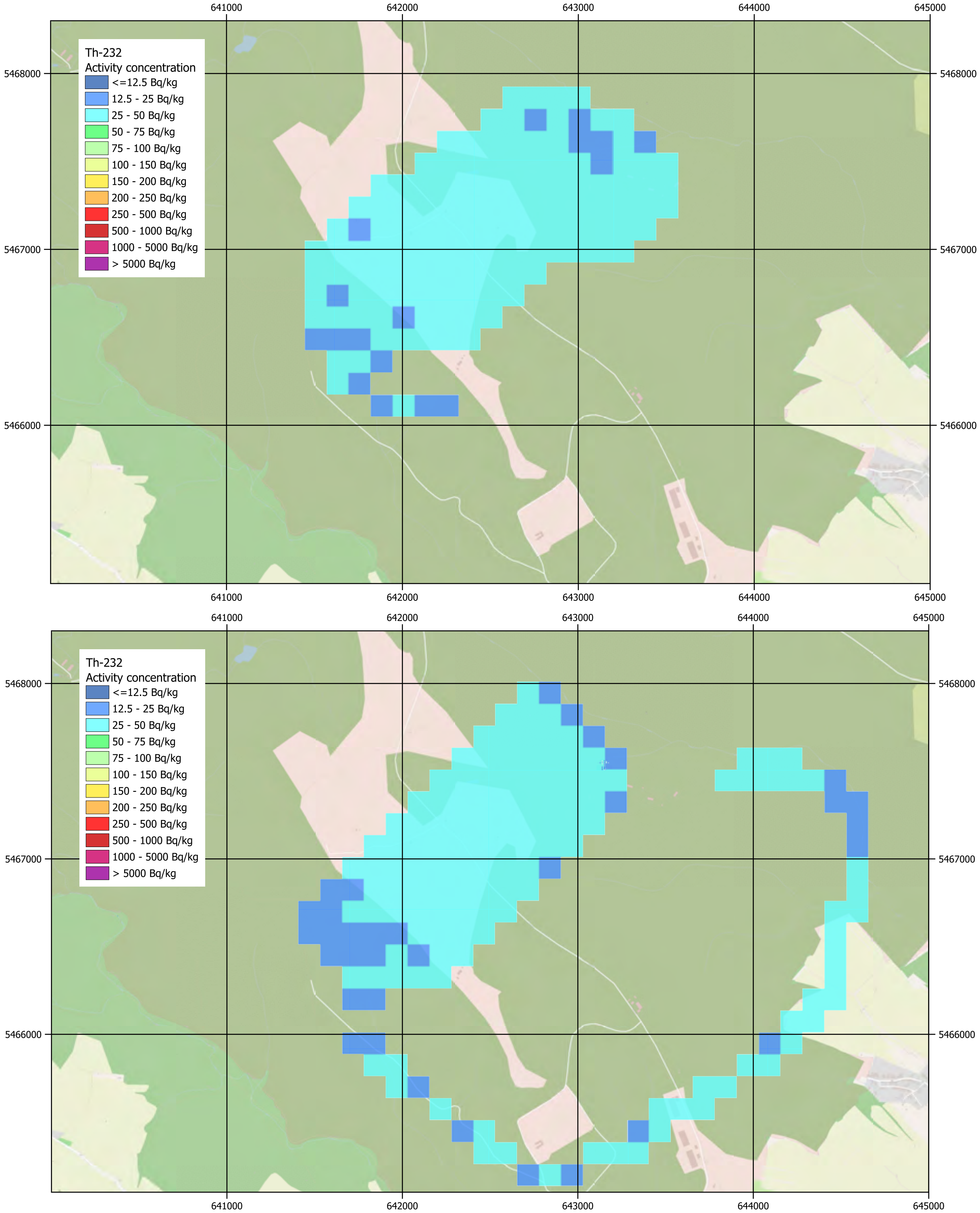

Figure 52: ^{232}Th activity concentration measured at VYK with a flight clearance of 70m (top) and 140m (bottom). Geodata©OpenStreetMap.

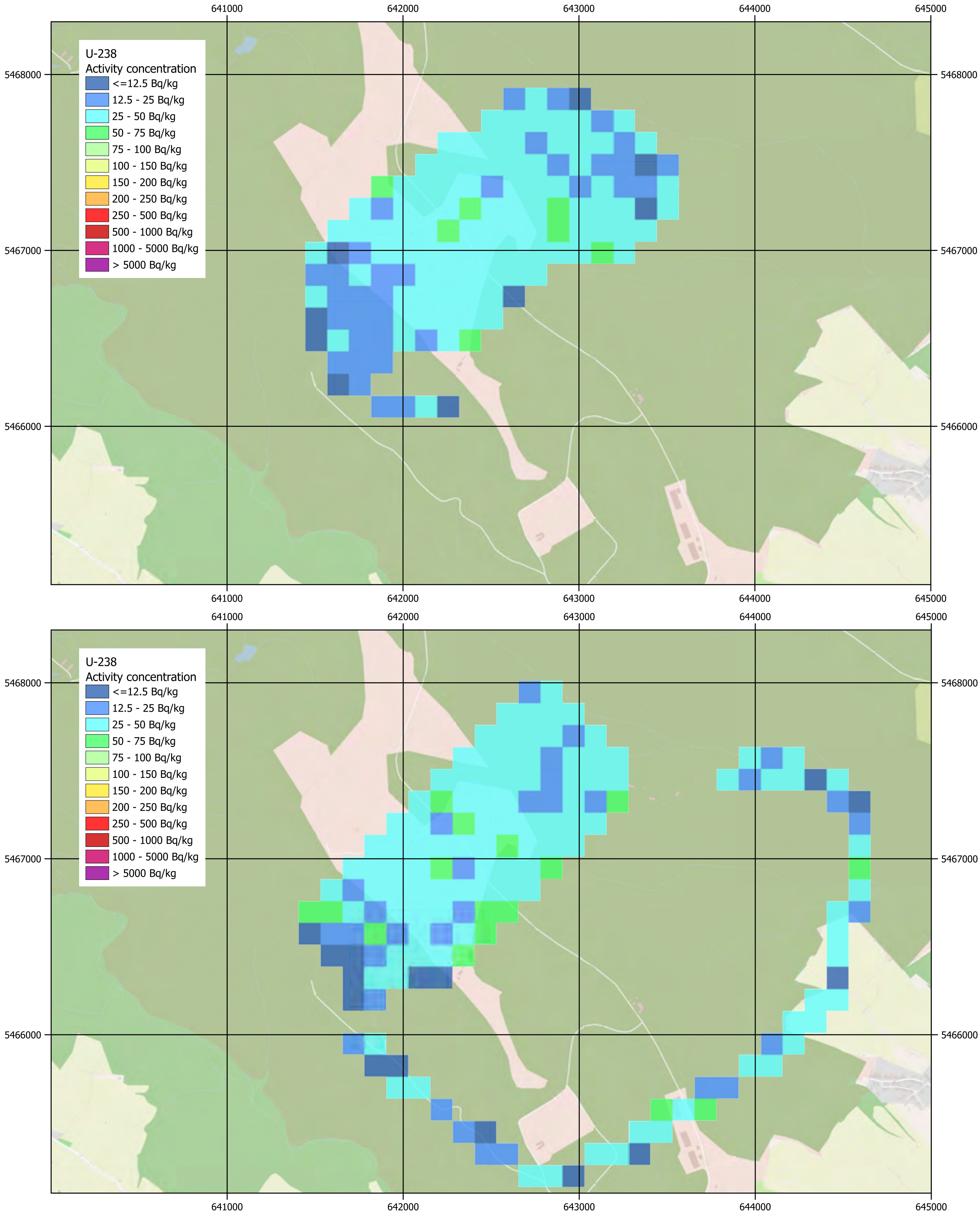

Figure 53: ^{238}U activity concentration measured at VYK with a flight clearance of 70m (top) and 140m (bottom). Geodata©OpenStreetMap.

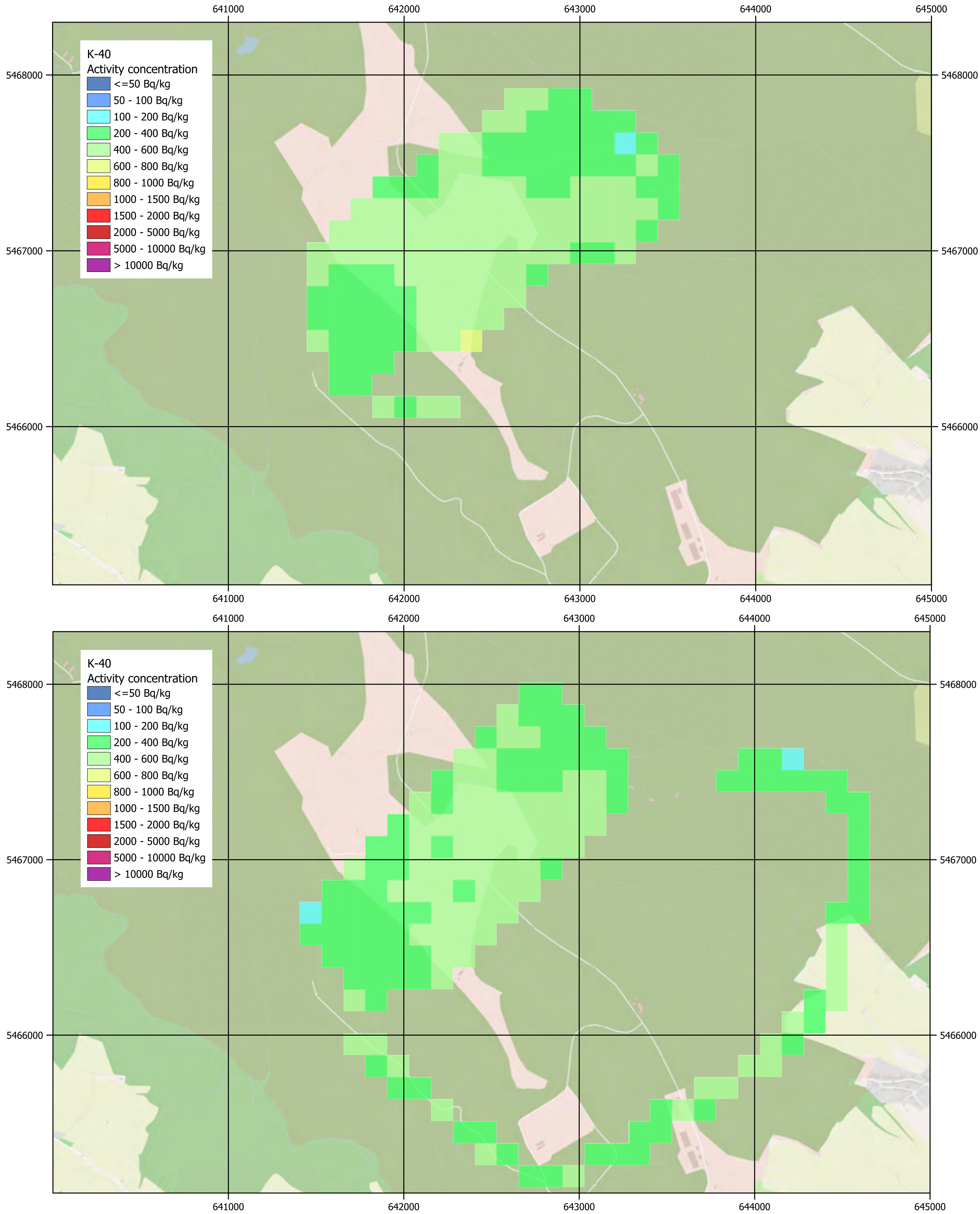

Figure 54: ^{40}K activity concentration measured at VYK with a flight clearance of 70m (top) and 140m (bottom). Geodata©OpenStreetMap.

Height comparison

The repeated measurements over the same area at different ground clearances provided an opportunity to test the evaluation algorithm and compare the estimated dose rates and activity concentrations. Figures 55 through 58 illustrate the percentage deviations obtained by comparing the estimates at altitudes of 70 m and 140 m over the surveyed area.

As shown in Figure 55, the dose rate estimations at two different ground clearances differ by less than 15%. The activity concentrations of ^{232}Th and ^{40}K, depicted in Figures 56 and 57, generally agree within 25% across most of the area. Larger discrepancies of up to 50% are observed at the edges of the surveyed region, likely arising from differences in flight trajectories and variations in the detector's field of view. Estimation of ^{238}U low activity concentration, as displayed in Figure 58, is generally affected by larger uncertainties arising from the influence of radon in air.

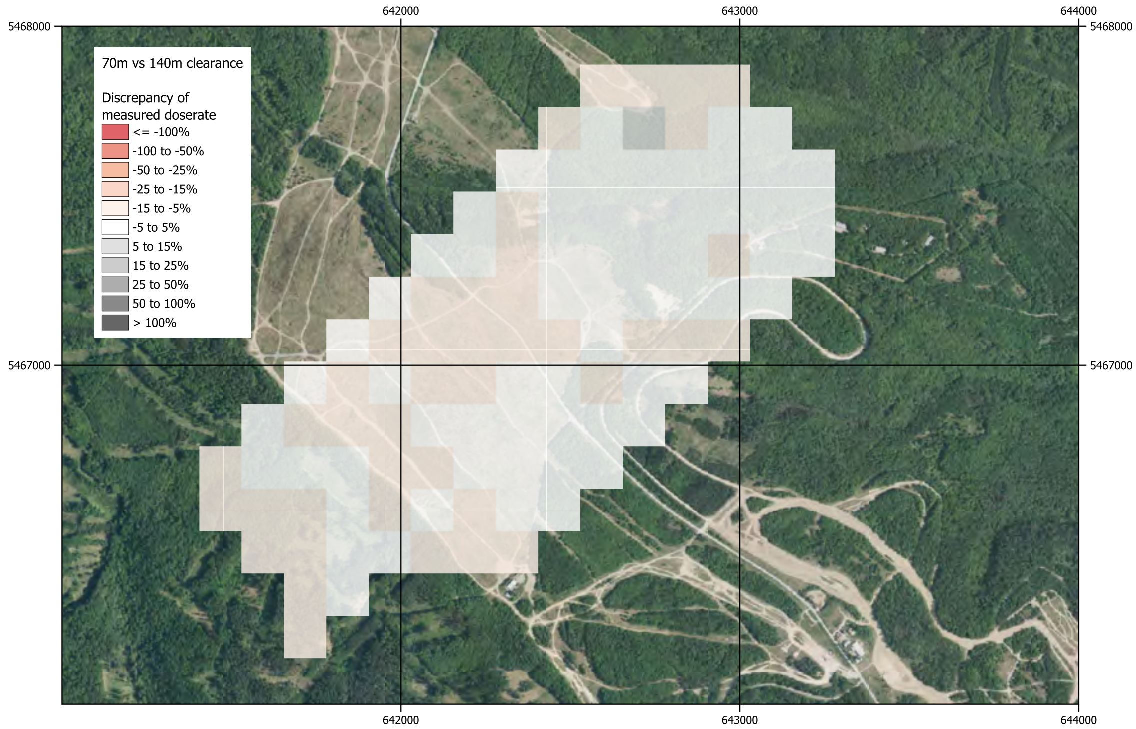

Figure 55: Discrepancy in dose rate measurements during flights at ground clearances of 70m and 140m at VYK. Orthophoto©Czech Office for Surveying, Mapping and Cadastre.

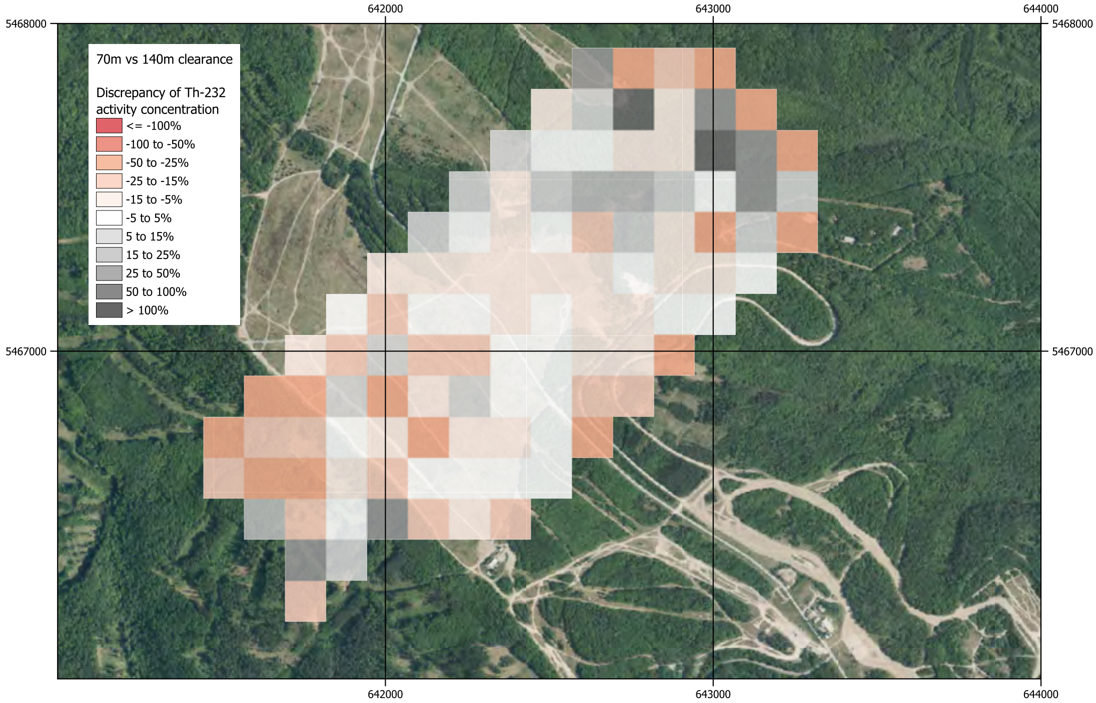

Figure 56: Discrepancy in ^{232}Th activity concentration measurements during flights at ground clearances of 70m and 140m at VYK. Orthophoto©Czech Office for Surveying, Mapping and Cadastre.

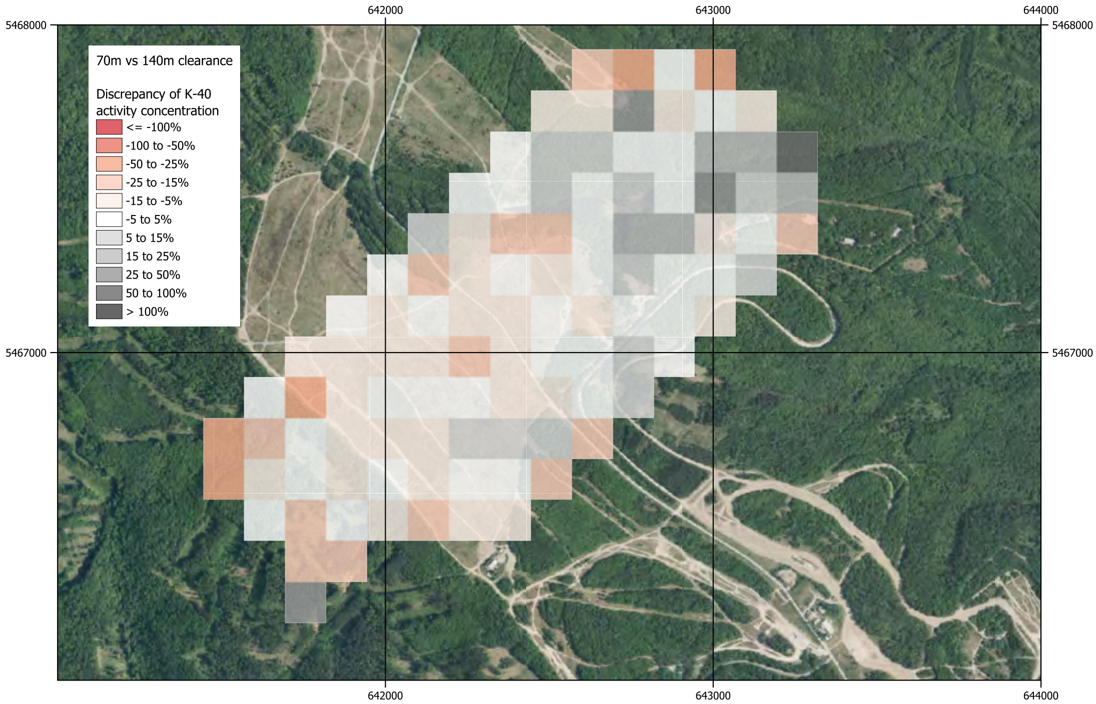

Figure 57: Discrepancy in ^{40}K activity concentration measurements during flights at ground clearances of 70m and 140m at VYK. Orthophoto©Czech Office for Surveying, Mapping and Cadastre.

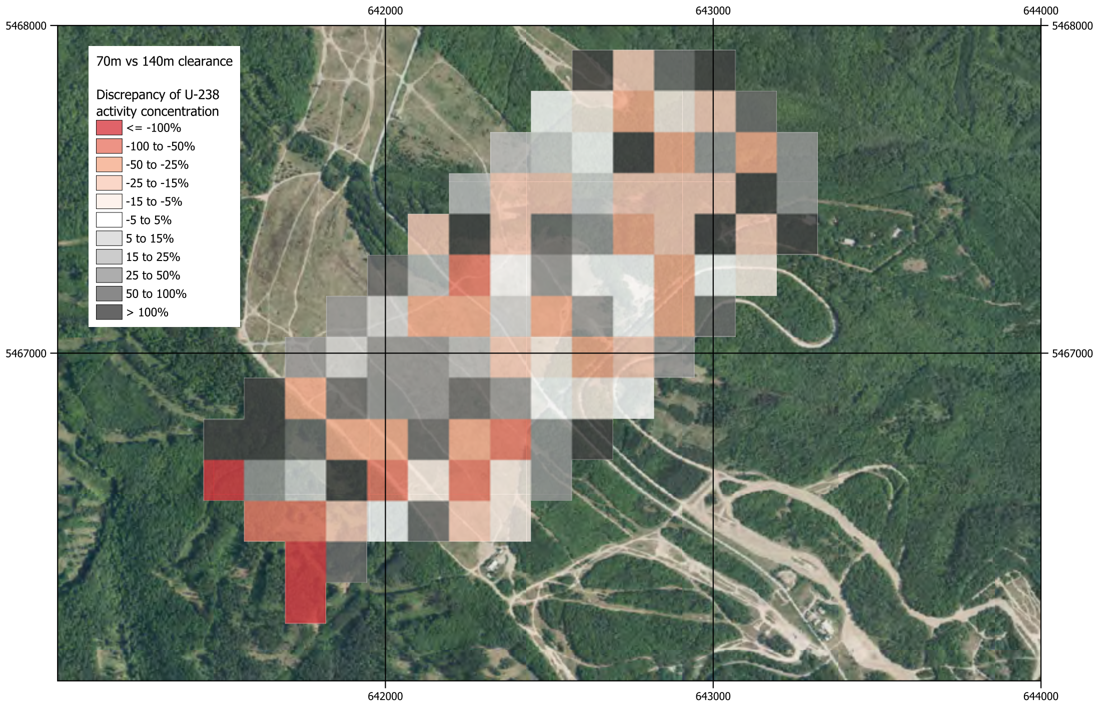

Figure 58: Discrepancy in ^{238}U activity concentration measurements during flights at ground clearances of 70m and 140m at VYK. Orthophoto©Czech Office for Surveying, Mapping and Cadastre.

Software comparison

Figures 59 to 62 illustrate the comparison of the dose rate and activity concentration estimations obtained with the AGS_CH and the Mirion software of the flight at 140 m clearance.

As shown in Figures 59 and 60, the dose rate and the ^{232}Th activity concentration agree within 5% across most of the area. The largest discrepancies, up to 15%, occur over wooded areas. This can be attributed to differences in how ground clearance is estimated. Unlike the Mirion software, which relies on radar signal to measure the distance from the ground, AGS_CH uses a corrected ground clearance derived from the digital elevation model and GPS altitude. Over dense forests, the layer of vegetation can cause discrepancies of a few tens of meters in the ground clearance estimation.

Discrepancies in the estimations of ^{40}K and ^{238}U activity concentrations are higher, as observed in Figures 57 and 58. The reason for the larger discrepancies could arise from the different width of the spectral windows defined in the two softwares: in fact, the Mirion software, in comparison to AGS_CH, has a larger number of windows that allow the activity estimation of more radionuclides. However, these windows are generally narrower in the Mirion software, implying larger statistical uncertainties in the counts and hence a larger dispersion of the activity estimations.

Figure 59: Discrepancy in dose rate estimates: AGS_CH vs. Mirion Software at 140m flight clearance VYK. Orthophoto©Czech Office for Surveying, Mapping and Cadastre.

Figure 60: Discrepancy in ^{232}Th activity concentration estimates: AGS_CH vs. Mirion Software at 140m flight clearance VYK. Orthophoto©Czech Office for Surveying, Mapping and Cadastre.

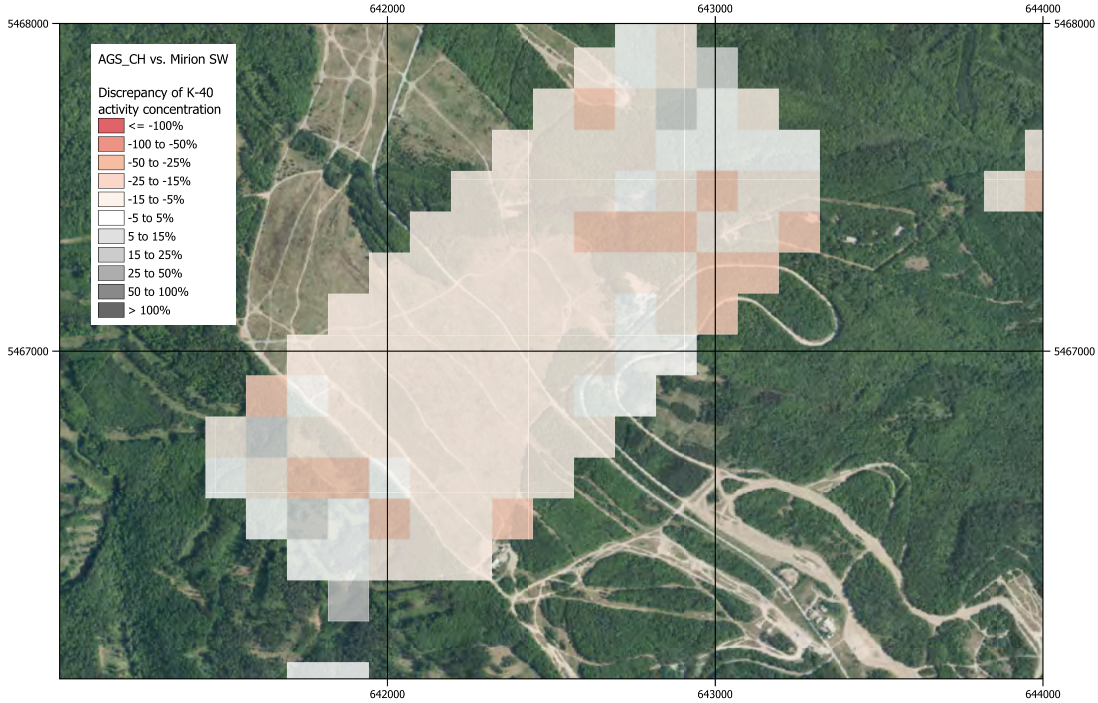

Figure 61: Discrepancy in ^{40}K activity concentration estimates: AGS_CH vs. Mirion Software at 140m flight clearance VYK. Orthophoto©Czech Office for Surveying, Mapping and Cadastre.

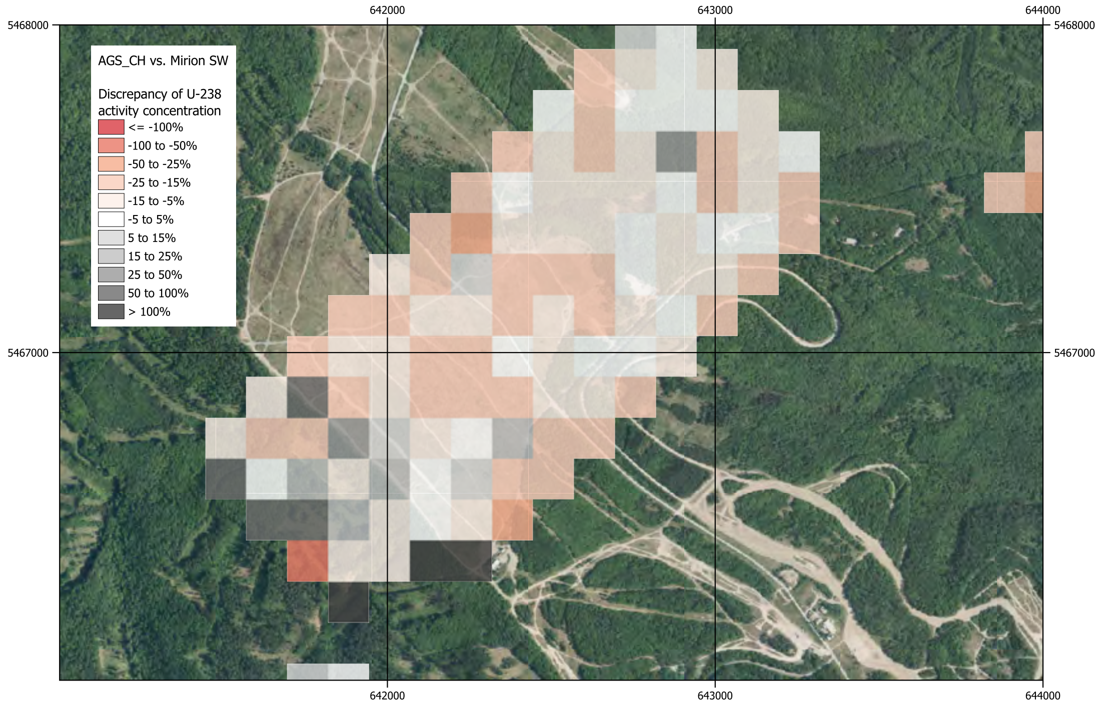

Figure 62: Discrepancy in ^{238}U activity concentration estimates: AGS_CH vs. Mirion Software at 140m flight clearance VYK. Orthophoto©Czech Office for Surveying, Mapping and Cadastre.

3.2.3 Task 2: VYS

The ambient dose equivalent rate calculated from the measurements in the Vysočina region is shown in the map in Figure 63. Elevated values, reaching up to 0.8 μSv/h, have been detected in the northernmost area, designated as high priority. This area contains the Rožná uranium mine, which was closed in 2017. Figure 64 provides a closer view of the dose rate map on the decommissioned uranium mine site. Increased dose rates were recorded in the vicinity of the main mine shaft "R1", in the settling basins, and around buildings used for the chemical processing of uranium ore. The high priority region located in the south, as well as the rest of the area (considered low priority), is characterised by typical background dose rates. Thanks to the initial estimation of dose rates and activity concentrations performed "online" during flights, the team decided to conduct two additional measurements in the northern area to enhance the collected data.

The map of ^{238}U activity shown in Figure 65 and Figure 66 illustrates concentrations up to 2 kBq kg^{-1} in the mining area, distributed in the same locations mentioned in relation to the dose rate. The spectrum acquired over the area is indicated in Figure 70 by a red line and show peaks in correspondence of ^{238}U daughters ^{214}Pb and ^{214}Bi. Areas with activity concentrations above normal background are also found near the main mining site.

The activity concentration map of ^{232}Th in Figure 68 shows typical background values (< 60 Bq kg^{-1}). In the results for the activity concentration of ^{40}K measured over the area (Figure 67), the highest values are observed in the region surrounding the mine. In the rest of the measured area, aside from low values over water surfaces, typical background concentration levels are present.

In the ^{137}Cs activity concentration map shown in Figure 69, an area of elevated ^{137}Cs concentration is visible near the river in the southern high-priority region, likely originating from Chernobyl fallout. The spectrum corresponding to this area, represented by the red line in Figure 70, features a distinct ^{137}Cs peak.

The elevated values observed near the uranium mine are artefacts caused by the very high and localised concentration of ^{238}U. Although the evaluation using the window method in AGS_CH applies a correction based on stripping factors, such high and localised ^{238}U concentrations (and, consequently, those of its daughter isotope ^{214}Bi, which emits at 609 keV) interfere with the ^{137}Cs energy window. This interference arises because the determination of stripping factors, as described in Section 2.1.1, assumes a homogeneous distribution of a given radionuclide over a large area. However, steep concentration gradients and highly localised contamination deviate from this assumption, reducing the effectiveness of the correction based on the estimated stripping factors.

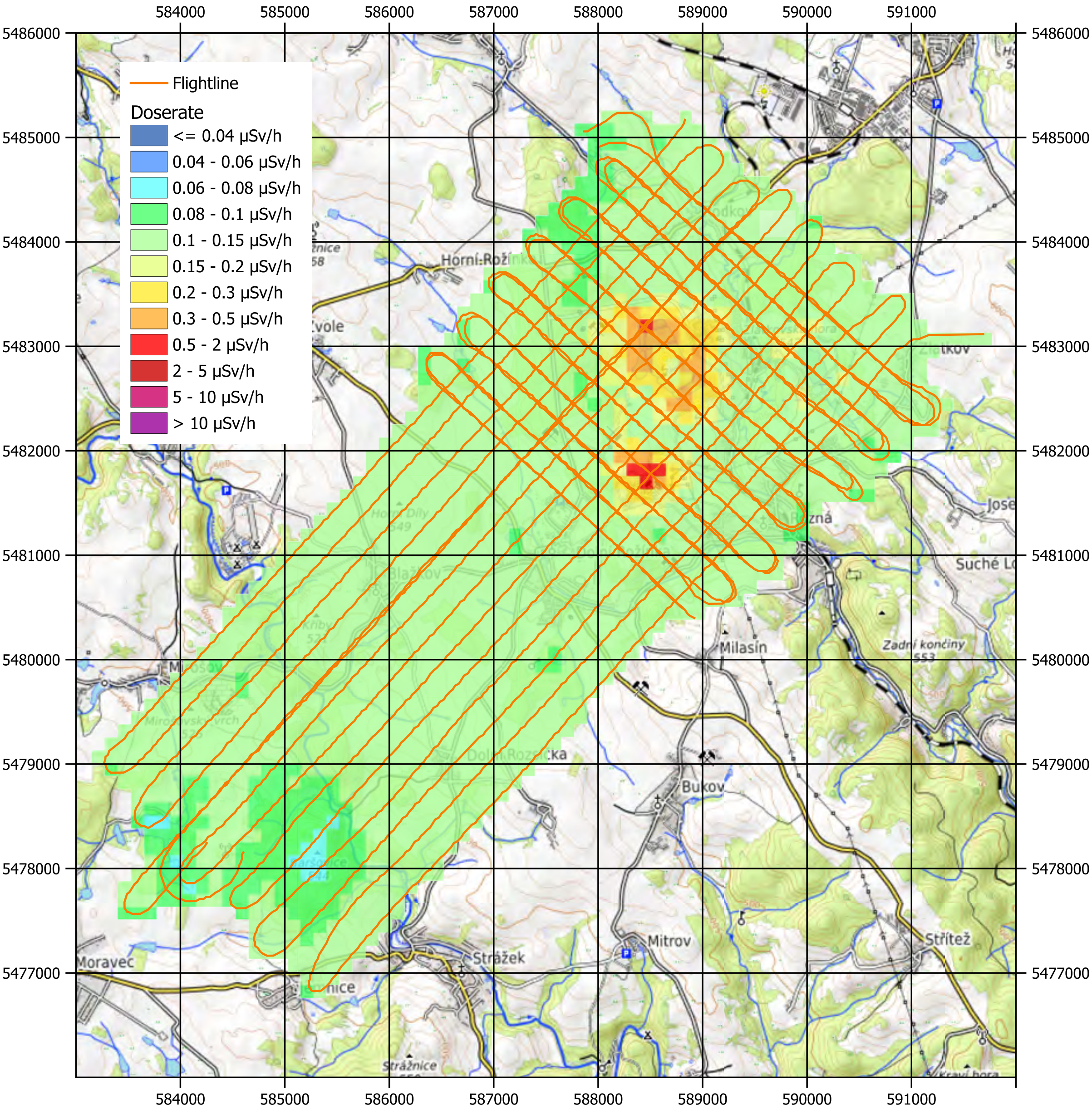

Figure 63: Dose rate measured at VYS. Geodata©OpenTopoMap.

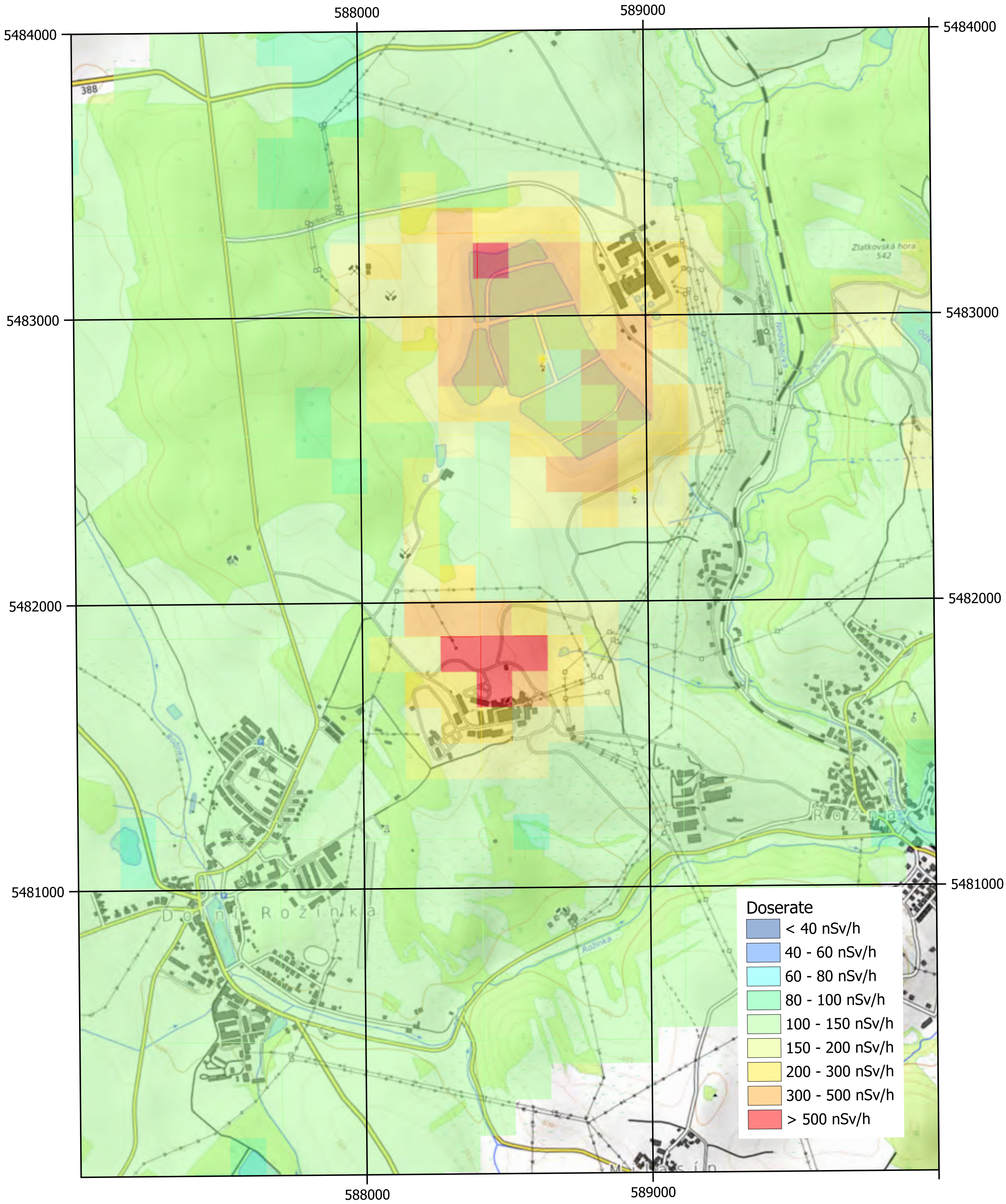

Figure 64: Dose rate measured at VYS, in the area of the uranium mine. Geodata©OpenTopoMap.

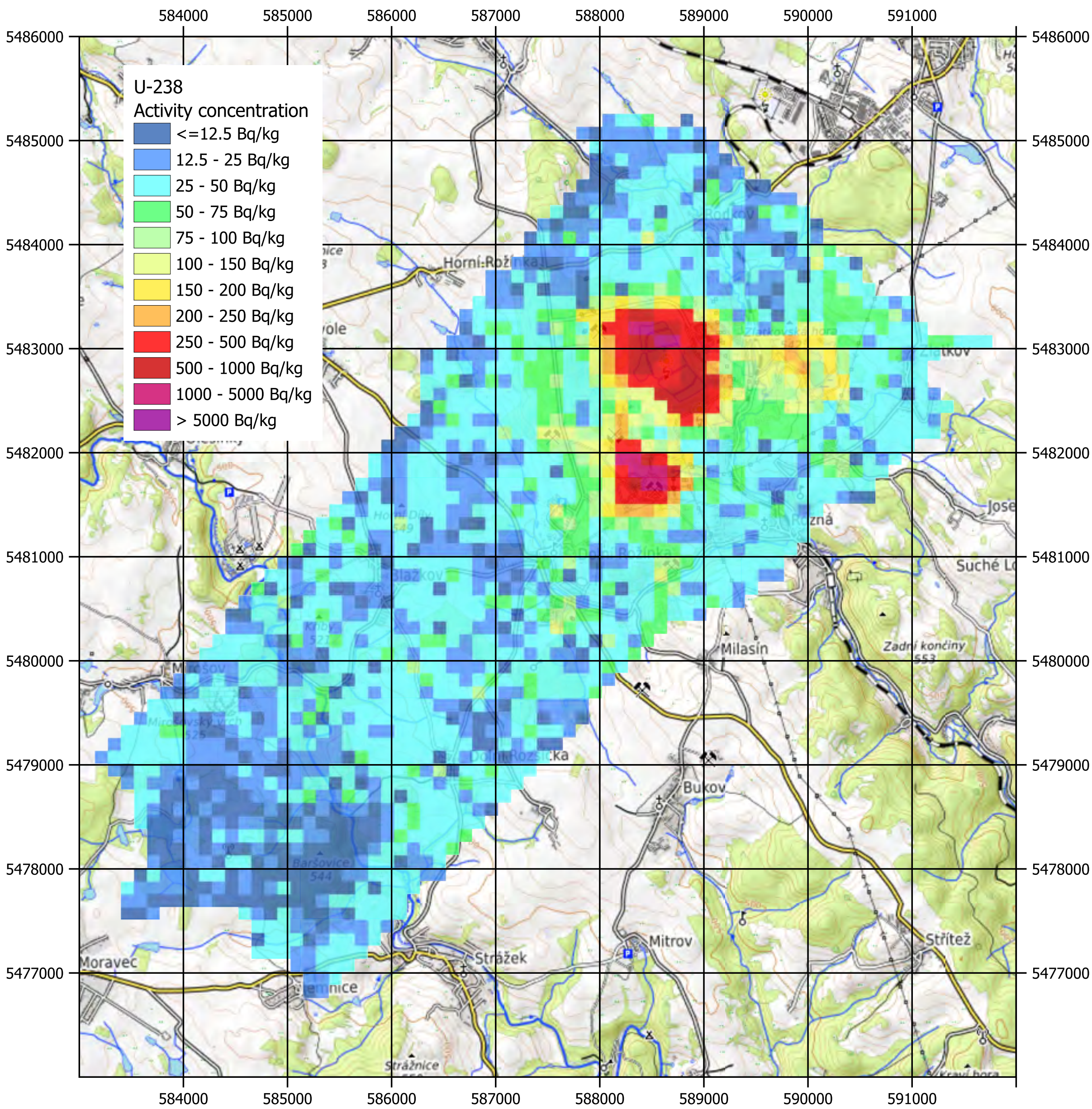

Figure 65: ^{238}U activity concentration measured at VYS. Geodata©OpenTopoMap.

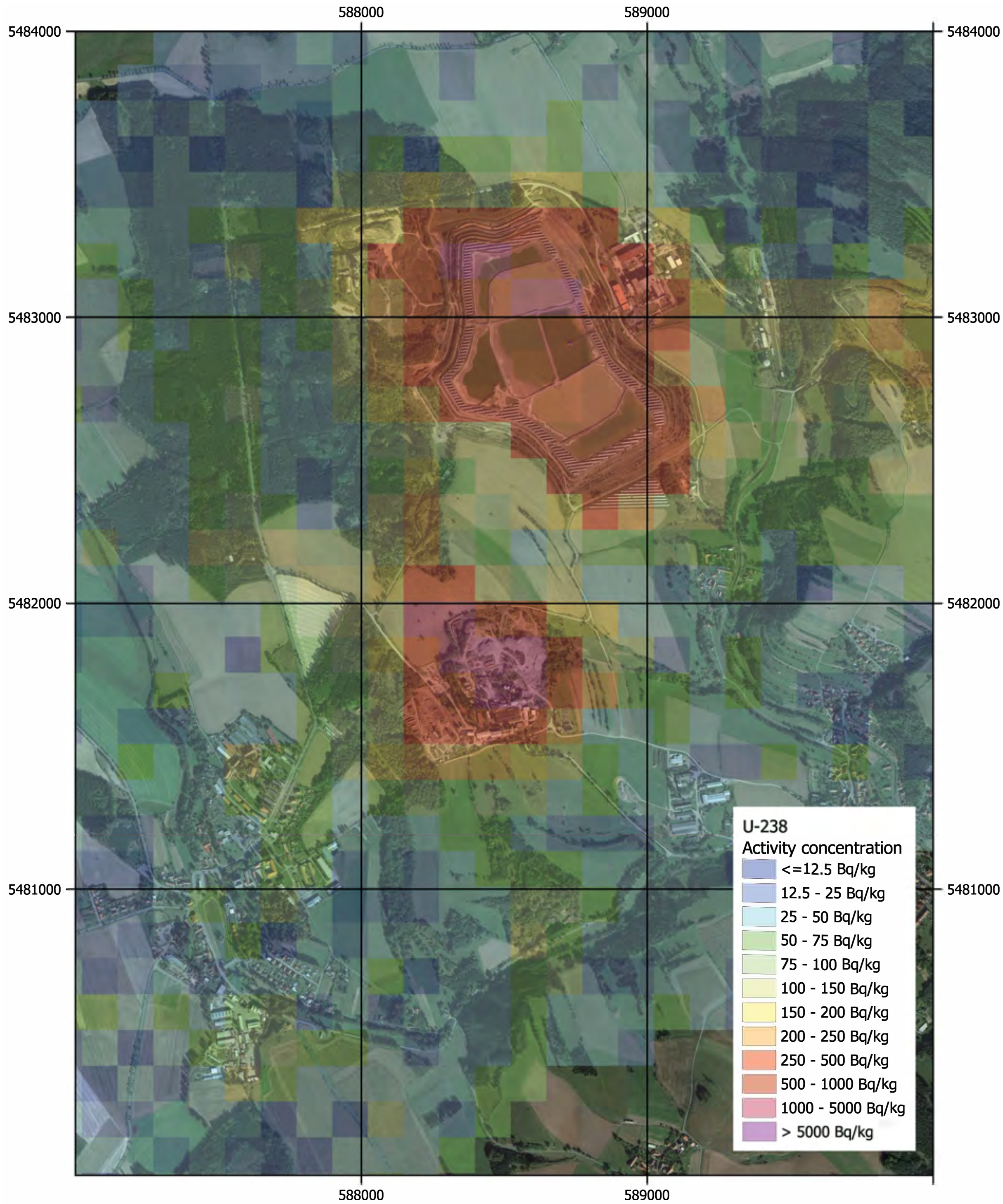

Figure 66: ^{238}U activity concentration measured at VYS, in the area of the uranium mine. Orthophoto©Czech Office for Surveying, Mapping and Cadastre.

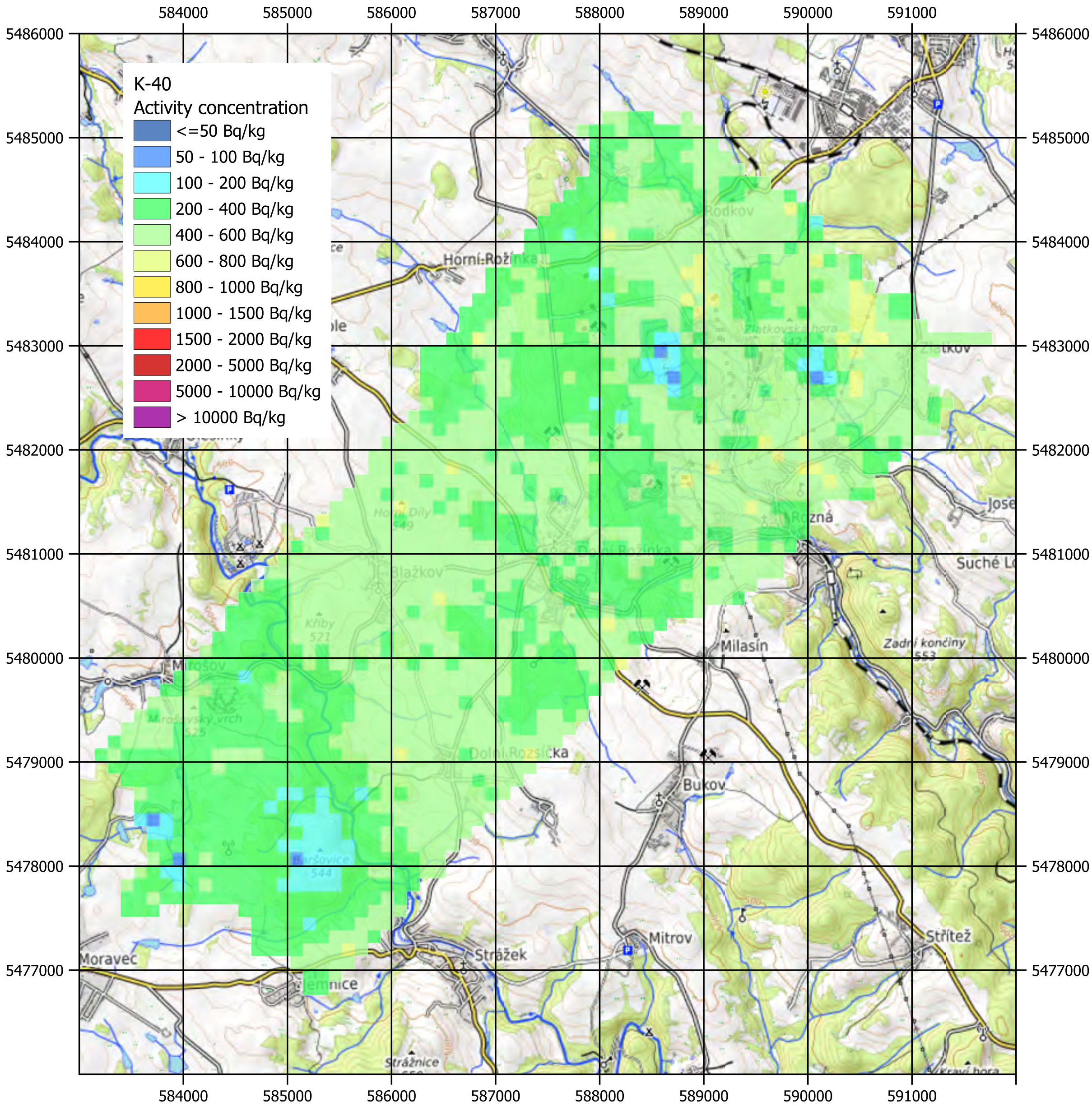

Figure 67: ^{40}K activity concentration measured at VYS. Geodata©OpenTopoMap.

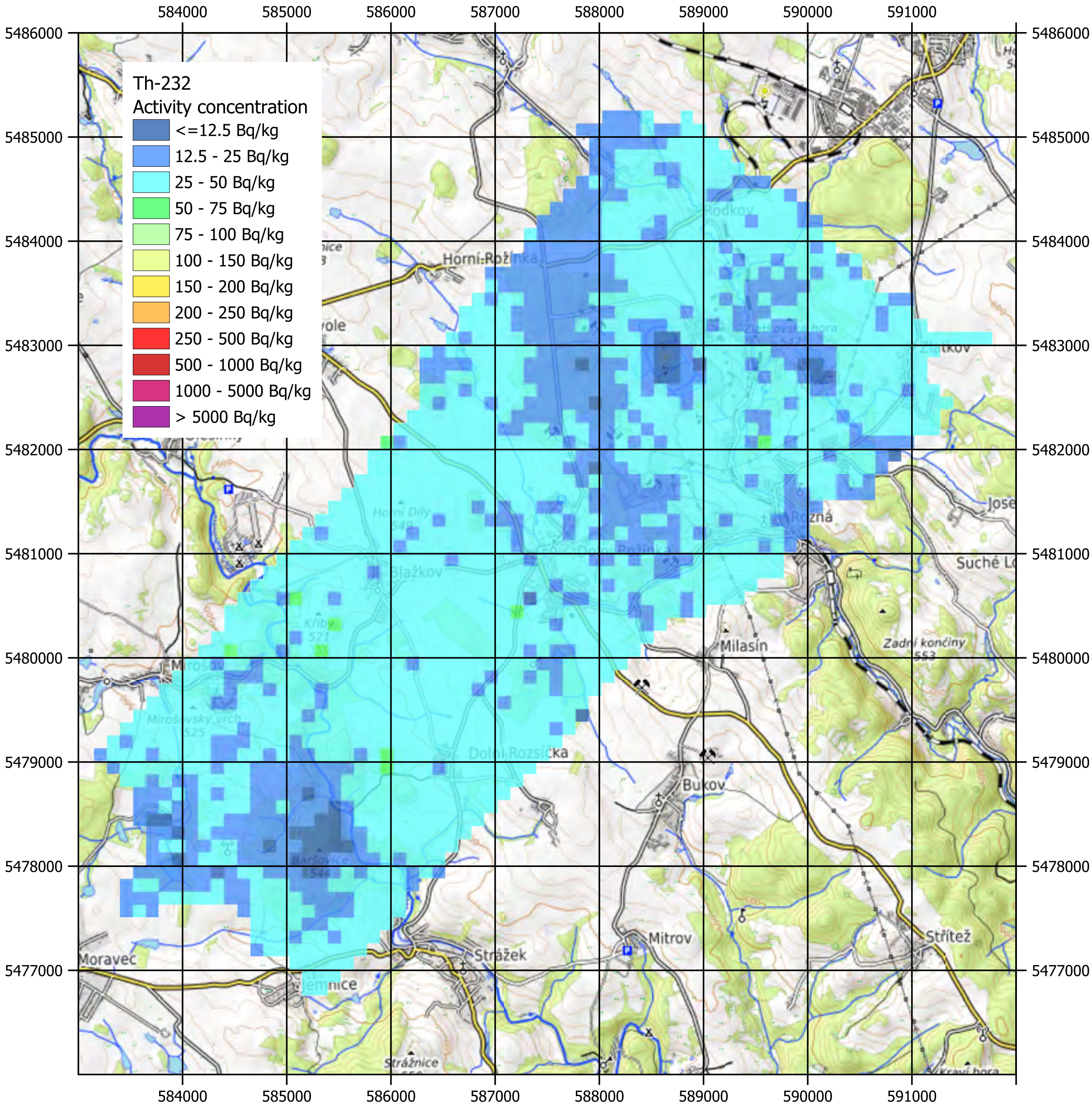

Figure 68: ^{232}Th activity concentration measured at VYS. Geodata©OpenTopoMap.

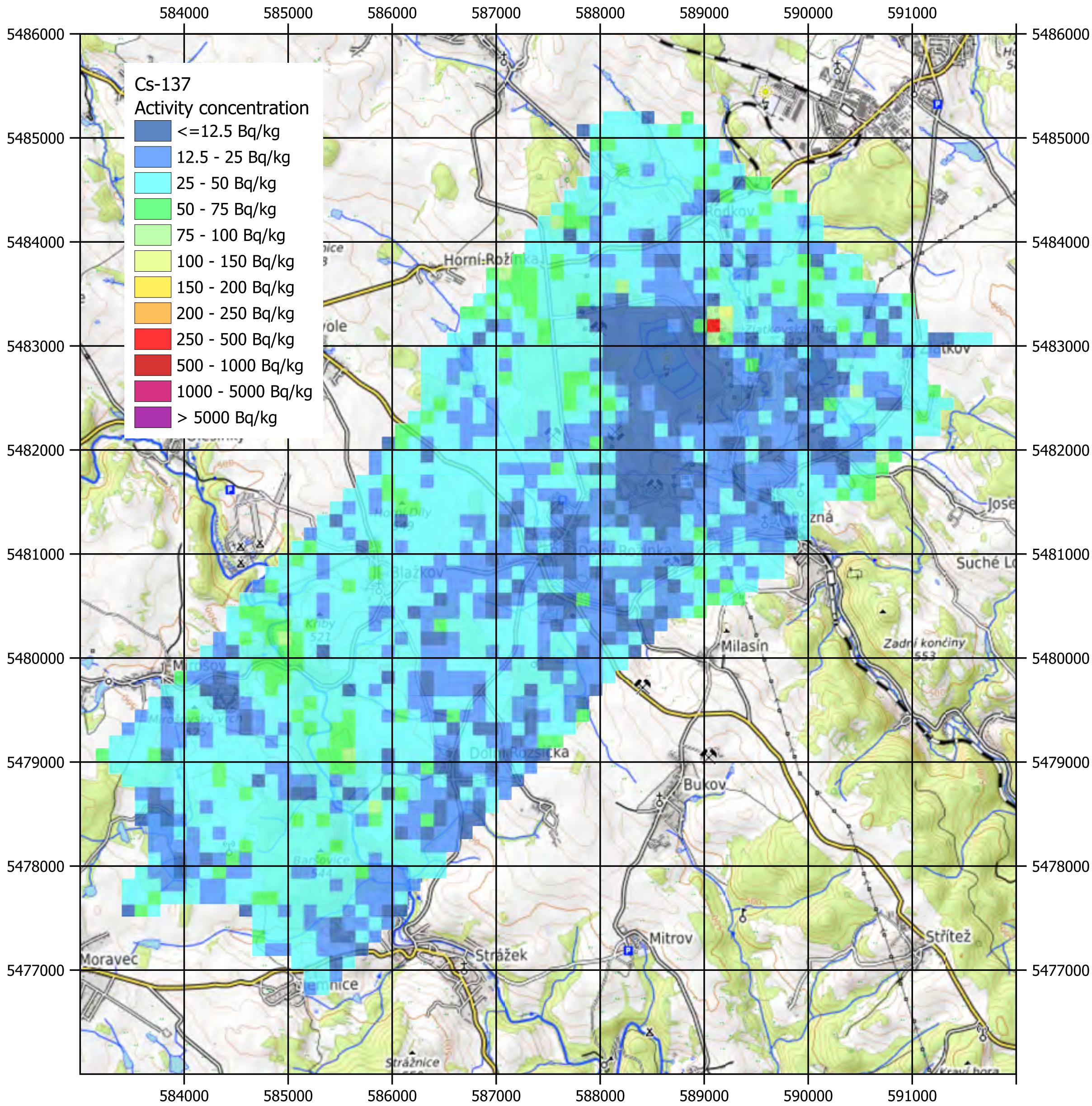

Figure 69: ^{137}Cs activity concentration measured at VYS. Geodata©OpenTopoMap.

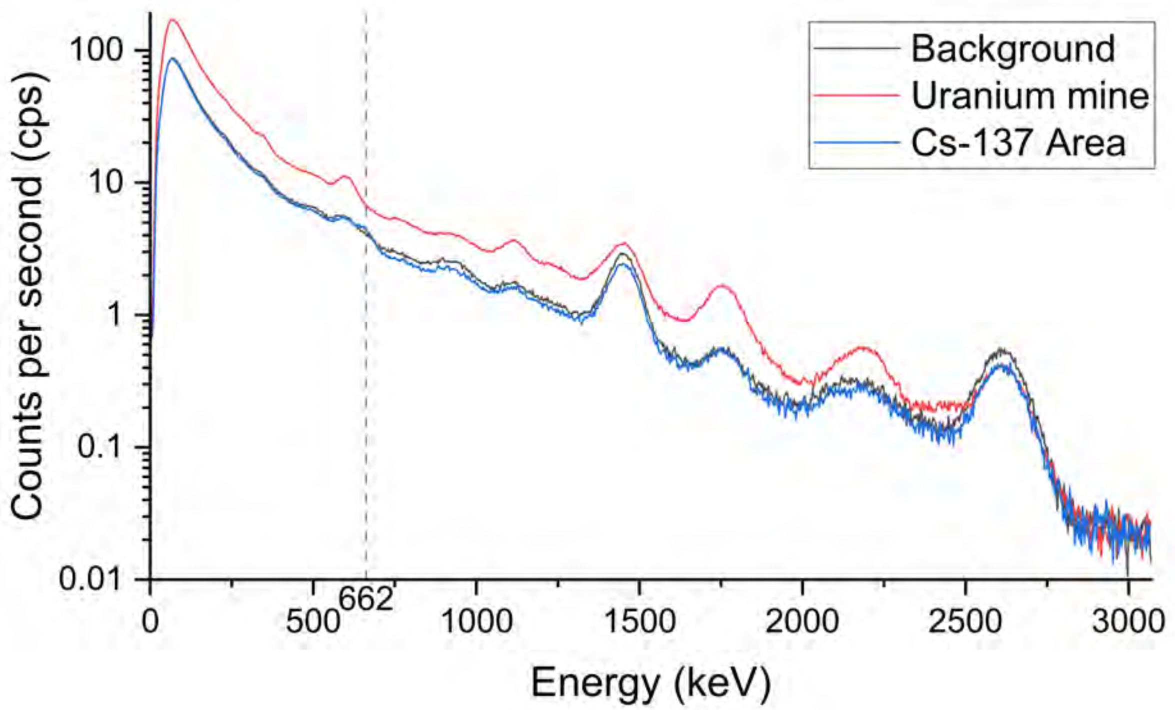

Figure 70: Spectra acquired at VYK. Background, area over the uranium mine, area affected by Chernobyl ^{137}Cs fallout.

3.2.4 Task 3: OPA

The dose rate map obtained from measurements with the RLL system during the task devoted to composite mapping is shown in Figure 71, displaying fairly homogeneous values (0.09 μSv/h - 0.15 μSv/h) across the entire region, except for a small area northwest of Jakubčovice, where a stone quarry is located. The exposed bare stone of the quarry results in higher values in the activity concentration map of ^{40}K, as observed in Figure 72. The ^{238}U and ^{232}Th activity concentration maps, shown in Figure 73 and 74, do not exhibit values beyond the expected background levels.

On the contrary, maps of the MMCG-Ratio and ^{137}Cs activity concentration, presented in Figure 75 and Figure 76, identify an extensive region between coordinates (5526000E, 710000N) and (5530000E, 720000N) with elevated values. The presence of ^{137}Cs can also be confirmed by inspecting the spectrum for this area (Figure 77). Discussions with Czech colleagues verified the presence of ^{137}Cs in the region, as documented in the literature, originating from the Chernobyl accident.

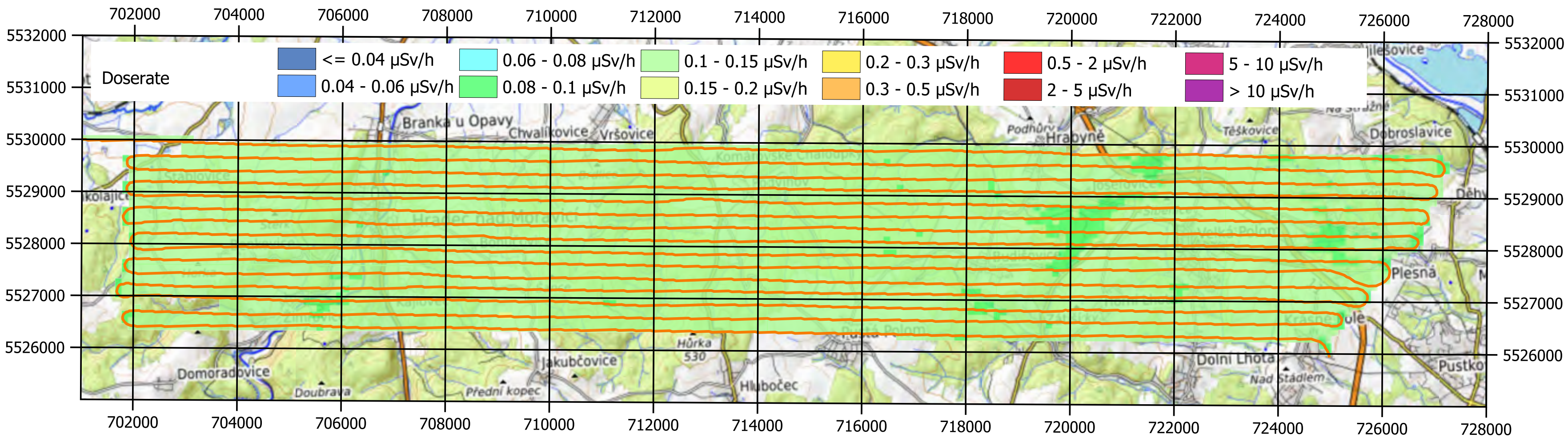

Figure 71: Dose rate measured at OPA. Geodata©OpenTopoMap.

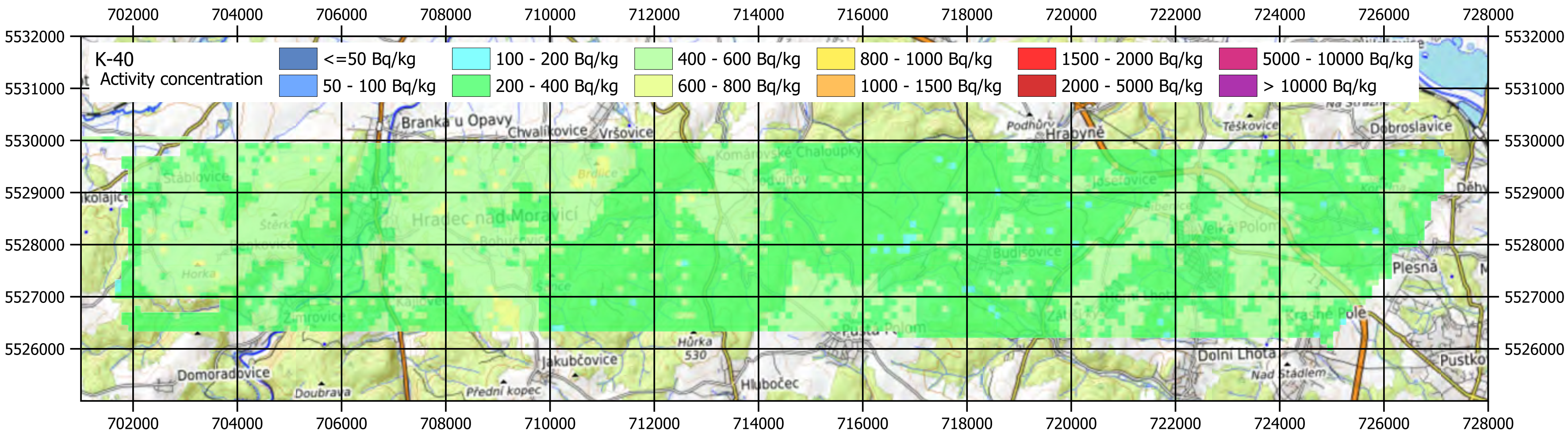

Figure 72: ^{40}K activity concentration measured at OPA. Geodata©OpenTopoMap.

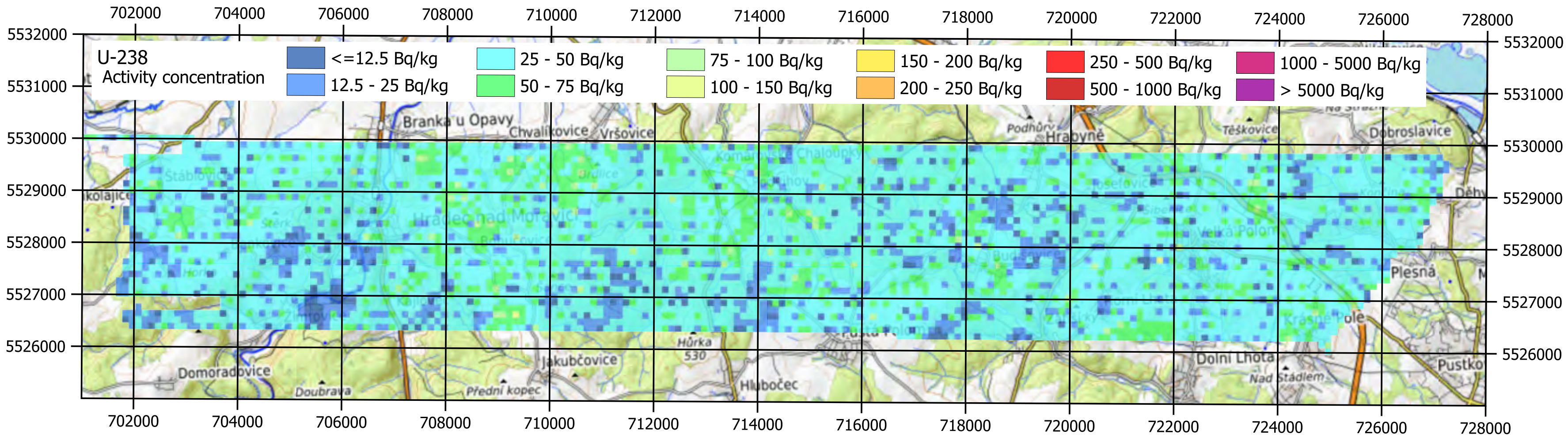

Figure 73: ^{238}U activity concentration measured at OPA. Geodata©OpenTopoMap.

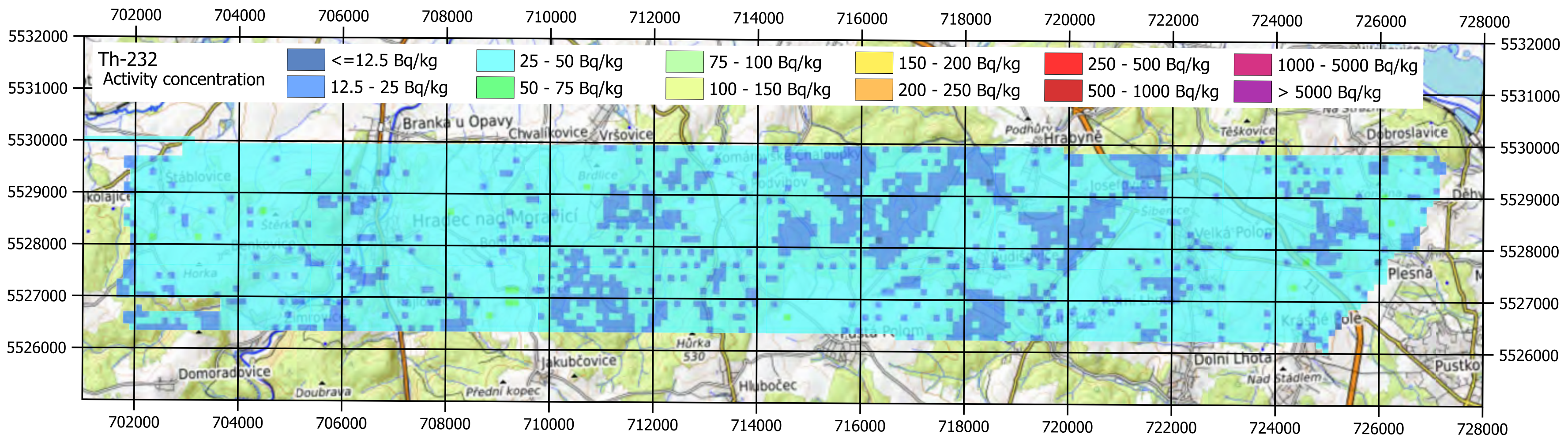

Figure 74: ^{232}Th activity concentration measured at OPA. Geodata©OpenTopoMap.

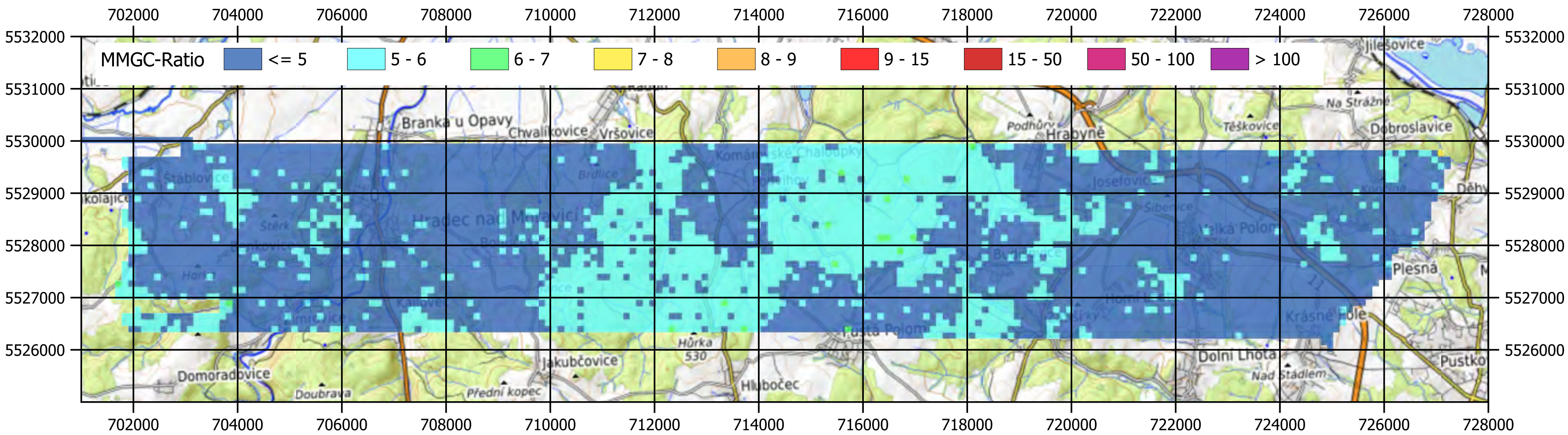

Figure 75: MMGC-Ratio measured at OPA. Geodata©OpenTopoMap.

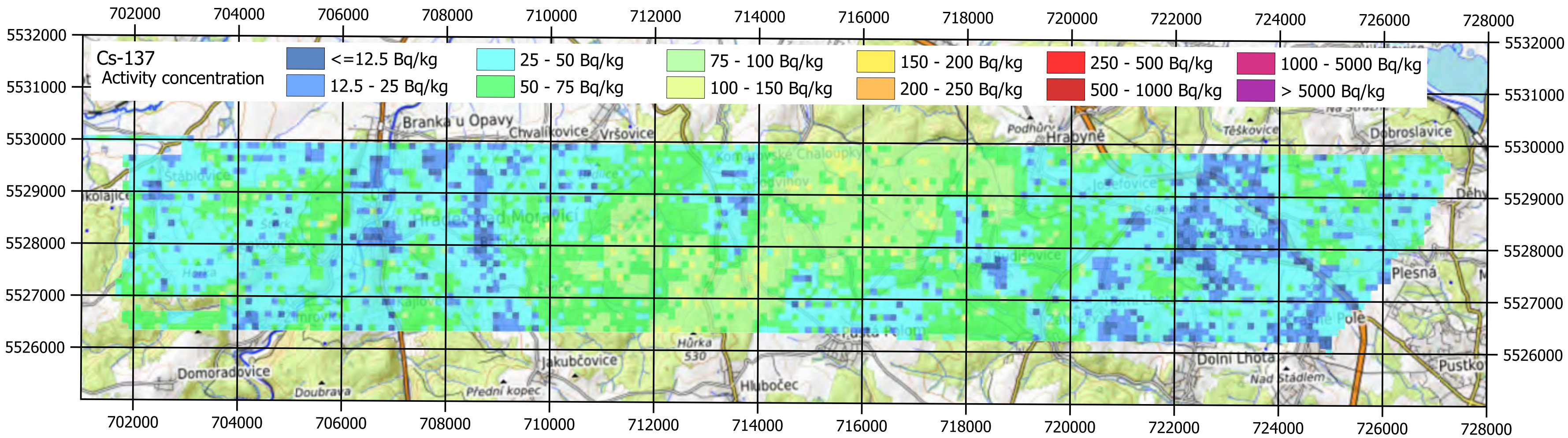

Figure 76: ^{137}Cs activity concentration measured at OPA. Geodata©OpenTopoMap.

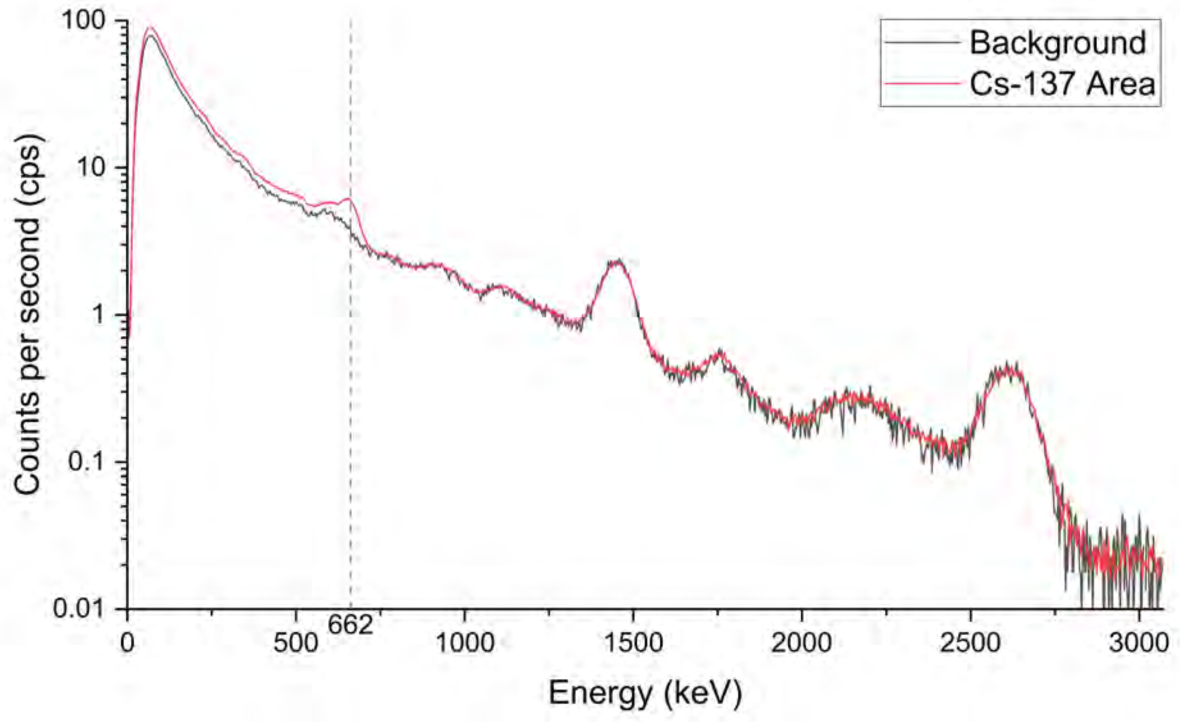

Figure 77: Spectra acquired at OPA. Background, area affected by Chernobyl ^{137}Cs fallout.

3.2.5 Task 4: LIB

Preparation for this specific task required a bit more effort, since an optimised flying path had to be devised in order to cover the whole target area without crossing the jagged boundary defined by the blue line in Figure 13. Within the allotted 90-minute time frame, the Swiss team opted to conduct two measurement flights employing different sampling modalities. The first (Measurement 1) utilised a sampling rate of 1 Hz with a standard integration time of 1 s, while the second maintained the same sampling rate of 1 Hz but employed an extended integration time of 5 s, effectively sampling spectra with a moving average over 5 seconds. This second acquisition modality can be activated to facilitate nuclide identification, owing to the improved statistics derived from the longer integration time, albeit at the expense of localisation precision and, consequently, activity estimation. Maps corresponding to both measurements, based on the differing acquisition settings, have been produced. The source activity estimation was derived using the standard sampling modality (integration time of 1 s).

The flight lines and dose rate maps pertaining the two measurements are illustrated in Figures 78 and 79, respectively. Already during the first flight two locations of interest were identified, denominated in the figures as point A (688220E, 5501752N) and point B (684925E, 5498813N). The ambient dose equivalent rate registered at point A indicates point sources with larger activities, whereas point B showed a milder increase of the dose rates, suggesting a lower source activity. For this reason, during the second measurements flight lines were thickened in correspondence of point B, to achieve better statistics. The smeared hotspots identified in Figure 79 in comparison to Figure 78 result from the extended integration time and hence worse precision in localisation.

The maps of the MMGC-Ratio obtained from the two measurements are illustrated in Figures 80 and 81 and identify the same points of interest. In comparison to dose rate maps, the signal of the radioactive sources is much more obvious, not only for point A, where sources used are expected to have higher activity, but also for point B, where the dose rate increase registered is not substantially marked. For radioactive source search especially, calculating the MMGC-Ratio confirms to be an effective strategy to locate even weaker sources (for nuclides whose emission energies are < 1.4 MeV).

Spectra acquired over the points of interest A, B and of background are reported in Figure 82 for each measurement flight 1 and 2. Concerning nuclide identification, the peaks of ^{60}Co at 1173 keV and 1332 keV and the one of ^{137}Cs at 661 keV are clearly distinguishable for the spectra acquired at point A. Spectra at point B feature again a ^{137}Cs peak and an additional one centred on the energy of 350keV, attributed to ^{131}I.

An estimation of the activity of the sources is provided in Table 6. The estimation with AGS_CH used the data of Measurement 1 and could be performed only for the ^{137}Cs and ^{60}Co nuclides. It could not be carried out for ^{131}I due to the absence of a dedicated nuclide calibration. The initial evaluation results provided during the exercise are also presented in Table 6. These were instead derived from the data of Measurement 2, as the Mirion software required a nuclide identification to carry out an activity assessment.

Site	Nuclide	Estimated Activity [GBq]	
		Mirion (5 s)	AGS_CH
A	^{137}Cs	1.3	1.9(2)
A	^{60}Co	4.2	3.6(6)
B	^{137}Cs	0.48	0.8(3)
B	^{131}I	0.69	n/a

Table 6: Radioactive sources activities estimated at LIB.

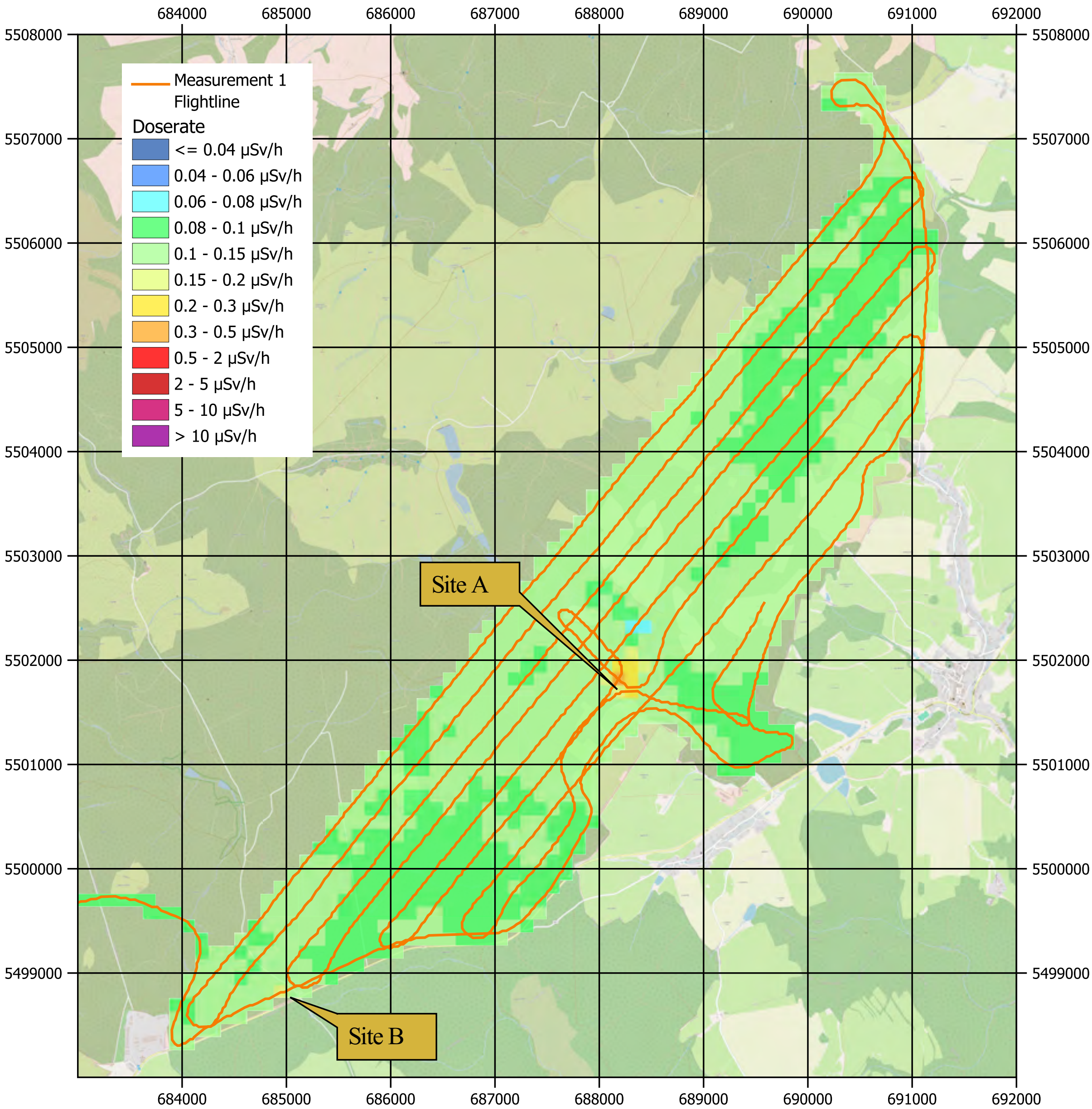

Figure 78: Dose rate measured at LIB during the first measurement. Geodata©OpenStreetMap.

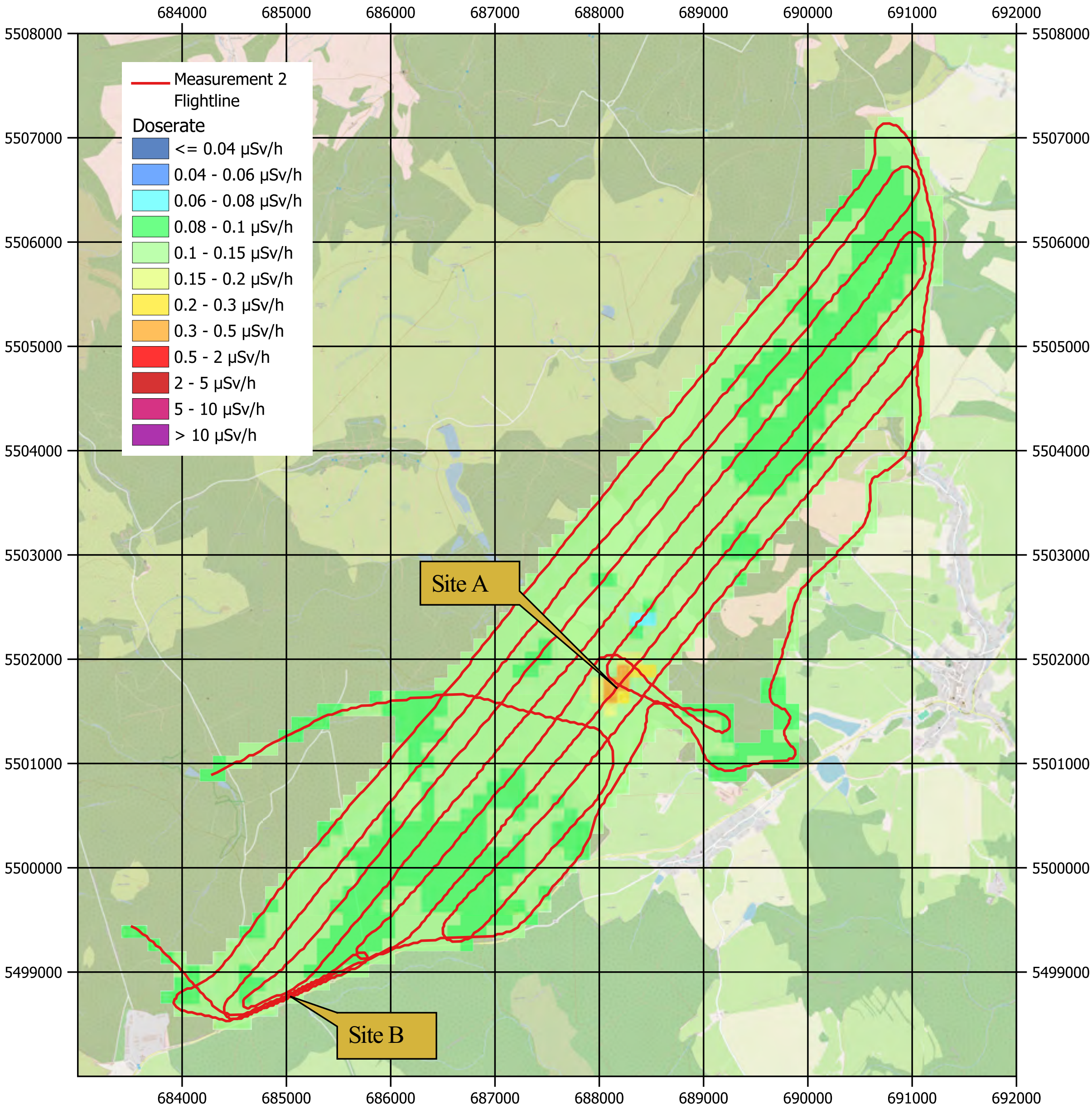

Figure 79: Dose rate measured at LIB during the second measurement. Geodata©OpenStreetMap.

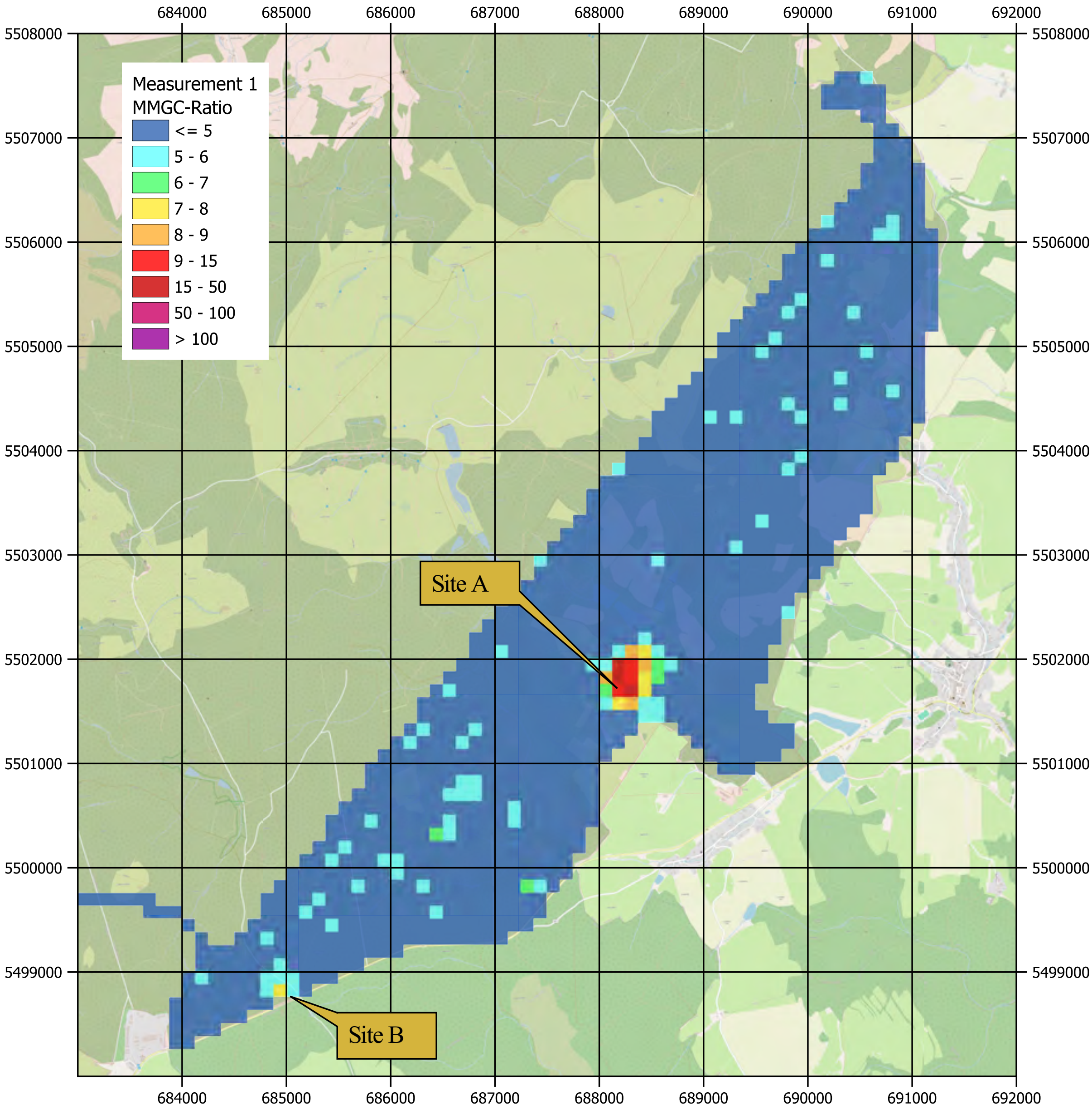

Figure 80: MMGC-Ratio measured at LIB during the first measurement. Geodata©OpenStreetMap.

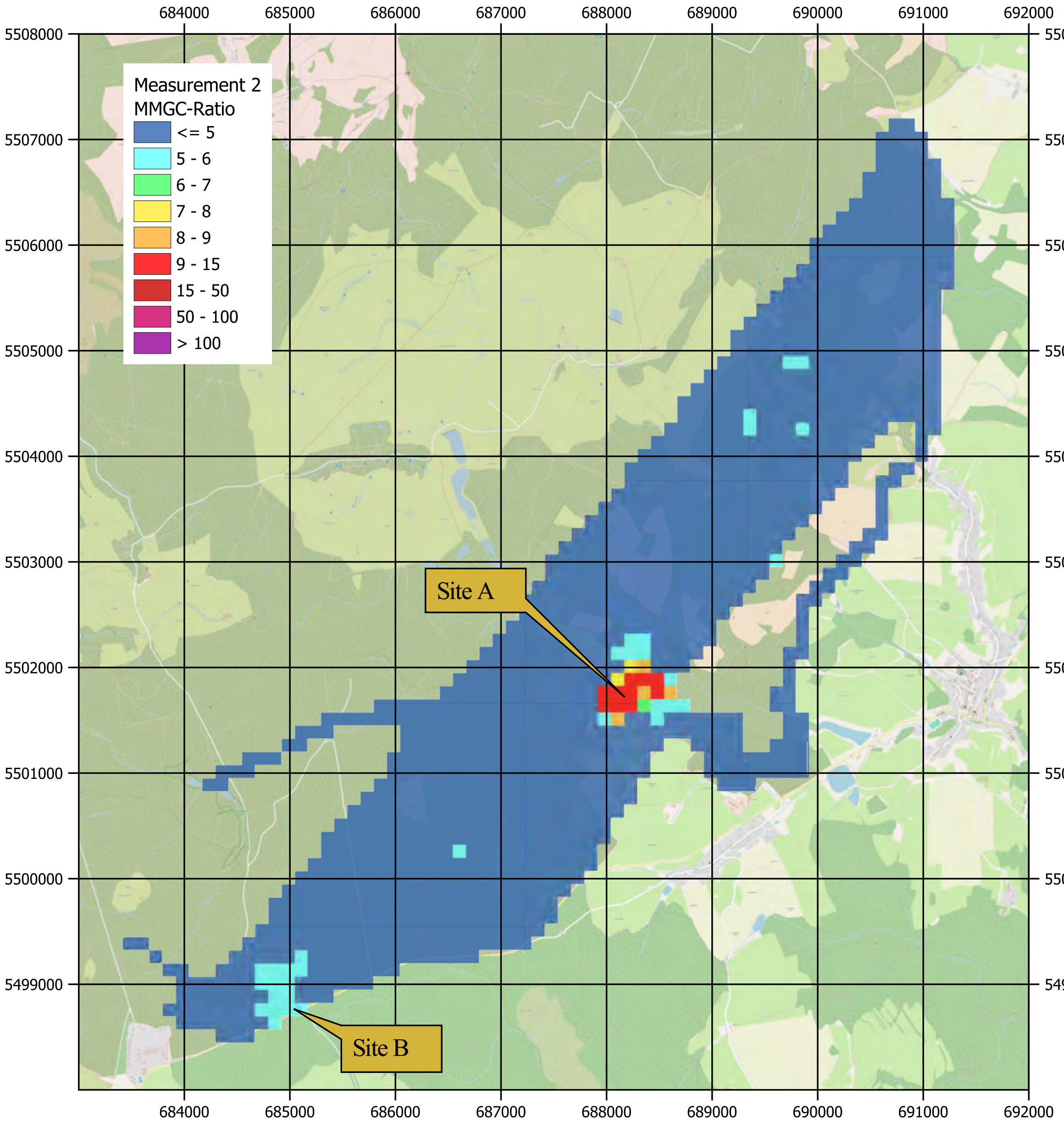

Figure 81: MMGC-Ratio measured at LIB during the second measurement. Geodata©OpenStreetMap.

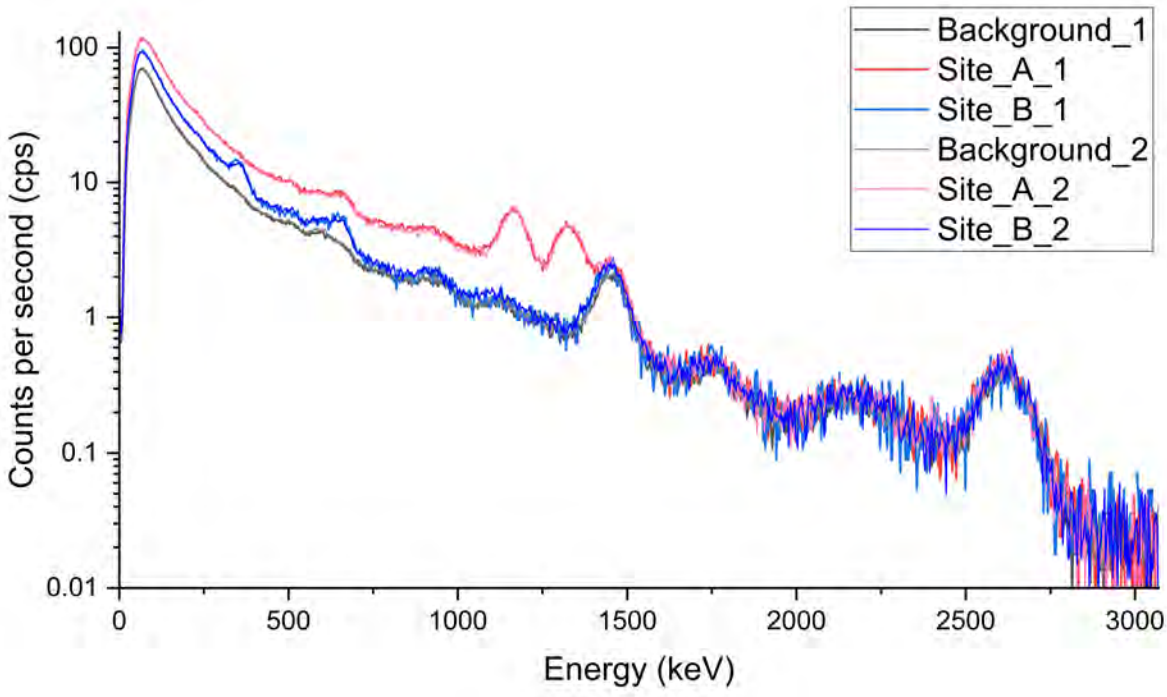

Figure 82: Spectra acquired at LIB. Background, Site A, Site B.

4 Conclusions

Measurements in the area of Bürgenstock, were carried out a few weeks before the High Level Conference on Peace in Ucraine (HLCPU) to obtain reference values for the area. The region, characterised by steep cliffs overlooking lake of Lucerne, provided an additional flight challenge that could be effectively trained. Results show values consistent with the typical background levels of the area.

Measurements conducted on behalf of ENSI during the civil exercise (ARM24c) were carried out in the vicinity of several Swiss nuclear power plants and facilities, including the Beznau and Leibstadt nuclear power plants, the Zwilag interim storage facility, and the research facilities of the Paul Scherrer Institute. Within the premises of the Leibstadt nuclear power plant (KKL), which was in the process of resuming operations, the usual presence of ^{16}N was detected. As in previous assessments, short-lived atmospheric and terrestrial anthropogenic radionuclides were identified in the western area of the Paul Scherrer Institute. This report highlights the application of a novel evaluation method, based on a full-spectrum Bayesian inversion approach, which enabled the identification and quantification of the atmospheric and terrestrial anthropogenic radionuclides produced by the research facilities using the aeroradiometry system. All of the emissions observed are authorised and are subject to rigorous monitoring by the regulatory authorities. No deviations from natural background radiation levels were detected on the premises and in the vicinity of the Beznau nuclear power plant (KKB) and the Zwilag interim storage facility.

The ARM24m campaign surveyed regions in western Switzerland adjacent, to the areas screened by previous exercises. Due to adverse weather conditions, the regions of Concise and Sainte-Croix could not be entirely surveyed and will be completed in future exercises. Some of the crystals of the system RLL 004, used for the military exercise, experienced issues during the measurements that affected the raw data. The evaluation could nonetheless be successfully carried out, by excluding the contribution of the crystals affected. The results indicate dose rate levels in line with the background and normal activity concentrations with variations reflecting the geology of the regions. Traces of ^{137}Cs, attributable to the Chernobyl fallout, were detected in some of the areas. Such deposits have previously been identified in adjacent regions and documented in earlier reports. The ^{137}Cs activity concentrations detected are minimal and pose no radiological concern.

The international exercise AGC24 in the Czech Republic was successfully conducted, reaffirming the importance of international collaboration. Such exercises provide valuable opportunities to compare and refine methodologies, practise measurements under unique conditions not present in the national territory but pertinent to emergency scenarios, and harmonise procedures and data formats. These efforts contribute to smoother and more efficient international support during radiological emergencies. In this regard, the adoption of the ERS 2.0 format for exchanging raw data and results proved highly effective in ensuring data compatibility.

5 Literature

Ahdida, C., Bozzato, D., Calzolari, D., Cerutti, F., Charitonidis, N., Cimmino, A., Coronetti, A., D'Alessandro, G.L., Donadon Servelle, A., Esposito, L.S., Froeschl, R., García Alía, R., Gerbershagen, A., Gilardoni, S., Horváth, D., Hugo, G., Infantino, A., Kouskoura, V., Lechner, A., Lefebvre, B., Lerner, G., Magistris, M., Manousos, A., Moryc, G., Ogallar Ruiz, F., Pozzi, F., Prelipcean, D., Roesler, S., Rossi, R., Sabaté Gilarte, M., Salvat Pujol, F., Schoofs, P., Stránský, V., Theis, C., Tsinganis, A., Versaci, R., Vlachoudis, V., Waets, A., Widorski, M.: New Capabilities of the FLUKA Multi-Purpose Code. Frontiers in Physics 9, 2022.
DOI https://doi.org/10.3389/fphy.2021.788253

Breitenmoser, D.: Towards Monte Carlo based Full Spectrum Modeling of Airborne Gamma-Ray Spectrometry Systems. Dissertation Nr. 30551, ETH Zurich, 2024.
DOI https://doi.org/10.3929/ethz-b-000694094
arXiv https://doi.org/10.48550/arXiv.2411.02606

Breitenmoser, D., Cerutti, F., Butterweck, G., Kasprzak, M.M., Mayer, S.: Emulator-based Bayesian inference on non-proportional scintillation models by compton-edge probing. Nature Communications 14, 2023.
DOI https://doi.org/10.1038/s41467-023-42574-y
arXiv https://doi.org/10.48550/arXiv.2302.05641

Bucher, B.: Methodische Weiterentwicklungen in der Aeroradiometrie. Dissertation Nr. 13973, ETH Zürich, 2001.

Goodman, J., Weare, J.: Ensemble samplers with affine invariance. Communications in Applied Mathematics and Computational Science 5, 2010.
DOI https://doi.org/10.2140/CAMCOS.2010.5.65

Marelli, S., Sudret, B., 2014. UQLab: A Framework for Uncertainty Quantification in Matlab. 2nd International Conference on Vulnerability and Risk Analysis and Management, 2014.
DOI https://doi.org/10.1061/9780784413609.257

Pawlowicz, R.: M_Map: A mapping package for MATLAB. Earth, Ocean & Atmospheric Sciences (EOAS), 2020.
URL https://www.eoas.ubc.ca/~rich/map.html

Perrakis, K., Ntzoufras, I., Tsionas, E.G.: On the use of marginal posteriors in marginal likelihood estimation via importance sampling. Computational Statistics & Data Analysis 77, 2014.
DOI https://doi.org/10.1016/j.csda.2014.03.004

Schwarz, G. F.: Methodische Entwicklungen zur Aerogammaspektrometrie. Beiträge zur Geologie der Schweiz, Geophysik Nr. 23, Schweizerische Geophysikalische Kommission, 1991.

Trotta, R.: Bayes in the sky: Bayesian inference and model selection in cosmology. Contemporary Physics 49, 2008.
DOI https://doi.org/10.1080/00107510802066753

6 Previous reports

Schwarz, G. F., Klingelé, E. E., Rybach, L.: Aeroradiometrische Messungen in der Umgebung der schweizerischen Kernanlagen. Bericht für das Jahr 1989 zuhanden der Hauptabteilung für die Sicherheit der Kernanlagen (HSK). Interner Bericht, Institut für Geophysik, ETH Zürich, 1990.

Schwarz, G. F., Klingelé, E. E., Rybach, L.: Aeroradiometrische Messungen in der Umgebung der schweizerischen Kernanlagen. Bericht für das Jahr 1990 zuhanden der Hauptabteilung für die Sicherheit der Kernanlagen (HSK). Interner Bericht, Institut für Geophysik, ETH Zürich, 1991.

Schwarz, G. F., Klingelé, E. E., Rybach, L.: Aeroradiometrische Messungen in der Umgebung der schweizerischen Kernanlagen. Bericht für das Jahr 1991 zuhanden der Hauptabteilung für die Sicherheit der Kernanlagen (HSK). Interner Bericht, Institut für Geophysik, ETH Zürich, 1992.

Schwarz, G. F., Klingelé, E. E., Rybach, L.: Aeroradiometrische Messungen in der Umgebung der schweizerischen Kernanlagen. Bericht für das Jahr 1992 zuhanden der Hauptabteilung für die Sicherheit der Kernanlagen (HSK). Interner Bericht, Institut für Geophysik, ETH Zürich, 1993.

Schwarz, G. F., Klingelé, E. E., Rybach, L.: Aeroradiometrische Messungen in der Umgebung der schweizerischen Kernanlagen. Bericht für das Jahr 1993 zuhanden der Hauptabteilung für die Sicherheit der Kernanlagen (HSK). Interner Bericht, Institut für Geophysik, ETH Zürich, 1994.

Schwarz, G. F., Rybach, L.: Aeroradiometrische Messungen im Rahmen der Übung ARM94. Bericht für das Jahr 1994 zuhanden der Fachgruppe Aeroradiometrie (FAR). Interner Bericht, Institut für Geophysik, ETH Zürich, 1995.

Schwarz, G. F., Rybach, L.: Aeroradiometrische Messungen im Rahmen der Übung ARM95. Bericht für das Jahr 1995 zuhanden der Fachgruppe Aeroradiometrie (FAR). Interner Bericht, Institut für Geophysik, ETH Zürich, 1996.

Schwarz, G. F., Rybach, L., Bärlocher, C.: Aeroradiometrische Messungen im Rahmen der Übung ARM96. Bericht für das Jahr 1996 zuhanden der Fachgruppe Aeroradiometrie (FAR). Interner Bericht, Institut für Geophysik, ETH Zürich, 1997.

Bucher, B., Rybach, L., Schwarz, G., Bärlocher, C.: Aeroradiometrische Messungen im Rahmen der Übung ARM97. Bericht für das Jahr 1997 zuhanden der Fachgruppe Aeroradiometrie (FAR). Interner Bericht, Institut für Geophysik, ETH Zürich, 1998.

Bucher, B., Rybach, L., Schwarz, G., Bärlocher, C.: Aeroradiometrische Messungen im Rahmen der Übung ARM98. Bericht für das Jahr 1998 zuhanden der Fachgruppe Aeroradiometrie (FAR). Interner Bericht, Institut für Geophysik, ETH Zürich, 1999.

Bucher, B., Rybach, L., Schwarz, G., Bärlocher, C.: Aeroradiometrische Messungen im Rahmen der Übung ARM99. Bericht für das Jahr 1999 zuhanden der Fachgruppe Aeroradiometrie (FAR). Interner Bericht, Institut für Geophysik, ETH Zürich, 2000.

Bucher, B., Rybach, L., Schwarz, G., Bärlocher, C.: Aeroradiometrische Messungen im Rahmen der Übung ARM00. Bericht für das Jahr 2000 zuhanden der Fachgruppe Aeroradiometrie (FAR). Interner Bericht, Institut für Geophysik, ETH Zürich, 2001.

Bucher, B., Rybach, L., Schwarz, G., Bärlocher, C.: Aeroradiometrische Messungen im Rahmen der Übung ARM01. Bericht für das Jahr 2001 zuhanden der Fachgruppe Aeroradiometrie (FAR). Interner Bericht, Paul Scherrer Institut, Villigen, Schweiz, 2002.

Bucher, B., Rybach, L., Schwarz, G., Bärlocher, C.: Aeroradiometrische Messungen im Rahmen der Übung ARM02. Bericht für das Jahr 2002 zuhanden der Fachgruppe Aeroradiometrie (FAR). Interner Bericht, Paul Scherrer Institut, Villigen, Schweiz, 2003.

Bucher, B., Rybach, L., Schwarz, G.: Aeroradiometrische Messungen im Rahmen der Übung ARM03. PSI-Bericht 04-14, ISSN 1019-0643, Paul Scherrer Institut, Villigen, Schweiz, 2004.

Bucher, B., Butterweck, G., Rybach, L., Schwarz, G.: Aeroradiometrische Messungen im Rahmen der Übung ARM04. PSI-Bericht 05-10, ISSN 1019-0643, Paul Scherrer Institut, Villigen, Schweiz, 2005.
DOI `https://doi.org/10.55402/psi:41689`

Bucher, B., Butterweck, G., Rybach, L., Schwarz, G.: Aeroradiometrische Messungen im Rahmen der Übung ARM05. PSI-Bericht 06-06, ISSN 1019-0643,Paul Scherrer Institut, Villigen, Schweiz, 2006.
DOI `https://doi.org/10.55402/psi:41685`

Bucher, B., Butterweck, G., Rybach, L., Schwarz, G.: Aeroradiometrische Messungen im Rahmen der Übung ARM06. PSI-Bericht 07-02, ISSN 1019-0643, Paul Scherrer Institut, Villigen, Schweiz, 2007.
DOI `https://doi.org/10.55402/psi:41681`

Bucher, B., Guillot, L., Strobl, C., Butterweck, G., Gutierrez, S., Thomas, M., Hohmann, C., Krol, I., Rybach, L., Schwarz, G.: International Intercomparison Exercise of Airborne Gammaspectrometric Systems of Germany, France and Switzerland in the Framework of the Swiss Exercise ARM07. PSI-Bericht Nr. 09-07, ISSN 1019-0643, Paul Scherrer Institut, Villigen, Schweiz, 2009.
DOI `https://doi.org/10.55402/psi:35550`

Bucher, B., Butterweck, G., Rybach, L., Schwarz, G.: Aeroradiometrische Messungen im Rahmen der Übung ARM08. PSI-Bericht Nr. 09-02, ISSN 1019-0643, Paul Scherrer Institut, Villigen, Schweiz, 2009.
DOI `https://doi.org/10.55402/psi:35581`

Bucher, B., Butterweck, G., Rybach, L., Schwarz, G., Strobl, C.: Aeroradiometrische Messungen im Rahmen der Übung ARM09. PSI-Bericht Nr. 10-01, ISSN 1019-0643, Paul Scherrer Institut, Villigen, Schweiz, 2010.
DOI `https://doi.org/10.55402/psi:35541`

Bucher, B., Butterweck, G., Rybach, L., Schwarz, G., Mayer, S.: Aeroradiometrische Messungen im Rahmen der Übung ARM10. PSI-Bericht Nr. 11-02, ISSN 1019-0643, Paul Scherrer Institut, Villigen, Schweiz, 2011.
DOI `https://doi.org/10.55402/psi:35201`

Bucher, B., Butterweck, G., Rybach, L., Schwarz, G., Mayer, S.: Aeroradiometric Measurements in the Framework of the Swiss Exercise ARM11. PSI-Report No. 12-04, ISSN 1019-0643, Paul Scherrer Institut, Villigen, Switzerland, 2012.
DOI `https://doi.org/10.55402/psi:35137`

Butterweck, G., Bucher, B., Rybach, L., Schwarz, G., Hödlmoser, H., Mayer, S., Danzi, C. Scharding, G.: Aeroradiometric Measurements in the Framework of the Swiss Exercise ARM12. PSI-Report No. 13-01, ISSN 1019-0643, Paul Scherrer Institut, Villigen, Switzerland, 2013.
DOI https://doi.org/10.55402/psi:35134

Butterweck, G., Bucher, B., Rybach, L., Schwarz, G., Hohmann, E., Mayer, S., Danzi, C. Scharding, G.: Aeroradiometric Measurements in the Framework of the Swiss Exercise ARM13. PSI-Report No. 15-01, ISSN 1019-0643, Paul Scherrer Institut, Villigen, Switzerland, 2015.
DOI https://doi.org/10.55402/psi:35064

Butterweck, G., Bucher, B., Rybach, L., Schwarz, G., Hohmann, E., Mayer, S., Danzi, C. Scharding, G.: Aeroradiometric Measurements in the Framework of the Swiss Exercises ARM14 and FTX14. PSI-Report No. 15-02, ISSN 1019-0643, Paul Scherrer Institut, Villigen, Switzerland, 2015.
DOI https://doi.org/10.55402/psi:35062

Butterweck, G., Bucher, B., Rybach, L., Schwarz, G., Hofstetter-Boillat, B., Hohmann, E., Mayer, S., Danzi, C. Scharding, G.: Aeroradiometric Measurements in the Framework of the Swiss Exercises ARM15, GNU15 and the International Exercise AGC15. PSI-Report No. 15-04, ISSN 1019-0643, Paul Scherrer Institut, Villigen, Switzerland, 2015.
DOI https://doi.org/10.55402/psi:35047

Butterweck, G., Bucher, B., Rybach, L., Poretti, C., Maillard, S., Schwarz, G., Hofstetter-Boillat, B., Hohmann, E., Mayer, S., Scharding, G.: Aeroradiometric Measurements in the Framework of the Swiss Exercises ARM16 and LAURA. PSI-Report No. 17-01, ISSN 1019-0643, Paul Scherrer Institut, Villigen, Switzerland, 2017.
DOI https://doi.org/10.55402/psi:34988

Butterweck, G., Bucher, B., Gryc, L., Debayle, C., Strobl, C., Maillard, S., Thomas, M., Helbig, A., Krol, I., Chuzel, S., Couvez, C., Ohera, M., Rybach, L., Poretti, C., Hofstetter-Boillat, B., Mayer, S., Scharding, G.: International Intercomparison Exercise of Airborne Gamma-Spectrometric Systems of the Czech Republic, France, Germany and Switzerland in the Framework of the Swiss Exercise ARM17. PSI-Report No. 18-04, ISSN 1019-0643, Paul Scherrer Institut, Villigen, Switzerland, 2018.
DOI https://doi.org/10.55402/psi:34959,

Butterweck, G., Bucher, B., Rybach, L., Poretti, C., Maillard, S., Schindler, M., Hofstetter-Boillat, B., Mayer, S., Scharding, G.: Aeroradiometric Measurements in the Framework of the Swiss Exercises ARM18 and the International Exercise CONTEX 2018. PSI-Report No. 19-01, ISSN 1019-0643, Paul Scherrer Institut, Villigen, Switzerland, 2019.
DOI https://doi.org/10.55402/psi:34957,

Butterweck, G., Bucher, B., Rybach, L., Poretti, C., Maillard, S., Schindler, M., Hofstetter-Boillat, B., Mayer, S., Scharding, G.: Aeroradiometric Measurements in the Framework of the Swiss Exercise ARM19. PSI-Report No. 20-01, ISSN 1019-0643, Paul Scherrer Institut, Villigen, Switzerland, 2020.
DOI https://doi.org/10.55402/psi:44919

Butterweck, G., Bucher, B., Breitenmoser, D., Rybach, L., Poretti, C., Maillard, S., Kasprzak, M., Ferreri, G., Gurtner, A., Astner, M., Hauenstein, F., Straub, M., Bucher, M., Harm, C., Scharding, G., Mayer, S.: Aeroradiometric Measurements in the Framework of the Swiss Exercise ARM20. PSI-Report No. 21-01, ISSN 1019-0643, Paul Scherrer Institut, Villigen, Switzerland, 2021.
DOI https://doi.org/10.13140/RG.2.2.15326.51526

Butterweck, G., Bucher, B., Breitenmoser, D., Rybach, L., Poretti, C., Maillard, S., Hess, A., Kasprzak, M., Scharding, G., Mayer, S.: Aeroradiometric Measurements in the Framework of the Swiss Exercise ARM21. PSI-Report No. 22-02, ISSN 1019-0643, Paul Scherrer Institut, Villigen, Switzerland, 2022.
DOI https://doi.org/10.55402/psi:44921

Butterweck, G., Stabilini, A., Bucher, B., Breitenmoser, D., Rybach, L., Poretti, C., Maillard, S., Hess, A., Kasprzak, M., Scharding, G., Mayer, S.: Aeroradiometric Measurements in the Framework of the Swiss Exercise ARM22. PSI-Report No. 23-01, ISSN 1019-0643, Paul Scherrer Institut, Villigen, Switzerland, 2023.
DOI https://doi.org/10.55402/psi:51194

Butterweck, G., Stabilini, A., Bucher, B., Breitenmoser, D., Rybach, L., Poretti, C., Maillard, S., Hess, A., Hauenstein, F., Gendotti, U., Kasprzak, M., Scharding, G., Mayer, S.: Aeroradiometric Measurements in the Framework of the Swiss Exercise ARM23. PSI-Report No. 24-02, ISSN 1019-0643, Paul Scherrer Institut, Villigen, Switzerland, 2023.
DOI https://doi.org/10.55402/psi:60054

The reports since 1989 can be found and downloaded from the FAR website https://far.ensi.ch. under Publications; the reports 1989 - 2006 only in German.

7 Evaluation parameters

The parameters used for data evaluation are stored in the header section of each generated ERS 2.0 file. The header section used in the current exercise are listed below.

7.1 Detector RLL 001

These evaluation parameters were used for the evaluation of the measurements in Switzerland and the international exercise AGC24, with detector RLL 001.

```
V 2.0
HSW AGS_CH V0.0
HORG Nationale Alarmzentrale NAZ
HCTRY Switzerland
IAP Mirion 16l Container
ICA Superpuma
IPG From ARINC bus of helicopter
HSITE PSI-KKB-KKL
/* Parameters used for data evaluation---------------------------------------------------------------------
/* No data value;MND -999
/* Energy calibration;ISE0 0;ISE1 3;ISE2 0
/* Energy calibration;ISE0_D01 0;ISE1_D01 3;ISE2_D01 0
/* Energy calibration;ISE0_D02 0;ISE1_D02 3;ISE2_D02 0
/* Energy calibration;ISE0_D03 0;ISE1_D03 3;ISE2_D03 0
/* Energy calibration;ISE0_D04 0;ISE1_D04 3;ISE2_D04 0
/* Energy calibration;ISE0_D05 0;ISE1_D05 3;ISE2_D05 0
/* Energy windows------------------------------------------------------------------------------------------
ISW Total;ISWE1_Total 401;ISWE2_Total 2997;ISWB_Total 125.3;ISWC_Total 5.65;ISWT_Total 0.006;ISWRA_Total 0;ISWRB_Total 0
ISW K-40;ISWE1_K-40 1369;ISWE2_K-40 1558;ISWB_K-40 9.1;ISWC_K-40 0.3;ISWT_K-40 0.008;ISWRA_K-40 0;ISWRB_K-40 0
ISW U-238;ISWE1_U-238 1664;ISWE2_U-238 1853;ISWB_U-238 5.8;ISWC_U-238 0.23;ISWT_U-238 0.0055;ISWRA_U-238 0;ISWRB_U-238 0
ISW Th-232;ISWE1_Th-232 2407;ISWE2_Th-232 2797;ISWB_Th-232 0.5;ISWC_Th-232 0.28;ISWT_Th-232 0.006;ISWRA_Th-232 0;ISWRB_Th-232 0
ISW Cs-137;ISWE1_Cs-137 600;ISWE2_Cs-137 720;ISWB_Cs-137 19.6;ISWC_Cs-137 0.58;ISWT_Cs-137 0.01;ISWRA_Cs-137 0;ISWRB_Cs-137 0
ISW Co-60;ISWE1_Co-60 1100;ISWE2_Co-60 1400;ISWB_Co-60 12.2;ISWC_Co-60 0.65;ISWT_Co-60 0.008;ISWRA_Co-60 0;ISWRB_Co-60 0
```

```
ISW MMGC1;ISWE1_MMGC1 400;ISWE2_MMGC1 1400;ISWB_MMGC1 0;ISWC_MMGC1 0;ISWT_MMGC1 0.006;ISWRA_MMGC1 0;ISWRB_MMGC1 0
ISW MMGC2;ISWE1_MMGC2 1400;ISWE2_MMGC2 2997;ISWB_MMGC2 0;ISWC_MMGC2 0;ISWT_MMGC2 0.0065;ISWRA_MMGC2 0;ISWRB_MMGC2 0
ISW LOW;ISWE1_LOW 100;ISWE2_LOW 400;ISWB_LOW 0;ISWC_LOW 0;ISWT_LOW 0.02;ISWRA_LOW 0;ISWRB_LOW 0
ISW MID;ISWE1_MID 720;ISWE2_MID 2997;ISWB_MID 0;ISWC_MID 0;ISWT_MID 0.015;ISWRA_MID 0;ISWRB_MID 0
ISW SDI;ISWE1_SDI 240;ISWE2_SDI 2997;ISWB_SDI 85.5;ISWC_SDI 4.26;ISWT_SDI 0.0053;ISWRA_SDI 0;ISWRB_SDI 0
/* Stripping factors---------------------------------------------------------------------------------------
ISWS_U-238_K-40 0.931
ISWS_Th-232_K-40 0.478
ISWS_Co-60_K-40 0.067
ISWS_Th-232_U-238 0.362
ISWS_U-238_Th-232 0.049
ISWS_K-40_Cs-137 0.450
ISWS_U-238_Cs-137 3.161
ISWS_Th-232_Cs-137 1.654
ISWS_Co-60_Cs-137 0.154
ISWS_K-40_Co-60 0.758
ISWS_U-238_Co-60 2.370
ISWS_Th-232_Co-60 0.684
/* Conversion factors-------------------------------------------------------------------------------------
ISWA_AW_K-40 5.58
ISWA_AW_U-238 3.57
ISWA_AW_Th-232 1.22
ISWA_AW_Cs-137 1.02
ISWA_AA_Cs-137 201
ISWA_AP_Cs-137 2511000
ISWA_AP_Co-60 1505000
ISD_SDI 5.65E-08
ISWD_K-40 0.000289
ISWD_U-238 0.00197
ISWD_Th-232 0.000971
ISWD_Cs-137 0.000191
/* --------------------------------------------------------------------------------------------------
/* Corrections-------------------------------------------------------------------------------------------
```

```
/* Factor for the calculation of synthetic cosmic counts;&Factor_COS 14.35
/* Topographic correction;MTC Y
/* Radon correction;MRC N
/* Definition of additional Identifiers for corrected altitude and ground clearance,
/* an indicator for a new flight and the factor for calculation of synthetic cosmic counts
DEFINE&PZ_korr Corrected altitude im m;
DEFINE&PH_korr Corrected ground clearance in m;
DEFINE&New_Flight Switch for data composed of several flights;
DEFINE&Factor_COS Factor for calculation of synthetic cosmic counts
/* -------------------------------------------------------------------------------------------------
/* Evaluation of detector number 0
%
```

7.2 Detector RLL 004

These evaluation parameters were used for the evaluation of the measurements in Switzerland and the international exercise AGC24, with detector RLL 004.

```
V 2.0
HSW AGS_CH V0.0
HORG ABC-Kamir
HCTRY Switzerland
IAP Mirion 16l Container
ICA Superpuma
IPC WGS84
IPG From ARINC bus of helicopter
/* Parameters used for data evaluation---------------------------------------------------------------------
/* No data value;MND -999
/* Energy calibration;ISE0 0;ISE1 3;ISE2 0
/* Energy calibration;ISE0_D01 0;ISE1_D01 3;ISE2_D01 0
/* Energy calibration;ISE0_D02 0;ISE1_D02 3;ISE2_D02 0
/* Energy calibration;ISE0_D03 0;ISE1_D03 3;ISE2_D03 0
/* Energy calibration;ISE0_D04 0;ISE1_D04 3;ISE2_D04 0
/* Energy calibration;ISE0_D05 0;ISE1_D05 3;ISE2_D05 0
/* Energy calibration;ISE0_D06 0;ISE1_D06 3;ISE2_D06 0
/* Energy windows------------------------------------------------------------------------------------------
ISW_D06 Total;ISWE1_Total_D06 401;ISWE2_Total_D06 2997;ISWB_Total_D06 124.1;ISWC_Total_D06 5.78;ISWT_Total_D06 0.006;
ISWRA_Total_D06 0;ISWRB_Total_D06 0
ISW_D06 K-40;ISWE1_K-40_D06 1369;ISWE2_K-40_D06 1558;ISWB_K-40_D06 8.1;ISWC_K-40_D06 0.34;ISWT_K-40_D06 0.008;
ISWRA_K-40_D06 0;ISWRB_K-40_D06 0
ISW_D06 U-238;ISWE1_U-238_D06 1664;ISWE2_U-238_D06 1853;ISWB_U-238_D06 5.8;ISWC_U-238_D06 0.24;ISWT_U-238_D06 0.0055;
ISWRA_U-238_D06 0;ISWRB_U-238_D06 0
ISW_D06 Th-232;ISWE1_Th-232_D06 2407;ISWE2_Th-232_D06 2797;ISWB_Th-232_D06 0.3;ISWC_Th-232_D06 0.3;ISWT_Th-232_D06 0.006;
ISWRA_Th-232_D06 0;ISWRB_Th-232_D06 0
ISW_D06 Cs-137;ISWE1_Cs-137_D06 600;ISWE2_Cs-137_D06 720;ISWB_Cs-137_D06 19.9;ISWC_Cs-137_D06 0.63;ISWT_Cs-137_D06 0.01;
ISWRA_Cs-137_D06 0;ISWRB_Cs-137_D06 0
ISW_D06 Co-60;ISWE1_Co-60_D06 1100;ISWE2_Co-60_D06 1400;ISWB_Co-60_D06 11.8;ISWC_Co-60_D06 0.71;ISWT_Co-60_D06 0.008;
```

```
ISWRA_Co-60_D06 0;ISWRB_Co-60_D06 0
ISW_D06 MMGC1;ISWE1_MMGC1_D06 400;ISWE2_MMGC1_D06 1400;ISWB_MMGC1_D06 0;ISWC_MMGC1_D06 0;ISWT_MMGC1_D06 0.006;
ISWRA_MMGC1_D06 0;ISWRB_MMGC1_D06 0
ISW_D06 MMGC2;ISWE1_MMGC2_D06 1400;ISWE2_MMGC2_D06 2997;ISWB_MMGC2_D06 0;ISWC_MMGC2_D06 0;ISWT_MMGC2_D06 0.0065;
ISWRA_MMGC2_D06 0;ISWRB_MMGC2_D06 0
ISW_D06 LOW;ISWE1_LOW_D06 100;ISWE2_LOW_D06 400;ISWB_LOW_D06 0;ISWC_LOW_D06 0;ISWT_LOW_D06 0.02;
ISWRA_LOW_D06 0;ISWRB_LOW_D06 0
ISW_D06 MID;ISWE1_MID_D06 720;ISWE2_MID_D06 2997;ISWB_MID_D06 0;ISWC_MID_D06 0;ISWT_MID_D06 0.015;
ISWRA_MID_D06 0;ISWRB_MID_D06 0
ISW_D06 SDI;ISWE1_SDI_D06 240;ISWE2_SDI_D06 2997;ISWB_SDI_D06 84.6;ISWC_SDI_D06 4.32;ISWT_SDI_D06 0.0053;
ISWRA_SDI_D06 0;ISWRB_SDI_D06 0
/* Stripping factors-------------------------------------------------------------------------------------
ISWS_U-238_K-40_D06 0.997
ISWS_Th-232_K-40_D06 0.461
ISWS_Co-60_K-40_D06 0.023
ISWS_Th-232_U-238_D06 0.364
ISWS_U-238_Th-232_D06 0.096
ISWS_K-40_Cs-137_D06 0.449
ISWS_U-238_Cs-137_D06 3.358
ISWS_Th-232_Cs-137_D06 1.686
ISWS_Co-60_Cs-137_D06 0.090
ISWS_K-40_Co-60_D06 0.808
ISWS_U-238_Co-60_D06 2.435
ISWS_Th-232_Co-60_D06 0.668
/* Conversion factors-----------------------------------------------------------------------------------
ISWA_AW_K-40_D06 5.58
ISWA_AW_U-238_D06 3.57
ISWA_AW_Th-232_D06 1.22
ISWA_AW_Cs-137_D06 1.02
ISWA_AA_Cs-137_D06 201
ISWA_AP_Cs-137_D06 2511000
ISWA_AP_Co-60_D06 1505000
ISD_SDI_D06 5.65E-08
```

```
ISWD_K-40_D06 0.000289
ISWD_U-238_D06 0.00197
ISWD_Th-232_D06 0.000971
ISWD_Cs-137_D06 0.000191
/* -------------------------------------------------------------------------------------------------
/* Corrections--------------------------------------------------------------------------------------
/* Factor for the calculation of synthetic cosmic counts;&Factor_COS 14.35
/* Topographic correction;MTC Y
/* Radon correction;MRC N
/* Definition of additional Identifiers for corrected altitude and ground clearance,
/*an indicator for a new flight and the factor for calculation of synthetic cosmic counts
DEFINE&PZ_korr Corrected altitude im m;
DEFINE&PH_korr Corrected ground clearance in m;
DEFINE&New_Flight Switch for data composed of several flights;
DEFINE&Factor_COS Factor for calculation of synthetic cosmic counts
/* -------------------------------------------------------------------------------------------------
/* Spectra of detector 2 were re-binned to an energy calibration of 3 keV/channel.
/* Sum of single detectors was re-calculated to sum detector 6
/* Evaluation of detector number 6
/* Warning: The cosmic factor and the measured cosmic counts could be modified due to the evaluation of detector number 6
```

Paul Scherrer Institute PSI
Forschungsstrasse 111
5232 Villigen PSI
Switzerland
www.psi.ch